Modelling Structural Variations in Brain Aging

A thesis submitted in partial fulfillment
of the requirements for the degree of

Doctor of Philosophy
in
Electronics and Communication Engineering

by

Alphin J Thottupattu
20162301
alphinj.thottupattu@research.iiit.ac.in

Advisor: Prof. Jayanthi Sivaswamy

International Institute of Information Technology Hyderabad
500 032, India

May 2024

International Institute of Information Technology Hyderabad
Hyderabad, India

CERTIFICATE

This is to certify that work presented in this thesis titled ***Modelling Structural Variations in Brain Aging*** by *Alphin J Thottupattu* has been carried out under my supervision and is not submitted elsewhere for a degree.

_____ _____

Date Advisor: Prof. Jayanthi Sivaswamy

Acknowledgment

I would like to express my deepest gratitude to my supervisor, Professor Jayanthi Sivasawmy, for her guidance, insightful feedback, and invaluable corrections throughout the course of this research. Her expertise and guidance helped in channeling my research interests effectively. I am also indebted to Professor Venky P for his guidance in the mathematical aspects of my work. I am grateful to all my MIP lab-mates for their support during my Ph.D. journey, with special thanks to Naren, Abhinav, Prathyusha, Mythri, Sukesh, and my seniors Raghav, Arunava, Praveen, and Thripthi for their advice, encouragement, and willingness to help. A big thanks to Raghav for getting me started on my Ph.D. journey. I am deeply thankful to Dr. Avinash Sharma for his invaluable support and mentorship during my Ph.D. coursework, which served as a source of strength and inspiration to my journey.

Thanks to all volunteers who gave consent to undergo brain scans for the aging study, who made this study possible. I am grateful to Dr. Ravi Varma for his efforts to design the data collection protocols for the aging study and for his invaluable support throughout the data collection process. I am also grateful to all staff members from Citi Neuro Centre who assisted in scanning the volunteers. Special thanks to Dr. Vikas for helping us to establish connections for data collection. I would like to extend my gratitude to Dr. Keshavdas, Dr. Sheela, and Rajesh from SCTMT for their assistance in data collection and their dedicated efforts in providing expert segmentation markings for the brain images. I am thankful to Dr. Bharath Holla, Dr. Saini, and Dr. P.T. Sivakumar from NIMHANS for generously providing access to the elderly subjects' research data, which proved to be crucial for our study despite initial challenges in procurement. I am grateful to Dr. Tharani Putta for facilitating our collaboration with AIG Hospital, and I am also grateful to the management and all the staff members at AIG Hospital who contributed to identifying and procuring the research data essential for our study.

I owe everything to my parents for their belief in me, which has been the cornerstone of my academic journey. Their unconditional love, encouragement, and prayers, despite their limited experiences and perspectives, have been a constant source of strength and motivation. To my husband and son, your constant support and patience have been the foundation of this journey. Your love and constant support made tough times easier for me. I also want to express my heartfelt appreciation to my siblings and my in-laws whose enthusiasm and support have been incredibly encouraging. Thanks to my friends for always being there for me.

Abstract

The aging of the brain is a complex process shaped by a combination of genetic factors and environmental influences, exhibiting variations from one population to another. This thesis investigates normative population-specific structural changes in the brain and explores variations in aging-related changes across different populations. The study gathers data from diverse groups, constructs individual models, and compares them through a thoughtfully designed framework. This thesis proposes as a comprehensive pipeline covering data collection, modeling, and the creation of an analysis framework. Finally, it offers an illustrative cross-population analysis, shedding light on the comparative aspects of brain aging.

In our study, the Indian population is considered as the reference, and an effort is made to address gaps within this population through the creation of a population-specific database, an atlas, and an aging model to facilitate the study. Due to the challenges in data collection, we adopted a cross-sectional approach. A cross-sectional brain image database is meticulously curated for Indian population. A sub-cortical structural atlas is created for the young population, enabling us to establish reference structural segmentation map for the Indian population. Age-specific, gender balanced, and high-resolution scans collected to create the first Indian brain aging model. Choosing cross-sectional data collection made sense because data from other populations were also mostly collected in a cross-sectional manner. Using the in-house database for Indian population and publicly available datasets for other populations, our inter-population analysis compares aging trends across Indian, Caucasian, Chinese, and Japanese populations. Developing an aging model from cross-sectional data presents challenges in distinguishing between cross-sectional variations and normative trends. In response, we proposed a method specifically tailored for cross-sectional data. We present a unique metric within our comprehensive aging comparison framework to differentiate between temporal and global anatomical variations across populations.

This thesis has detailed a comprehensive process to compare the aspects of healthy aging across these diverse groups, ultimately concluding with a pilot study across four different populations. This framework can be readily adapted to study various research problems, exploring changes associated with different populations while considering factors beyond ethnicity, such as lifestyle, education, socio-economic factors, etc. Similar analysis frameworks and studies with multiple modalities and larger sample sizes will contribute to deriving more conclusive results.

Contents

List of Figures

List of Tables

Chapter *1*

Introduction

Biological systems and their processes are influenced by the environment in which they are established. In humans, the nervous system is one of the vital biological systems, and the brain is the most important organ in the system. It controls the entire body's functions, senses, thoughts, memory, and emotions. No other organ in the human body handles this wide variety of tasks, making the brain anatomy more complex. It is considered the most complex organization of matter in the universe. The brain plays a key role in a person's unique behavioral and intellectual capabilities. The complex anatomy and significant anatomical variations across subjects make the brain the most challenging organ to study in the medical field. The changes with time are inevitable for all natural systems and same for brain. Brain aging is a complex process due to various nature and nurturing factors, along with the intricate nature of the organ, making it challenging to study. The definition of a healthy brain aging raises questions, and the best approach is to analyze cohort-specific aging trends.
This thesis aims to study the normative structural variations associated with healthy adult human brain aging through the analysis of neuroimages. The study covers the examination of normative aging trends within a cohort and the comparison of variations across different cohorts.

1.1 Motivation

1.1.1 Studying the normative aging trends

The structural image of the brain is like a spatial map. To understand the brain and its variations among individuals, we need a comprehensive representation in a spatial coordinate system. This representation, essentially an average anatomy known as a structural template, serves as a foundational tool for defining the individual structural variations. The template serves as a reference, helping define other group average information such as structural and functional details. This spatially defined comprehensive representation is known as an atlas. With aging, the structure of the brain undergoes changes, emphasizing the importance of developing a model that can capture the average trends in structural changes to map associated information.
Brain aging is a natural transformation in the anatomy of the brain over time. It is expected to follow a specific pattern with relatively minor variations among individuals who share similarities in the

factors influencing brain aging. Understanding or defining the trends [193] or reference pattern of aging also helps us to define normal or abnormal anatomy variations with time.

1.1.2 Cohort-specific Modeling and Cross-Cohort Comparisons

The brain anatomy of a fetus is entirely determined by its genetic configuration, which has evolved over thousands of years from the life experiences of its ancestors. It has the immense potential to grow in infinite possible ways. As an individual grows, he/she learns new things and faces new situations; this training face of life influences brain anatomy. I.e., the brain anatomy of each individual is determined by nature and nurture. As these two factors vary broadly across individuals, brain anatomy shows complex variations across subjects. Hence, defining a single reference for the whole world will not work because the definition of a healthy biological process differs for different cohorts. Still, a common trend can be expected within a cohort. I.e., to study the normative behavior of aging, first group the brain scans from different individuals who are expected to have a similar aging pattern. Reference models for each cohort can be used for better representation and analysis. Cohort-specific models help to define standards for the corresponding cohort.

1.2 Designing the Aging Study

1.2.1 Choice of imaging modality

Understanding brain anatomy is crucial for grasping how the brain is structured and organized. It's like creating a map to navigate the brain's complexities and represent additional information spatially. Aging, in particular, induces changes in brain structure, and these structural changes serve as direct indicators of the aging process. Different methods to image the brain's anatomy include: MRI (Magnetic Resonance Imaging), CT (Computed Tomography) and Diffusion Tensor Imaging (DTI). Unlike CT, MRI provides clearer images of the brain's soft tissues, making it more effective for studying anatomy. Additionally, while DTI is valuable for exploring brain connectivity, our focus is on understanding the fundamental anatomy, and MRI is more suitable for this specific aspect of our research. Among MRI scans, T1 and T2 are popular ones, with T2 being well-suited for detecting abnormalities like edema, inflammation, or specific pathological conditions. However, for our research, we chose T1 MRI because it is excellent for visualizing the anatomical structures and details of tissues.

1.2.2 Cohort Definition: Understanding the Grouping Criteria

Let us consider the growth of two chillies as shown in Figure 1.1. Each chilli will have a unique *shape* which changes as it grows. If the chillies are of the same variety, there will be similarity in shape, otherwise not as in the case of long versus short chilli varieties. Hence, to define a reference model for the growth process, we should group the round chillies and long chillies separately.

Figure 1.1: Growth pattern of two chilli varieties

Defining such a grouping criteria need not be simple in case of a complex organ like Brain.
Age is an obvious criterion for grouping subjects to understand the common brain anatomy. The next question is whether the aging process is the same for different individuals. If not, another criterion to group individuals along with age is population. Within the same population, individuals typically share more common genetic and ethnic traits compared to different populations. Therefore, grouping based on population is a practical choice.

1.2.3 Cross-sectional Data Based Study

Normative structural information about aging trends can be a reference in neurological assessment. This normative trend can vary across populations. As aging is a time-controlled process, accurate modeling demands accurate extraction of the temporal changes. A large pool of longitudinal data is the key to developing a growth model to study the aging process. Longitudinal data has follow-up scans of the same subject over a while. That is the same person is scanned at multiple time points(longitudinal data), and the path connecting the follow-up scans will be the aging of that person. When multiple such paths are available for different individuals, an average aging path can be developed accurately. However, acquiring longitudinal data from a large cohort is a big challenge. This is not the case when the images are acquired from different individuals at different time points, i.e., cross-sectional data. Availability and scalability of cross-sectional data motivate methods to develop the aging model with cross-sectional data. Nevertheless, the challenges are different with cross-sectional data. The variations across subjects at different age points need not be because

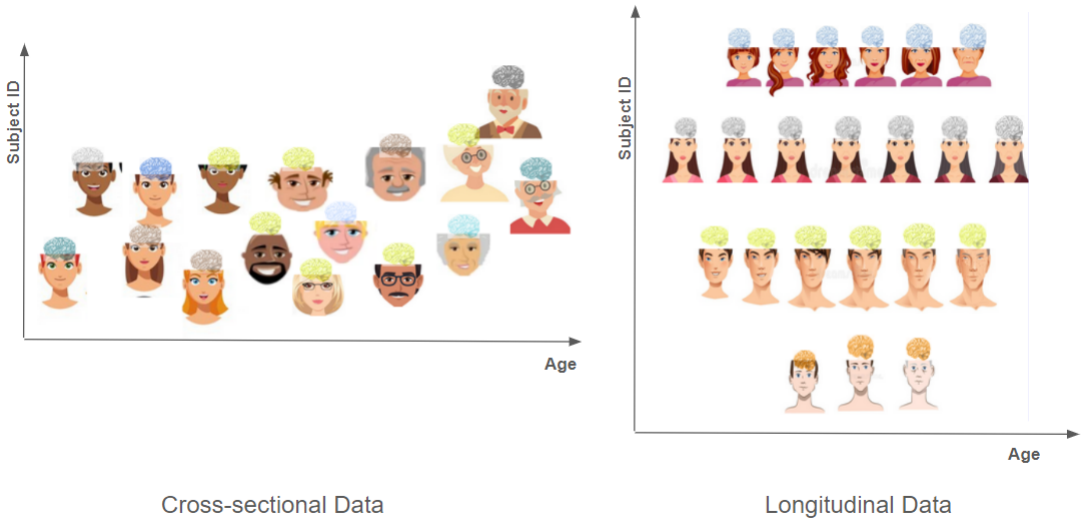

Figure 1.2: A schematic diagram of cross-sectional and longitudinal data acquisition difference

of aging but also cross-sectional variations across subjects. Figure 1.2 shows the difference in the acquisition of scans in the longitudinal and cross-sectional studies.

1.2.4 Path-based Modelling

Growth/aging is seen as a type of deformation because it involves shaping and expanding biological tissues and organs as they develop. When analyzing groups, our challenge lies in distinguishing between cross-sectional variations in the data and those caused by aging-related structural changes. Our goal is to define the aging process based on the average anatomy of the population under study. Towards this, we are attempting to model the brain aging process as the deformation of a structural template with an aging deformation. In general, tissue density statistics are used to understand the aging process. We propose a deformation comparison strategy to understand the aging process directly instead of using some derived information from the datasets. Age-related changes are better understood from image space. Nevertheless, comparison of aging trends across populations becomes difficult with analysis in the image space directly or using derived features like tissue densities. Instead, a direct comparison of aging deformations gives a better understanding of the population difference. Aging can be considered as a path through which age-related changes happen to the matured brain. A comparison of aging across populations is a comparison of these paths. Hence to understand population-differences in aging the idea is to compare the normative aging paths of different populations.

1.3 Thesis Contributions

1.3.1 Population-Specific Atlas: Segmentation Map for the Indian Brain Template

The normative anatomy of the brain, coupled with the accurate labeling of its structures, is essential for the development of a comprehensive reference system. Acknowledging the need for a dedicated reference system for the Indian population, we are taking the initiative to introduce the Indian Brain Atlas. Having an atlas designed for the Indian population greatly improves the accuracy of segmenting new brain volumes. The segmentation data developed for this purpose is valuable, aiding the creation and validation of various algorithms, especially those focused on population-specific studies.

1.3.2 Cross-sectional data based brain aging model

Establishing benchmarks for disease progressions and treatment effects relies on understanding normative anatomical variations during aging. Due to challenges in creating age-specific MRI templates and the discrete nature of age-range specific templates, a more practical approach involves developing an aging model. We propose a method to derive an aging model to leverage readily available and scalable cross-sectional data. Challenges in distinguishing age-related changes from cross-sectional differences are addressed. The aging deformation is derived from cross-sectional data and utilized to model aging as a deformation of the global anatomy obtained from the same data.

1.3.3 Comparative Framework for Brain Aging Across Populations

Brain aging induces structural changes, and these alterations vary across different populations. Additionally, the matured brain anatomy exhibits structural variations across populations. Distinguishing between global anatomy and age-related changes is challenging. However, discerning these differences is crucial for comprehending time-dependent changes and factors influencing brain aging across populations. In this thesis, we introduce a comprehensive analysis framework for comparing aging across different populations.

1.3.4 Indian Brain Aging Data Acquisition and Inter-Population Aging Comparison

We created a cross-sectional brain image database for Indian brain aging using scans from four sites (IIIT, NIMHANS, AIG, SCTMT). Subjects aged 20-80 years were grouped by decade, ensuring gender balance. The database, comprising Indian brain scans, was utilized to develop the first Indian brain aging model, all images being 3T high-resolution scans. Leveraging data from publicly available databases of other populations, we created population-specific models. A comprehensive analysis, along with the proposed comparison framework, was conducted to discern aging differences across populations.

1.4 A Roadmap to the Chapters

Chapter 2 lays the groundwork by exploring the mathematical and technical aspects essential for our study, along with a summary of the related works. Moving forward, Chapter 3 introduces the Indian Brain Atlas and its details. In Chapter 4, we present a method to understand aging using cross-sectional data. Chapter 5 details our framework for studying aging differences, and Chapter 6 gives a closer look at Indian Brain Aging Data collection and how aging compares across different populations.The chapters detail a comprehensive pipeline for creating population-specific aging models and comparing brain aging across different populations.

Chapter *2*

Background

The structural changes occurring in human brain follow specific patterns. Brain aging is a gradual process without any abrupt structural changes. In order to understand and define such changes, the structural changes are categorized as deformations within a specific class of smooth transformations. Modeling the temporal changes linked to aging requires preserving natural trends and properties. Given the complex nature of the brain and the structural variation across subjects, when group trends are analysed an average brain anatomy is used as a reference point. Specific methods are then employed to define the mapping across brains and model the group trend. Before delving into the methodological details, let's explore some fundamental concepts from differential geometry, a branch of mathematics focused on studying smooth shapes and spaces by examining their geometric properties, including curvature and topology. Structural changes in the brain involve smooth variations in shape, curvature, and size, and differential geometry offers tools and techniques to quantify and analyze these changes.

2.1 Differential Geometry Concepts used in the Thesis

The biological structures we analyze are embedded in Euclidean spaces, but the extracted features that represent the shapes need not belong to Euclidean spaces. The data is nonlinear, so the analysis of the anatomical variabilities should be done on a manifold, i.e., by linearizing the data space locally. To understand how this is accomplished, it's essential to comprehend the following concepts:

2.1.1 Shape Space

Shape space encompasses the entire spectrum of possible shapes an object can assume. This includes everything from simple geometric forms to intricate and irregular structures. Each point within shape space denotes a unique shape. In our analysis of the manifold, shape space (S) becomes a central concept. In order to study the shape transition between different states deformations are used which allows alteration of the geometry of a shape. These deformations, regarded as elements of a group, enable a systematic exploration of shape variations. By applying these group elements to a representative shape, often termed the Orbit Concept, we can methodically generate shapes within

S. This methodology furnishes us with a structured framework to comprehend and characterize the broad spectrum of shapes within S.

2.1.2 Topology

Topology is a mathematical discipline that studies the fundamental properties of geometric shapes and spaces, particularly focusing on concepts like continuity, connectivity, and deformation. It explores how these properties are preserved under smooth and continuous deformations, providing insights into the structure and relationships within complex shapes. The purpose of topology is to classify spaces. In topology, two entities are defined as equivalent if one can be deformed into another continuously. For example, it is impossible to make any rubber sheet into a rubber band with continuous smooth deformation. So, no rubber sheet can be topologically similar to any rubber band.
Two topological spaces are homeomorphic to each other if we can deform one into the other continuously. Homeomorphisms preserves topological invariants. When non-rigid deformation without any constraint is considered, it can even deform the brain to a sphere. Here the topological invariant is the genus of the entity(roughly speaking, holes).

Figure 2.1: Examples of Genus-0 topologically similar entities

Another topological invariant that can be considered is the number of boundaries, which also does not help topologically differentiate a brain surface from a sphere surface. For practical applications, such topological invariants alone need not help analyze anatomical variabilities. The data processing is tough without the inclusion of domain knowledge. For instance, a topological invariant-like genus of the surface is inadequate for differentiating surfaces as all the surfaces are topologically similar to genus 0. Hence, for practical applications, along with a simple topological invariant, defining a metric space that can quantify the similarity between entities is a better solution for the task. Metric spaces are a subset of manifolds and manifolds are a subset of topological space. In aging studies, embedding the representation in a metric space facilitates comparison across different aging trends.

2.1.3 Diffeomorphism

A manifold is a topological space locally homeomorphic to a Euclidean space. We can assign local coordinates to points in the manifold. One point can have multiple coordinates, but the transition from one to another should be smooth. The local homeomorphism of m-dimensional manifold M to Euclidean space $\mathbb{R}^m$ which is smooth and invertible is called a diffeomorphism. Homeomorphisms preserve the fundamental topological properties and diffeomorphisms go a step further by preserving smooth structures on the manifolds, including differentiable functions. Diffeomorphisms helps to map each point i in the manifold along with its neighborhood and this neighborhood is called a coordinated neighborhood. The mapping from U_i to $\mathbb{R}^m$ is referred to as a coordinate function ϕ_i, the diffeomorphic deformation. More details about the modelling of diffeomorphism are discussed in appendix section.

In summary the trio of shape space, topology, and diffeomorphisms forms a fundamental framework for understanding shape variations. Shape space represents all possible configurations of a shape, with each point denoting a unique manifestation. Topology classifies shapes based on their preserved properties. Diffeomorphisms, smooth and invertible mappings, enable systematic exploration and manipulation of shape variations while maintaining geometric properties. Together, they offer insights into shape variability across disciplines.

Computation of the diffeomorphic deformations is generally done in an optimization framework. The entire process of computing the deformation between one shape/image to another and deforming from one to another using the computed deformation is called Registration. The template for a particular set of shapes is generated by performing registration in an optimization framework such that the generated template captures all the characteristics specific to the shape class. Miller suggested an anatomical orbit model [120] to define the growth/atrophy happening in different human organ anatomies, where each anatomy sample is an orbit under Diffeomorphic Deformations of some template anatomy. Diffeomorphic deformations of a template anatomy represent the paths along which anatomical structures evolve or change over time. In this thesis, as previously discussed, we embrace a path-based modeling approach, wherein aging is conceptualized as the evolution of a template brain along a diffeomorphic path.

2.2 Modeling Brain Aging: Essential Methods

2.2.1 Registration

Capturing structural changes between two brains and aligning them is accomplished through image registration—a method that aligns different images into the same coordinate system. Because of brain anatomy's complex and highly variable nature, group analysis is almost impractical without a registration or alignment procedure that can handle complex deformations. Accuracy of the registration step is the key to determining the reliability of the analysis based on the data.

There are 3 main tools to perform registration: 1) Deformation, 2) Similarity Metric, 3)Interpolation method, and 4)Optimizer. Except for the first tool, other tools are commonly used in other methods like segmentation, regression, etc. Commonly used similarity metrics are Mean Square Error(MSE),

Local Correlation Coefficient(LCC), Mutual Information(MI), Spectral feature-based metrics, etc. Spline interpolation is used in general for getting visually better results. Gradient descent is used in general as an optimization method.
In this thesis, T1 structural MRI scans are considered for the analysis. In structural MRI registration, as mentioned before, the deformation needs to be smooth, and such deformations are modeled by constraining them to be invertible. A set of such invertible smooth deformations is referred to as diffeomorphic deformation. There are mainly two approaches for diffeomorphic registration. The first approach models the diffeomorphism as the integral path of displacement [130] or time-varying velocity field. This approach gives promising results and is mathematically grounded but has high computational complexity. The other approach assumes the deformations to be geodesics and parameterizes the deformations with the initial momenta or stationary velocity field [96] of the geodesics.
In the context of registration, stationary velocity based modelling of diffeomorphisms are more popular. Diffeomorphic registration involves finding a smooth and invertible transformation between two objects, often represented as differentiable manifolds. Diffeomorphism can be modeled using the exponential map applied to a stationary velocity field. The stationary velocity field, denoted as $\mathbf{v}$, characterizes the smooth deformation of one object into another without a change in velocity over time ($\frac{\partial \mathbf{v}}{\partial t} = 0$). The exponential map, denoted as $\exp(\cdot)$, is then employed to generate the diffeomorphic transformation from the velocity field. Mathematically, a diffeomorphism Φ can be expressed as $\Phi = \exp(\mathbf{v})$, where $\mathbf{v}$ and Φ maps points from the tangent space of the manifold back to the manifold itself. This diffeomorphic approach allows for smooth and invertible transformations, making it valuable in applications such as medical image registration and shape analysis. More details about this modelling is given in appendix.

2.2.2 Brain Atlas

A brain atlas in neuroimaging refers to a structural model that maps and labels different regions of the brain. The model includes predefined regions or structures within the brain, each labeled to indicate its anatomical or functional significance. The reference anatomy of the atlas is called the template. It acts as a standardized reference system, facilitating the comparison and analysis of brain images from diverse individuals or groups. Its purpose is to aid in the spatial normalization of individual brain MRI scans. Spatial normalization transforms individual brain images into a common coordinate system, allowing researchers to compare and integrate data from multiple subjects, simplifying the identification of common patterns or abnormalities across a population.
An ideal brain MRI template should represent the average anatomy and associated information of the studied population. The underlying average anatomy/template is derived in a way that minimizes the shape deformation on average across individual images in the group of brain images.Therefore, the template provides a standardized reference frame for aligning and comparing individual brain images, enabling researchers to derive meaningful conclusions from their group analyses.

2.2.3 Brain Aging Model

In this dissertation, the analysis of brain anatomy shape and variations is undertaken to model average patterns of brain aging. To capture the structural variations that contribute to average trends in brain aging, different types of variations are considered. A group of subjects is selected to study the aging process, and the average trends within this group are then derived. Variations in anatomy from one subject to another are termed inter-subject variations, and these can stem from genetic, physical, and psychological factors across subjects. Another category of anatomical variations occurs within the same subject's brain due to aging or certain disease conditions, termed intra-subject variations.

Both inter-subject and intra-subject anatomical variations can be effectively analyzed using non-linear models, which offer a more comprehensive representation of shape variations. The objective of a brain aging model is to identify the trajectory followed by the group by normalizing the inter-subject variations. This normalization process allows for a more accurate representation of average trends in brain aging, considering the diverse anatomical variations introduced by both inter-subject and intra-subject factors.

2.3 A Comprehensive Literature Review: Brain Aging Study

Many studies have been reported on brain aging [125], [117], [122], [123] and disease progression [116], [129] based on longitudinal data collected from subjects/patients. Brain development and aging studies have been done separately for different populations in the literature [51–53,55,68]. The importance of population-specific studies is also discussed in the literature [8]. In these studies, statistical volumetric analysis of different parts of the brain was done using automatic segmentation. The volumetric analysis is insufficient to develop a brain growth model. Hence, deformation models have been developed for brain growth, and disease progression [125], [117], [122], [123], [116], [129]. Temporal shape and size changes are initially modeled by a linear shape model. However, the underlying data is not linear, and hence a manifold framework is required.
Longitudinal data-based spatiotemporal atlases have been generated mainly to analyze disease progression [105]. Sourcing such data for a healthy population is challenging. Researchers have tried statistical and principal component analysis on this type of data, considering the data belongs to a non-linear space, i.e., manifold. Average growth, which is a result of natural deformation, belongs to a group of diffeomorphic deformation.

2.3.1 Diffeomophic Model based Studies

Diffeomorphic growth model-based analysis of the aging process has been studied in two ways: i) by considering longitudinal data of different subjects and combining the growth trajectories, ii) using take cross-sectional, time-series data. Miller [120] has suggested a method based on the orbit model to continuously evolve a template through a time series of images by connecting the images through a geodesic path [120] using the LDDMM framework. This approach needs dense time

sampling of the data. In [119], the authors suggest a discrete version of [120] by defining the evolution with the integration of a time-dependent velocity field. When longitudinal data is available, an interpolation of piece-wise geodesics to model the growth [126] is possible. Growth trajectories have also been modeled with acceleration (instead of velocity) field [112]. In this approach, the registration step's accuracy determines the growth model accuracy. Aging has been modeled as a time series regression in different ways such as a geodesic [138–142]piece-wise geodesic [143], as a spline [144], polynomial [145], nonlinear kernel-based [146] regression paths as well as with stationary velocity fields parameterized path [148] and acceleration parameterized path [149, 150]. Time-series regression methods find a path to best fit the time series data using the initial data point (image) as the path's starting point. In [148], the method has used longitudinal data to define an aging model by transferring individual growth trajectories to a global template space. The data, however, has been sourced for a small cohort over a shortage interval. Kernel-based approaches are used for modeling brain growth when cross-sectional data is used, where images at different time instances are interpolated smoothly to represent the growth at different time instances [118]. But such cross-sectional models do not allow us to understand the aging deformation and compare the same across models from different populations.

Chapter *3*

Population-Specific Atlas: Segmentation Map for the Indian Brain Template

In this study, we aim to explore brain aging in connection with concepts from differential geometry. As discussed in the 'Concept of Orbit,' a template shape exists for a group of brains, and aging can be modeled as a deformation of this template. When a template carries additional information, such as structural segmentation maps, it is referred to as an atlas. With this added information, it becomes possible to map the same to other age points, making the aging model more informative and easier to validate. Therefore, in this work, we have developed a segmentation map for the Indian Brain template established in [199].
The brain template and the segmentation map together constitute the first Indian brain atlas. Getting accurate segmentation maps is crucial to develop an atlas. Hence here we discuss the segmentation map generation for the individual images, validation of segmentation maps and finally the atlas generation and validation of the same.

3.1 Indian-specific brain segmentation database

A set of 114, 1.5 Tesla, T1 MRI scans with manual delineations for 14 sub-cortical structures were developed to study population-specific differences in the Indian brain. The scans in the dataset were acquired from healthy young (21-30 years) subjects (58 male and 56 female) and all the structures are manually delineated by experienced radiology experts. Creating a brain segmentation database for the Indian population and making the data publicly available is one of the implicit goals of this thesis as there exists no such database. We present an Indian Brain Segmentation Dataset (IBSD), for sub-cortical brain segmentation. This has 114 MR volumes generated under a fixed imaging protocol. Each volume has 14 labeled sub-cortical structures. The number of MR scans in the dataset is of an approximately equal number of male and female subjects belonging to a young age group (20-30 years). This data is used to create a template for the young Indian population.
Our sub-cortical structure segmentation dataset, Indian Brain Segmentation Dataset (IBSD), is available at `https://doi.org/10.5281/zenodo.5656776`. Some of the widely used public

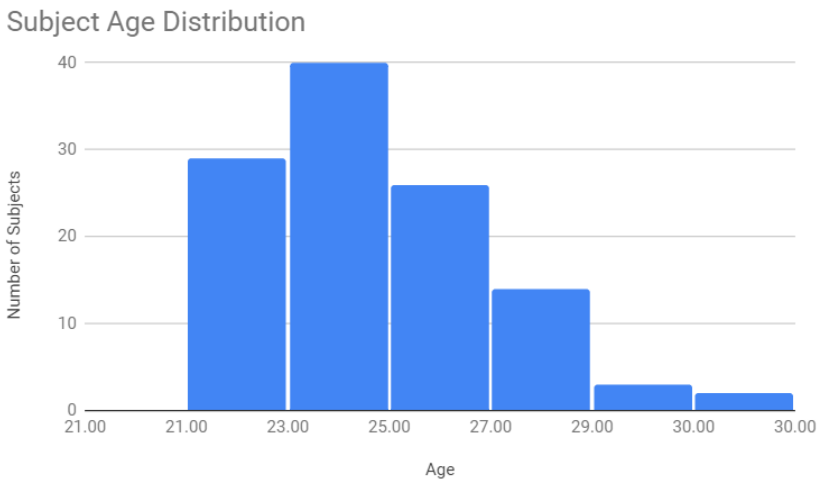

Figure 3.1: Age histogram of 114 volunteers

datasets for brain segmentation and the number of MR volumes and structures with markings/labels are: i) MICCAI 2012 [20] with 35 MR volumes and 134 labeled structures ii) IBSR [21] with 20 volumes and 43 labeled structures and iii) LPBA40 [63] with 40 volumes and 56 labeled structures iv) Hammers67n20 [23] with 20 volumes and 67 labeled structures and v) Hammers83n30 [23] with 30 volumes and 83 labeled structures. Besides these, there are few public structure-specific datasets with only (ex. hippocampus, [24]). private datasets such as those introduced by Babalola et al. provide 270 volumes and labels (via semi-automated segmentation) for 18 structures. The neuroimages in these datasets are of young to elderly individuals.

3.1.1 Database Development

3.1.1.1 MRI Images Used to Create Segmentation Database

We used MR scans collected from 114 young (21-30 years) healthy adult volunteers. This database was created as part of another thesis from our team [136]. All the adults had completed their schooling, and a majority (> 90%) had an undergraduate-level education. Healthy volunteers who had no past history of head injury were selected for the study. Figure3.1 shows the age distribution of all the volunteers. An experienced psychiatrist examined all the volunteers and helped select only psychologically healthy subjects for the study. A clinician and an experienced neurologist examined all the scans to identify and exclude those with any structural abnormalities. After scrutiny, scans of 58 male and 56 female volunteers were finally selected for inclusion in our study. As approved by the Institute Review Board, the study involved collecting MRI volumes of young adults after obtaining informed consent in writing. Written consent from each volunteer is to use their anonymized MRI scan for research purposes. The work described has been carried out in accordance with The Code of Ethics of the World Medical Association. Scanning was done at three

different sites, which had different models of scanners as follows. The sitewise distribution was as follows: 39 subjects were scanned using Siemens 1.5T MRI scanner with T1 MPRAGE sequence, TE/TR/TI = 2.9 / 2370/ 1000 ms and flip angle=7°; 38 subjects were scanned using GE 1.5T MRI scanner with T1 BRAVO sequence TE/TR/TI = 4.2 /10.2/450 ms and flip angle=15°; and finally 37 subjects were scanned using Phillips 1.5T MRI scanner with T1 3D TFE sequence with TE/TR/TI = 3.8/8.2/- and flip angle=7°. The imaging protocol was fixed to obtain scans with a voxel size of $1 \times 1 \times 1mm^3$ and a 3D matrix size of $256 \times 256 \times 192$. The MRI volumes were acquired using 192 sagittal cuts.

Preprocessing

All the MRI volumes were pre-processed using a standard pipeline consisting of N4 Bias field correction [66] followed by denoising using Non-local Means filtering [59]. Skull stripping was done with the Brain Extraction Tool [28] and all the images were checked manually slice by slice (using ITK-SNAP) to ensure good image quality after preprocessing.

3.1.1.2 Sub-cortical segmentation labels

The seven sub-cortical structure pairs (Left and Right) chosen for markings were the Thalamus, Putamen, Pallidum, Hippocampus, Amygdala, Caudate and Accumbens area. Experts from Sree Chitra Tirunal Institute for Medical Sciences and Technology, India did all the manual markings. The seven structures in each of the 2 hemispheres are illustrated with different colors in 3 canonical views for a sample slice in Figure 3.2.

Sub-cortical structure segmentation approach

The process of image marking/labeling had 4 sequential steps: i) automated labeling, ii) label correction by a trained person, iii) label correction by a radiologist with 2 years of experience and iv) label finalization by a senior neuroradiologist who has more than 25 years of experience. In order to perform the automated labeling, a set of 14 sub-cortical labels from Talairach Daemon labels [29] were transferred to each brain MRI scan. These were then manually edited using the ITK-SNAP [30] tool by a trained person to correct for overshoots and fill the missing voxels. The first two steps helped the radiologists to concentrate on fine-tuning the markings and producing good-quality labels. A radiologist then corrected the labels by overlaying them on the actual 3D MRI scans slice by slice. The corrected labels were checked in the 3 canonical views (coronal, sagittal, and axial views) to verify the completeness of the 3D shape and labels. In the same way, the corrected labels were finalized by a senior neuroradiologist. Experts delineated the structures using tissue intensity, relative position, and structure shape information from their experience. 3D-mesh visualization of each structure helped the experts to verify the delineated structure shape with the expected shape in their minds. The slice-by-slice delineation and 3D visualized cross-verification in each step helped the experts to work efficiently.

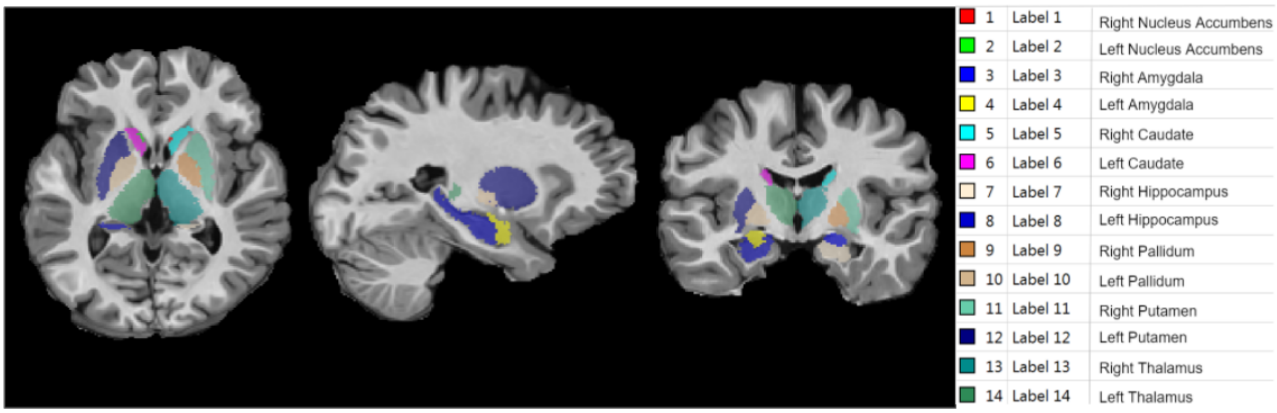

Figure 3.2: Sub-cortical Structure labels of a sample subject image visualized in 3 planes. The labels corresponding to each color-mapped structure are given on the right side.

3.1.1.3 Data Records

All 114 scans and their labels are made publicly available at `https://doi.org/10.5281/zenodo.5656776`. The IBSD dataset is organized: T1 weighted preprocessed 3D MRI scans and corresponding label files are stored in the main directory. Each label file has *.ch.nii.gz* extension with the same filename as the corresponding 3D MRI scan. All the image files are stored in NIFTI format. The sub-cortical structure labels are numbered in Figure 3.2.

3.2 Segmentation-map Validation

To gauge the level of corrections made by experts on the markings supplied to them, the dice and Hausdorff distance (HD) between the supplied and corrected labels are calculated. A dice of 0.985 ± 0.112 and HD of 1.073 ± 6.908 is observed. As HD captures the worst-case deviations between the markings, one can infer that the expert did correct the labels up to as many as 8 voxels. The Dice value on the other hand is a metric for global assessment as it captures the degree of the overlap between the supplied and corrected labels. This is not very informative in drawing insights into the degree of corrections made by the expert. This is because the expert was correcting the boundaries of structures in the supplied markings.

The data quality of IBSD was checked by doing a comparison with other datasets. This is first done via a visual comparison of the image and the segmented structures. Next, IBSD data was used to train and test currently popular non-DL algorithms as well as state-of-the-art DL algorithms which report results on public datasets. Specifically, segmentation was done with two popular toolboxes namely the Freesurfer [31] and FIRST, [32]; It was also done with DL methods namely 3D U-net [33], Residual 3D U-net [34], Dense U-net [35] V-net [36], M-net [13] and the state of the art ψ-net [14]. The segmentation performance of Freesurfer [31], FIRST [32]; 3D U-net [33], and ψ-net [14] was assessed on IBSD as well as two other public datasets namely MICCAI 2012 [20] and IBSR [21] for comparison.

3.2.0.1 Evaluation Measures

Two commonly used metrics are used for the quantitative evaluation of the segmentation methods. These are the Dice Similarity Coefficient (Dice) [37] and the Hausdorff Distance (HD) [73]. Dice helps assess the degree of overlap between the ground truth and computed segments while the HD helps capture any tendency to over/under segment at a local level by a method. Since these two metrics help assess the accuracy of a method at a global and local level they are appropriate to evaluate accurate and spatially consistency of segmentation results. Let A and B be the predicted segmentation and ground truth respectively. The Dice coefficient is found by computing the overlap between the computed segmentation result and the ground truth:

$$Dice(A, B) = \frac{2 \times |A \cap B|}{|A| + |B|}, \tag{3.1}$$

Where $|A \cap B|$ denotes the number of pixels in the overlapping region between computed segmentation and ground truth while $|A| + |B|$ denotes the number of pixels in A and B. The Dice score varies between 0 and 1, with 0 indicating no overlap or segmentation failure and 1 indicating complete overlap with ground truth or perfect segmentation.

HD is a spatial distance based metric, unlike Dice which assesses the overlap. HD therefore is based on computing the Euclidean distance between A and B as well as B and A as follows.

$$HD(A, B) = max(h(A, B), h(B, A)), \tag{3.2}$$

$$h(A, B) = \max_{a \in A} \min_{b \in B} \parallel a - b \parallel, \tag{3.3}$$

$\parallel \ . \ \parallel$ is the Euclidean distance. Unlike Dice, HD is not bounded, however, lower values of HD indicate better segmentation.

Dataset	Image Resolution	Age Range	# of subjects (Male:Female)	# of labels (total: sub-cortical)
IBSR	0.93x0.93x1.5 or 1x1x1.5 mm^3	Juvenile to 71	14:4	43:14
MICCAI2012	1x1x1.25 mm^3	18-90	22:13	134:14
LPBA40	2x2x2 mm^3	19.3-39.5	20:20	56:6
IBSD	1x1x1mm^3	21-30	58:56	14:14

Table 3.1: Broad description of neuroimage datasets (of 1.5 T scans) for segmentation.

Visual assessment of IBSD data

Image resolution and quality have a major role in determining the quality of final manual delineations. The specifications of various datasets such as image quality parameters and subject information are listed for comparison in Table 3.1. It can observed that IBSD has the highest number of scans (58+56 = 114) and the best image resolution (1mm isotropic voxel). A sample slice

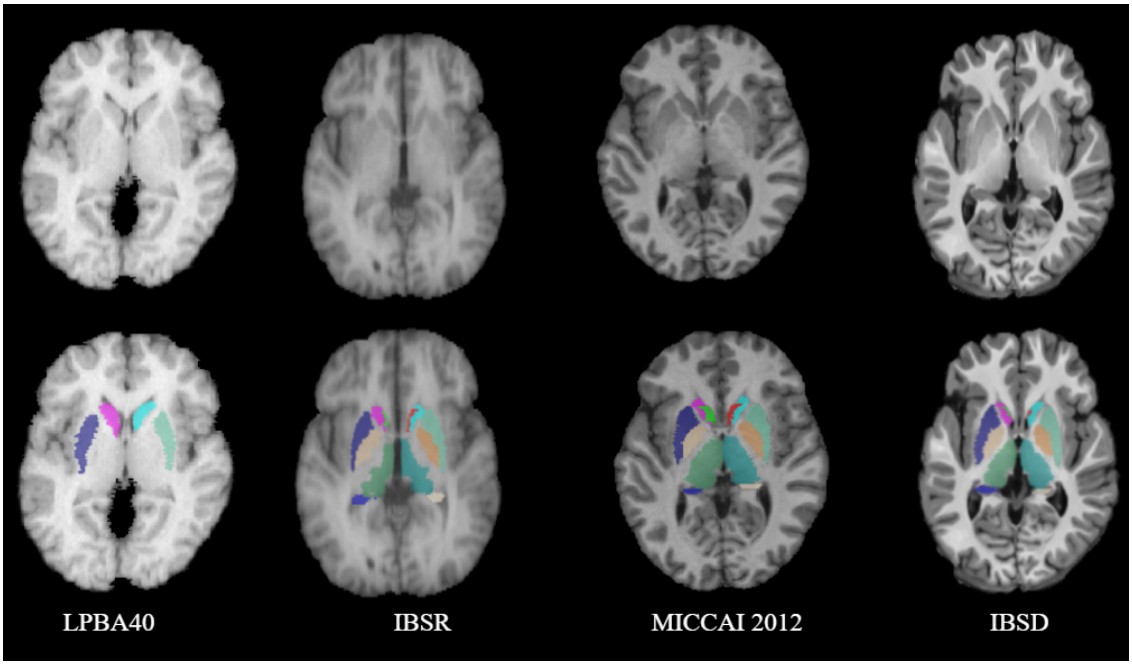

Figure 3.3: Visual Comparison of quality of MR image in (first row) and segmentation (second row) with central slices of the volume

image from 3 public datasets (LPBA40, IBSR, MICCAI 2012) and IBSD is shown in Fig. 3.3. The IBSD image is seen to be visually similar in the MICCAI 2012 dataset due to the similarity in image resolution, though with better contrast.

Validation of IBSD via automatic segmentation

Validation of IBSD was done using two types of automated segmentation algorithms, namely those based on traditional machine learning and DL. If DL methods demonstrate good segmentation performance then it can be inferred that the size of the dataset and image quality are good as these DL methods are data driven.

The performance figures of two commonly used conventional segmentation tools, namely the Freesurfer [31] and FIRST [32], are presented in TABLE 3.2 while those for DL-based methods are presented in Table 3.3. The Nucleus Accumbens (Label 1-2) is significantly smaller than others which affects the automatic segmentation performance. So, the performance excluding Accumbens', i.e. only for labels 3-14, is also reported in TABLE 3.2 and 3.3.

A six-fold cross validation was done to assess the DL methods by splitting the 114 volumes into six folds with 19 images in each; of these, four folds were used for training, one fold for validation and one for testing. Six different models were thus obtained, tested separately and the performance scores were averaged and reported for each segmentation method.

When one compares the results in Table 3.3 with those for non-DL methods in TABLE 3.2, it is apparent that the DL methods outperform the non-DL methods. Among the DL methods, the Dense U-net shows the best performance on IBSD, with a 14% improvement in Dice and nearly 100%

improvement in HD over the best non-DL (FIRST) method. Exclusion/inclusion of Accumbens appears to impact the Dice score but not the HD value as indicated by the figures in the last 2 rows of the Table. A consistent performance is observed with DL methods (see Table 3.3) using U-net based architectures on the IBSD dataset as the Dice scores are between 0.87 to 0.88 and HD value is between 2.9 and 5. This attests to the integrity of the IBSD data.

Label	Structure	Freesurfer		FIRST	
		Dice	HD	Dice	HD
1	Right Nucleus Accumbens	0.55 ± 0.08	7.14 ± 3.71	0.64 ± 0.09	6.27 ± 3.45
2	Left Nucleus Accumbens	0.51 ± 0.13	8.67 ± 3.37	0.57 ± 0.09	16.26 ± 10.42
3	Right Amygdala	0.66 ± 0.04	5.68 ± 4.7	0.71 ± 0.05	4.9 ± 4.82
4	Left Amygdala	0.67 ± 0.05	4.16 ± 0.8	0.71 ± 0.05	3.76 ± 1.06
5	Right Caudate	0.8 ± 0.03	8.02 ± 2.64	0.79 ± 0.04	5.31 ± 1.38
6	Left Caudate	0.81 ± 0.03	7.83 ± 2.48	0.79 ± 0.05	4.36 ± 1.43
7	Right Hippocampus	0.81 ± 0.03	4.18 ± 0.81	0.8 ± 0.03	3.96 ± 0.89
8	Left Hippocampus	0.77 ± 0.03	5.04 ± 0.96	0.76 ± 0.04	4.78 ± 1.28
9	Right Pallidum	0.77 ± 0.03	4.44 ± 1.2	0.79 ± 0.05	3.43 ± 0.67
10	Left Pallidum	0.69 ± 0.03	4.39 ± 1.19	0.78 ± 0.06	3.04 ± 0.61
11	Right Putamen	0.83 ± 0.03	5.31 ± 1.84	0.85 ± 0.03	4.95 ± 1.98
12	Left Putamen	0.82 ± 0.05	8.54 ± 2.84	0.85 ± 0.03	8.56 ± 2.88
13	Right Thalamus	0.84 ± 0.02	4.69 ± 0.53	0.86 ± 0.02	4.47 ± 0.7
14	Left Thalamus	0.83 ± 0.03	4.75 ± 0.89	0.86 ± 0.02	4.22 ± 0.81
	Average of label 3-14	0.78 ± 0.04	5.59 ± 1.74	$\mathbf{0.8 \pm 0.04}$	$\mathbf{4.65 \pm 1.54}$
	Full Average	0.74 ± 0.05	5.92 ± 2	$\mathbf{0.77 \pm 0.05}$	$\mathbf{5.59 \pm 2.31}$

Table 3.2: Segmenttation performance of Freesurfer and FIRST on IBSD data. The mean Mean$\pm$ Standard Deviation values are reported for Dice coefficient and HD.

Segmentation performance comparison with IBSD and other datasets

It is well known that the performance of segmentation algorithms depends on many aspects of the dataset, such as the number of images in the set, image quality, and structural details. As a final experiment, three models were trained and tested on two public datasets (IBSR and MICCAI 2012) and compared with that on IBSD. The obtained results are presented in Table 3.4, with the best results for each method indicated in bold font. From this Table, it can be observed that training on IBSD yields the best Dice consistently for all 3 DL methods (last 3 rows), and the lowest HD value is obtained for 2 of 3 DL methods.

Label	Structure	3D U-net		Residual 3D U-net		Dense U-net		V-net		M-net		$\psi - net$	
		Dice	HD	Dice	HD	Dice	HD	Dice	HD	Dice	HD	Dice	HD
1	Right Nucleus Accumbens	0.751 ±0.06	3.856 ±0.147	0.767 ±0.061	4.68 ±1.827	0.778 ±0.056	3.783 ±0.412	0.74 ±0.068	3.669 ±0.628	0.788 ±0.012	3.759 ±0.472	0.782 ±0.06	3.893 ±0.373
2	Left Nucleus Accumbens	0.708 ±0.056	4.026 ±0.377	0.72 ±0.052	3.706 ±0.244	0.728 ±0.054	3.868 ±0.15	0.7 ±0.057	3.865 ±0.475	0.735 ±0.008	3.769 ±0.215	0.729 ±0.061	3.955 ±0.308
3	Right Amygdala	0.849 ±0.028	3.038 ±0.858	0.86 ±0.031	3.499 ±1.224	0.864 ±0.029	2.915 ±0.842	0.839 ±0.038	3.378 ±1.112	0.872 ±0.004	2.884 ±0.733	0.867 ±0.036	3.475 ±1.472
4	Left Amygdala	0.828 ±0.03	3.195 ±0.299	0.841 ±0.035	3.423 ±0.85	0.846 ±0.031	2.879 ±0.358	0.805 ±0.054	3.252 ±0.54	0.854 ±0.004	2.958 ±0.63	0.849 ±0.039	3.074 ±0.379
5	Right Caudate	0.902 ±0.015	3.11 ±0.849	0.905 ±0.017	3.512 ±0.926	0.908 ±0.014	2.911 ±0.707	0.896 ±0.031	2.718 ±0.311	0.903 ±0.003	2.864 ±0.984	0.909 ±0.015	7.952 ±8.141
6	Left Caudate	0.902 ±0.014	3.83 ±1.854	0.906 ±0.014	3.91 ±0.487	0.908 ±0.013	2.96 ±0.158	0.898 ±0.022	3.647 ±1.319	0.903 ±0.002	3.234 ±1.073	0.909 ±0.015	4.396 ±1.216
7	Right Hippocampus	0.885 ±0.013	3.884 ±1.236	0.891 ±0.012	3.903 ±2.283	0.894 ±0.011	2.688 ±0.265	0.875 ±0.02	3.584 ±0.717	0.889 ±0.004	3.361 ±1.103	0.898 ±0.012	7.533 ±3.66
8	Left Hippocampus	0.871 ±0.017	3.715 ±1.516	0.876 ±0.017	3.382 ±0.548	0.88 ±0.016	3.086 ±0.479	0.858 ±0.029	3.28 ±0.305	0.874 ±0.003	3.709 ±1.314	0.883 ±0.019	6.934 ±3.323
9	Right Pallidum	0.88 ±0.017	2.021 ±0.101	0.887 ±0.017	2.983 ±1.996	0.893 ±0.015	1.811 ±0.075	0.868 ±0.021	2.275 ±0.134	0.893 ±0.003	2.106 ±0.769	0.904 ±0.014	2.734 ±2.176
10	Left Pallidum	0.871 ±0.022	2.121 ±0.076	0.882 ±0.021	2.029 ±0.113	0.883 ±0.021	2.01 ±0.133	0.86 ±0.027	2.345 ±0.189	0.886 ±0.002	2.351 ±0.707	0.895 ±0.02	2.176 ±0.129
11	Right Putamen	0.907 ±0.013	3.213 ±0.134	0.911 ±0.013	3.783 ±1.108	0.915 ±0.014	3.206 ±0.161	0.904 ±0.02	3.424 ±0.509	0.908 ±0.001	3.027 ±0.564	0.92 ±0.012	4.511 ±2.214
12	Left Putamen	0.902 ±0.014	3.747 ±0.441	0.906 ±0.014	3.671 ±0.719	0.909 ±0.013	4.126 ±1.419	0.899 ±0.02	4.071 ±1.358	0.903 ±0.001	3.565 ±0.496	0.913 ±0.015	6.973 ±3.541
13	Right Thalamus	0.928 ±0.01	2.704 ±0.6	0.931 ±0.009	2.794 ±0.625	0.934 ±0.008	2.377 ±0.051	0.923 ±0.012	2.648 ±0.215	0.924 ±0.002	2.787 ±0.692	0.938 ±0.008	4.795 ±2.619
14	Left Thalamus	0.928 ±0.01	3.858 ±1.212	0.931 ±0.01	4.527 ±1.486	0.934 ±0.009	2.544 ±0.12	0.922 ±0.013	2.896 ±0.43	0.923 ±0.002	3.219 ±0.933	0.937 ±0.01	6.928 ±2.766
	Average of label 3-14	0.888 ±0.017	3.203 ±0.368	0.894 ±0.017	3.451 ±0.406	0.897 ±0.016	**2.793 ±0.057**	0.879 ±0.026	3.126 ±0.489	0.894 ±0.003	3.005 ±0.833	**0.902 ±0.027**	5.123 ±1.463
	Full Average	0.865 ±0.023	3.308 ±0.332	0.872 ±0.023	3.557 ±0.442	0.877 ±0.022	**2.94 ±0.041**	0.856 ±0.031	3.218 ±0.467	0.867 ±0.002	3.005 ±0.734	**0.881 ±0.065**	4.952 ±1.23

Table 3.3: Performance of 3D Unet, Residual 3D Unet, Dense U-net and V-net with IBSD data in terms of dice coefficient and HD with respect to Ground truth. The values are in Mean± Standard Deviation format

	IBSR		MICCAI		IBSD	
	Dice	Hausdorff Distance	Dice	Hausdorff Distance	Dice	HD
3D-Unet	0.842 ± 0.052	3.52 ± 0.86	0.840 ± 0.047	4.01 ± 1.87	**0.865 ±0.023**	**3.308 ±0.332**
Dense U-net	0.846 ± 0.092	3.41 ± 1.27	0.864 ± 0.055	3.24 ± 1.64	**0.877 ±0.022**	**2.94 ±0.041**
ψ-net	0.855 ± 0.074	3.02 ± 0.55	0.875 ± 0.056	**2.76 ± 0.72**	**0.881 ±0.065**	4.952 ± 1.23

Table 3.4: Free-surfer,FIRST, 3D U-net, Dense U-net and ψ-net performance compared with IBSR, MICCAI and IBSD data with average dice coefficient and HD(in mm) for 14 sub-cortical structures.The values are in Mean± Standard Deviation format

3.3 Brain Atlas for Indian Population

The IBA100 template is an existing brain reference model generated with the IBSD database. Using 100 brains and corresponding structure maps from IBSD, a brain atlas for the Indian population was created. The markings were first transferred to the template space(IBA100 template), and the co-registered structure markings combined to generate a probability map for each structure. The constructed structure maps overlaid on IBA100 are given in Fig:3.4.

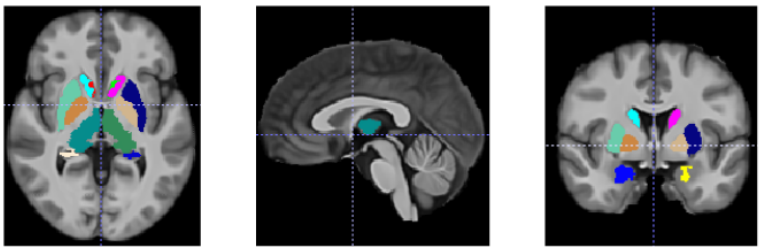

Figure 3.4: Indian brain template (i.e., IBA100) of the young population together with its Maximum probability structure maps . Left to right:Axial, Coronal and Sagittal slices

3.3.1 Comparison and Validation

We compared IBA100 with two different population atlases at the structure level, namely, LPBA40 [63] and Chinese2020 [57]. This comparison is motivated by the fact that atlases are popular in automated structure segmentation [39], [45] and selection of the structure atlas could be important. The Chinese2020 atlas is labeled by AAL atlas [67], where 45 anatomical volumes of interest (AVOI) in each hemisphere are marked and the LPBA40 has manual markings for 56 structures. IBA100 has manual markings for 6 structures in 2 hemispheres. Two of these structure pairs, namely, hippocampus and putamen are common with the other 2 population atlases and hence their average volumes (measured in the respective atlas space) were compared. These averages are tabulated as a percentage of the total brain volume in Table:3.5. The size of the structures of the Indian population is more similar to that of the Chinese population. Overall, however, there is a significant difference in the structure volumes across the 3 atlases. Thus, variation across populations appears to also hold at the structure level.

Structure	**IBA100**	**LPBA40**	**Chinese2020**
L-Hippocampus Volume(mm^3)	0.23	0.47	0.37
R-Hippocampus Volume(mm^3)	0.25	0.49	0.37
L-Puttamen Volume(mm^3)	0.32	0.68	0.39
R-Puttamen Volume(mm^3)	0.31	0.66	0.43

Table 3.5: Comparison of volume of different structures in % w.r.t. the total volume from different population atlases.

Table 3.6: Comparison of Volume of different structures in the Validation set with different population specific structure maps

Structure	**Expert marking** (mm^3)	**IBA100 label transfer-Volume** (mm^3)	**IBA100 vs Expert marking** ($dice$)
L-Hippocampus	3280.7±309.9	3214.6±290.1	0.847
R-Hippocampus	3399.5± 220.6	3353.1±227.6	0.862
L-Puttamen	4310.6± 300.6	4272.5±345.2	0.89
R-Puttamen	4215.1± 308.9	4099.5±338.9	0.88

The probability map, created by using the 100 co-registered volumes, is used to create a maximum probability structure map. The maximum probability structure map registered with each of the 15 validation volumes, and the labels are transfered to get the corresponding labels for the 15 validation volumes [54]. On the same 15 volumes, we got markings from experts for 2 structure pairs: Hippocampus and Puttamen. These markings were done by one medical expert and cross checked by a senior expert. We analyzed whether there is a good agreement between population specific structure map based segmentation and the expert markings for the 2 structure pair segmentations. For comparison we used Dice coefficient and volume statistics of two structure pairs- Hippocampus and Puttamen and the details is given in Table:3.6.

Chapter *4*

A Diffeomorphic Aging Model for Adult Human Brain from Cross-Sectional Data

Normative aging trends of the brain can serve as an important reference in the assessment of neurological structural disorders. Such models are typically developed from longitudinal brain image data – follow-up data of the same subject over different time points. In practice, obtaining such longitudinal data is difficult. We propose a method to develop an aging model for a given population, in the absence of longitudinal data, by using images from different subjects at different time points, the so-called cross-sectional data. We define an aging model as a diffeomorphic deformation on a structural template derived from the data and propose a method that develops topology preserving aging model close to natural aging. The proposed model is successfully validated on two public cross-sectional datasets which provide templates constructed from different sets of subjects at different age points.

4.1 Introduction

Human brain morphometry varies with respect to age, gender, and population. Since the human brain changes structurally with age, understanding the normative aging process from structural and functional images has been of interest both in general and within a specific population. Studies aimed at arriving at such an understanding, either use a longitudinal or a cross-sectional design for collecting images of the study cohort. The former is usually difficult as it is challenging to access a fixed cohort over an extended number of years and scan them repeatedly. A more pragmatic approach is based on a cross-sectional design where a set of individuals in different age range forms the cohort. This approach makes it easier to collect scans but their analysis requires a disentangling of the inter-subject variations from age-related changes which is not straight forward. A more elaborate treatment of the differences in such approaches can be found in [132].

Regardless of the design, templates play a major role in gaining an understanding of the aging process and derive a normative standard. Templates are images defined using an appropriate reference coordinate space. Templates created for the young adult Caucasian population [133, 134] are the most well known and used, though population specific templates are also gaining attention [135, 136]. In computational anatomy, aging is typically modelled as a *continuous* deformation

of a template image over time [137]. This modelling helps to derive any age-specific template from the model, develop subject specific growth trajectory and derive direct interpretations from the deformation field about the aging pattern. In this work, we propose a method to develop such an aging model for the adult human brain from cross-sectional data drawn from a specific population. Aging has been modeled as a time series regression. The time-series regression methods find the best fit model by minimizing a distance metric, that accounts for deviation of the regression model prediction with respect to the observations via optimization. One class of approach to time-series regression finds an optimal deformation path after selecting an initial image [149] and another class of approach jointly optimizes the metric and the initial image as it updates the selected initial image [138, 139, 144, 150]. Nevertheless, the initial image selection does have a notable influence on their result when an aging model is derived from cross-sectional data. Methods [140–143, 145, 146] are time series regression methods proposed for longitudinal data. The Global template is not relevant here as the same subject scans are considered at different time points. Method [148] also addresses longitudinal scans albeit from multiple subjects and develops the global aging model but only for a short age range of maximum 7 years.

In a cohort-based longitudinal study, the variability in inter-subject aging trends can also be high. This was handled in [151] by considering a tubular neighbourhood for the deformation. Alternatively, a powerful approach is to model individual changes as random effects and group changes as fixed effects, as demonstrated by Gerig et al. in [200]. This mixed-effects model effectively separates within-subject variations from between-subject differences, providing a comprehensive framework for analyzing complex longitudinal data in medical imaging. The spatio-temporal model suggested in [152] also considers similar variations due to diseased data points in the dataset and uses partial least squares regression to compute normal aging deformations; this gives modes of aging and corresponding scores for each subject. It has been reported [147] that a longitudinal change in signal intensity of different anatomical structures is a good indicator of aging. This has not been considered in the current work as it is outside the scope of our aging model. A cross-sectional design allows creation of larger data sets compared to that with longitudinal data. In aging studies with a cross-sectional design, the inter-subject variability within an age group and across age groups is disentangled to some extent by developing templates which represent subjects in some small age interval [154, 155, 178]. Several such template data are publicly accessible even though the image-sets used for template generation are not publicly available [155, 177, 178].

We are aware of only two reports that explicitly develop an aging model from cross-sectional data. In the first [157], an image regression approach based on weighted averaging is proposed for the aging model. In the second [183], the global template is derived from the given template data and the mapping between each of the template data point to the global template constitutes the aging model. The consequence of the second approach is that any comparison of a subject image with the global template space needs two transformations of the subject image; one from the subject image to the corresponding template data point and then to the global template image. Further, this is a departure from the notion of aging as a deformation process which acts on a template image [137].

We argue that an aging model represented by a set of image points developed by smoothly deforming a template image is more natural than a weighted average of image points in neighbourhoods. Hence given cross-sectional data, we explore the use of a diffeomorphic deformation of a template image as an aging model. In this work, we focus on developing the aging model from template data. The contributions of this work are: a method to derive i) a continuous aging model from cross-sectional data covering a long age span and ii) an aging model based on a diffeomorphic deformation of the global template; this is closer to the definition for an aging model in [137].

4.2 Methods

The proposed method derives an aging model from a given set of cross-sectional data for different age groups. The aging is modelled as a diffeomorphic deformation of the global structural template defined from all the images in the given data. The method requires only template data of a cohort instead of scans of subjects in the cohort as such scans are usually not publicly available.
The proposed aging model has two elements derived from the supplied templates: (i) a structural template for the brain and (ii) an aging deformation as a function of time defined on the structural template. The diffeomorphic aging is defined as a suitable deformation of the structural template. Computing the aging deformation, and mapping it to the structural template are the main steps of this method. The model derives temporally and spatially smooth deformations to minimize the effect of cross-sectional variations in the aging deformation computed from the cross-sectional data. These are discussed in detail below.

4.2.1 Computing the structural template

Template data points are used as input to derive the aging model. Closely and equally spaced data points, each of them generated from equal number of images is preferred. Let the template data T_i be the group average of images of subjects whose age is in the i^{th} interval and let us assume that we have N such data points. As each of the templates is derived from different sets of images, the template space defined for each set need not be the same and thus the aging path will be different for each T_i. Finding the common aging path from the unaligned $T_1, T_2, \cdots, T_N$ is the challenge here. The final aging model is defined using a template G constructed from the set of all T_is in the diffeomorphic space $\mathcal{G}$. The template G is the best structural representation of all the T_is, which is computed using a non-rigid group-wise registration method called SyNG proposed in [159]. SyNG iteratively computes the templates that minimizes the average distance from the template to each of the T_is on the diffeomorphic space $\mathcal{G}$, and the optimal template is G. The distance from this template to each of the T_i incorporates two aspects; the cross-sectional and aging deformations. The cross-sectional variations and aging deformations in the data affect G less as it is the template developed from the whole data covering the entire age range of interest. The template G can be considered as the global template for all T_is and considering it as the structural template element in the proposed model avoids biases toward any T_i. All the T_is are aligned to G using an affine

transformation before developing the model to make it affine invariant. This simplifies the model as an affine alignment can be done accurately from one template to another or to an image.

4.2.2 Computing the Aging Deformation

4.2.2.1 Assumptions made while computing the aging deformation

In order to compute the aging deformation from cross-sectional data, it is useful to understand the natural aging process from a physiological/structural perspective.We begin with the assumption that the data represents a cohort with some homogeneity in brain morphology. It is observed that in a mature human brain (from approximately 20 years), brain tissue regions shrink and the ventricular space increases with aging [160–162]. A key implication of this observation is that the deformation that the brain undergoes with normal aging is spatially and temporally smooth and topology is preserved as no new structure appears with aging. We can therefore assume that growth-induced deformation will be the smoothest and the most predictable among other types of spatial (cross-sectional variation) and temporal (atrophy) deformations. The log-Euclidean framework [163] covers such less-complex diffeomorphic deformations, and can be used to extract aging deformations from cross-sectional data. The space of diffeomorphisms is an infinite-dimensional manifold, and subject-images can be generated by applying a set of diffeomorphisms $\mathcal{G}$ on a template image. The log-Euclidean framework uses the locally Euclidean nature of the manifold to work with diffeomorphisms in a computationally efficient manner. This is defined by representing the diffeomorphism by Stationary Velocity Fields (SVF). Group exponential maps are generally used to compute the deformation ϕ represented by the SVF v, that is, $\phi = \exp(v)$.

4.2.2.2 Aging deformation modelled by two SVFs

Recall that we already have template data $\{T_i\}$ and their global representation G. The aging deformation is the second element in the aging model. As mentioned in before, G does not carry any information about the aging deformation. Mapping between G and T_is constitutes both aging and cross-sectional deformations. Therefore G cannot be used directly to extract the aging deformation from the T_is. We find T_M among the T_is that needs the smallest deformation to map to G. T_M is used as a reference data point to compute the aging deformation. The aging deformation computed with respect to T_M can be mapped to G fairly accurately as they are close. The SVFs $\{v_i\}$ that maps each T_i to G are computed first to find the reference template T_M. Let $\|v_i\|$ be a measure of the distance between G and T_i. Then the desired T_M is the template corresponding to the smallest norm $\|v_i\|$. In other words,

$$T_M = T_i \text{ where } i \text{ is such that } \|v_i\| = \min\{\|v_k\|, 1 \leq k \leq n\}. \tag{4.1}$$

The deformation $\exp(v_M)$ which maps T_M to G is used to map the deformation computed with respect to T_M to the common space. In the proposed model, the aging deformation is considered as a temporal relationship with a consistent trend between subsequent T_is, with T_M being considered

as the reference template. An example of consistent trend is the fluid-filled regions in a mature brain increasing in size with aging. This temporally consistent aging deformation is derived from the deformations between template pairs in the forward (f) and backward (b) directions. For instance, the deformations v_{j_f} between $(T_{M+(j-1)_f}, T_{M+j_f})$ for $j = 1, 2, \cdots, (N-M)$ are the SVF parameterizations for pairs in the forward direction. Similarly, the deformations v_{j_b} obtained by registering template pairs $(T_{M-(j-1)_b}, T_{M-j_b})$ for $j = 1, 2, \cdots, (M-1)$ are the corresponding SVF parameterizations for pairs in the backward direction. The spatial aging trends will be locally consistent and therefore, composing the forward/backward pairwise deformations can be used to extract the consistent trends in the deformation with respect to T_M in both directions. We propose to do this by composing the deformations sequentially using the Baker–Campbell–Hausdorff (BCH) formulation given in Eqn. 4.4 below. This allows compositions of group exponentials to be expressed as a single SVF. Let the velocity vector field obtained as a result of repeated application of BCH formula on the forward (backward) deformations be denoted as $\mathbf{v_{j_f}}$ ($\mathbf{v_{j_b}}$). The vector field $\mathbf{v_{j_f}}$ defines the single SVF parameterization of the forward deformation from T_M to $T_{(M+j)_f}$ and $\mathbf{v_{j_b}}$ defines the same for the backward deformation from T_M to $T_{(M-j)_b}$. These velocity fields are computed from Eqn. 4.2 and Eqn. 4.3 with an initialization of $\mathbf{v_{1_f}} = v_{1_f}$ and $\mathbf{v_{1_b}} = v_{1_b}$.

$$\mathbf{v_{j_f}} = \text{BCH}(\text{BCH}(\cdots(\text{BCH}(\mathbf{v_{1_f}}, v_{2_f}), v_{3_f}), ...), v_{j_f}), j = 2...(N-M), \tag{4.2}$$

$$\mathbf{v_{j_b}} = \text{BCH}(\text{BCH}(\cdots(\text{BCH}(\mathbf{v_{1_b}}, v_{2_b}), v_{3_b}), ...), v_{j_b}), j = 2...(M-1). \tag{4.3}$$

The BCH formula for a pair of forward deformations is given in Eqn. 4.4. Backward deformations can be computed in a similar manner.

$$\begin{aligned}&\text{BCH}(\mathbf{v_{(j-1)_f}}, v_{j_f}) = \log(\exp(\mathbf{v_{(j-1)_f}})\exp(v_{j_f}))\\ &= \mathbf{v_{(j-1)_f}} + v_{(j_f)} + \frac{1}{2}([\mathbf{v_{(j-1)_f}}, v_{(j_f)}]) + \frac{1}{12}([\mathbf{v_{(j-1)_f}}, [\mathbf{v_{(j-1)_f}}, v_{(j_f)}]] + [v_{j_f}, [v_{(j_f)}, \mathbf{v_{(j-1)_f}}]]) + \cdots = \mathbf{v_{j_f}}.\end{aligned} \tag{4.4}$$

Here, $[\cdot, \cdot]$ denotes the Lie bracket of two vector fields.

It should be noted that since the BCH approximation is valid only for small deformations, in practice, $v_{(j_f)}$ is divided into n smaller deformations such that $\frac{v_{(j_f)}}{n} < 0.5\times$ voxel dimension, and these smaller deformations are composed iteratively with $\mathbf{v_{(j-1)_f}}$ to compute $\mathbf{v_{j_f}}$. In the proposed method, the extracted deformation is constrained to be spatially smooth due to the log-Euclidean framework and temporally smooth since the composing step captures only the temporally consistent trends from the sequential data. For simplicity, the forward aging deformation from T_M to T_N, $\phi_f = \exp(\mathbf{v_{(N-M)_f}}t)$ is denoted as $\exp(\mathbf{v_f}t)$ and the backward aging deformation from T_M to T_1, $\phi_b = \exp(\mathbf{v_{(M-1)_b}}t)$ is denoted as $\exp(\mathbf{v_b}t)$. The computed aging deformations ϕ_f and ϕ_b vary uniformly with time which is not consistent with the natural aging trends whereas the aging deformation cannot be expected to vary uniformly, for example tissue degradation will be rapid for

elderly age range [162]. Hence, a temporal dependency is introduced in ϕ_f and ϕ_b to accommodate any non-uniform changes in natural aging. This step is explained in the next section.

4.2.2.3 Imposing non-uniform temporal variations on aging deformation

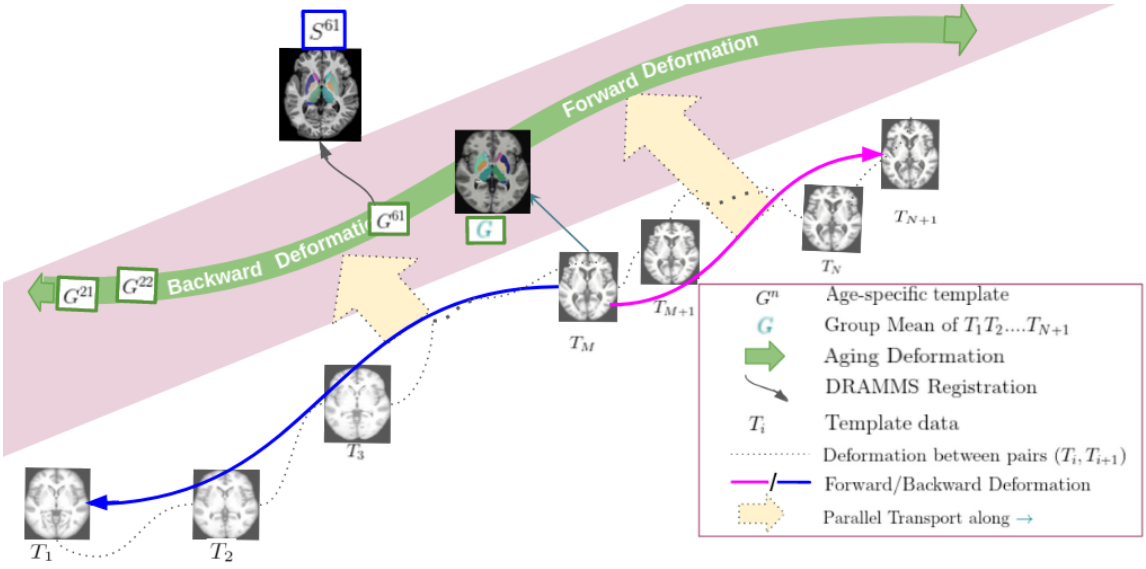

Figure 4.1: A schematic representation of the aging model. Included is an illustration of how the model maps a subject scan at age=61 years to the global space

The aging deformation need not increase linearly in time with respect to T_M. Hence we propose a quantification for the aging deformation (denoted as R) at each time point in Eqn. 4.5. This is defined in terms of the distance between T_i and T_M as in Eqn. 4.5. Here $\mathbf{v}^* = \mathbf{v_f}$ in the forward direction and $\mathbf{v}^* = \mathbf{v_b}$ in the backward direction. Further, $\mathbf{v_i} = \mathbf{v_{j_f}}$ for $i = (M+j)_f$ and $\mathbf{v_i} = \mathbf{v_{j_b}}$ for $i = (M-j)_b$. With this, let us define

$$R(i) = \frac{d(T_1, T_i)}{d(T_M, T_i)} = \frac{\|\mathbf{v_i}\|}{\|\mathbf{v}^*\|}. \tag{4.5}$$

Since $R(i)$ is a discrete sequence, whereas a continuous aging trend is of interest, a smooth curve $\gamma(t)$ is found by fitting a curve to $R(i)$. In our implementation, a cubic spline fitting was done in the forward and backward directions for the γ curve. The function $\gamma(t)$ for $t = [t_0, t_N]$, quantifies the aging deformation at a particular time point with respect to T_M. As this deformation increases in both directions with time, the curve will, in general, have a bilateral increasing trend about the age point corresponding to T_M. An illustration of the proposed method to extract the aging trends is shown in Fig. 4.1.

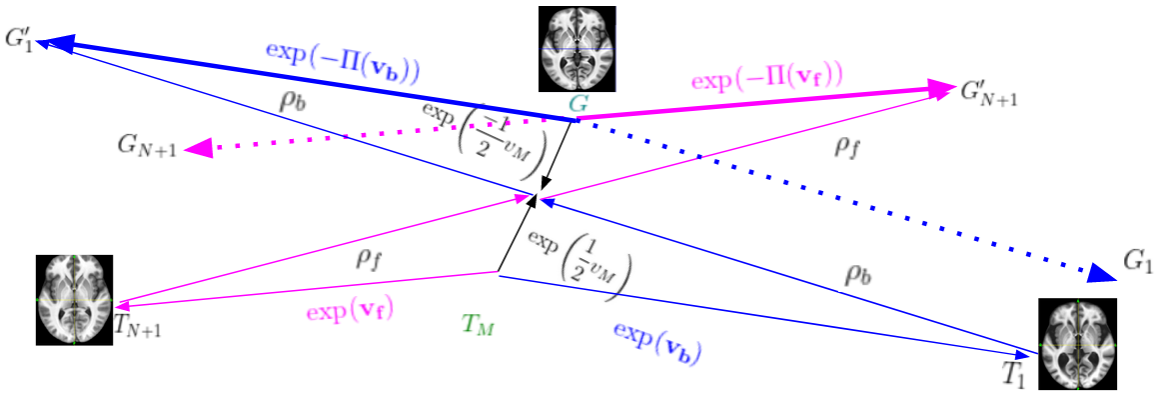

Figure 4.2: T_M is mapped to G using $\exp(v_M)$, and the path is used to transport $\exp(\mathbf{v_f})$ and $\exp(\mathbf{v_b})$ to the global template space.

4.2.2.4 Transferring the deformations to the global template space

The deformations captured using Eqn. 4.4 are mapped to the global template space using the mapping from T_M to G, i.e., $\exp(v_M)$. The captured deformations on the manifold $\mathcal{G}$ are parameterized by SVF. In order to transfer the aging deformations to the global template space we use an existing algorithm [164] for parallel transport. This is explained next.

Let the global template space images corresponding to T_is be G_is. The deformations to be transported are parameterized by SVFs $\mathbf{v_f}$ and $\mathbf{v_b}$. A schematic of the deformation mapping scheme is shown in Fig. 4.2. In Fig. 4.2, $G'_1 = G \circ \exp(-\Pi(\mathbf{v_b}))$ and $G'_{N+1} = G \circ \exp(-\Pi(\mathbf{v_f}))$. Thus, the inverse of the mappings from G to G'_1 and G'_{N+1} i.e., $\exp(\Pi(\mathbf{v_b}))$ and $(\exp(\Pi(\mathbf{v_f}))$ gives ϕ_b and ϕ_f respectively. Here $\rho_b = \exp\left(\frac{v_M}{2}\right) \circ \exp(-\mathbf{v_b})$ and $\exp(\Pi(\mathbf{v_b})) = \exp\left(\frac{v_M}{2}\right) \circ \rho_b^{-1}$. Therefore,

$$\exp(\Pi(\mathbf{v_b})) = \exp\left(\frac{v_M}{2}\right) \circ \exp(\mathbf{v_b}) \exp\left(\frac{-v_M}{2}\right), \tag{4.6}$$

and similarly,

$$\exp(\Pi(\mathbf{v_f})) = \exp\left(\frac{v_M}{2}\right) \circ \exp(\mathbf{v_f}) \exp\left(\frac{-v_M}{2}\right). \tag{4.7}$$

4.2.3 The aging model

The aging model has three components, G, $\gamma(t)$ and the SVF parameterization of the transported forward and backward deformations $\Pi(\mathbf{v_f}), \Pi(\mathbf{v_b})$ respectively. An age-specific template at any time point t can be computed using the following formula:

$$T(t) = \begin{cases} G \circ \exp(\Pi(\mathbf{v_f})\gamma(t)) \text{ for } t \geq M, \\ G \circ \exp(\Pi(\mathbf{v_b})\gamma(t)) \text{ for } t \leq M. \end{cases} \tag{4.8}$$

The aging model implementation has made publicly available in `http://dx.doi.org/10.17632/nw983x225c.1`.

Algorithm 1 Proposed Algorithm

Input: $T_1, T_2, \cdots, T_{N+1}$
Result: Aging Model (G, $\Pi(\mathbf{v_f})$, $\Pi(\mathbf{v_b})$, $\gamma(t)$)
Step 1: Compute the global template as group mean of $T_1, T_2, \cdots, T_{N+1} \longrightarrow G$
Step 2: Register G to T_i $\forall i \in [1...N] \longrightarrow v_i$
Step 3: Compute the distance $d_i = ||(v_i)||$ between G and each T_i
Step 4: Find T_i which is closest to G by comparing d_i values$\longrightarrow T_M$
Repeat Step 5 and **Step 6** for $(T_{(M+(j-1))_f}, T_{(M+j)_f})$ where $j = 1, 2...(N-M)$
Step 5: Register each pair $(T_{(M+(j-1))_f}, T_{(M+j)_f})$ using log-demons registration $\longrightarrow v_{j_f}$
Step 6: Single SVF parameterization of the composed aging deformation from T_M to $T_{(M+j)_f}$) using Eqn. 4.2 $\longrightarrow \mathbf{v_{j_f}}$
Repeat Step 7 and **Step 8** for $(T_{(M-(j-1))_b}, T_{(M-j)_b})$ for $j = 1, 2, \cdots, (M-1)$
Step 7: Register each pair $(T_{(M-(j-1))_b}, T_{(M-j)_b})$ using log-demons registration $\longrightarrow v_{j_b}$
Step 8: Single SVF parameterization of the composed aging deformation from T_M to $T_{(M-j)_b}$ using Eqn. 4.3 $\longrightarrow \mathbf{v_{j_b}}$ **Step 9:** $\mathbf{v_f} \longleftarrow \mathbf{v_{(N-M)_f}}$ and $\mathbf{v_b} \longleftarrow \mathbf{v_{(M-1)_b}}$
Step 10: Parallel Transport $\mathbf{v_f}$, $\mathbf{v_b}$ along v_M using Eqn. 4.6 and 5.4 respectively $\longrightarrow$ $\Pi(\mathbf{v_f})$, $\Pi(\mathbf{v_b})$.
Step 11: Compute a curve fitting for the discrete function R defined by Eqn. 4.5 using $\mathbf{v_{j_f}}$, $\mathbf{v_{j_b}}$, $\mathbf{v_f}$ and $\mathbf{v_b}$ $\longrightarrow \gamma(t)$

The entire procedure for comparing aging models is summarized in the flowchart shown in Figure 4.3.

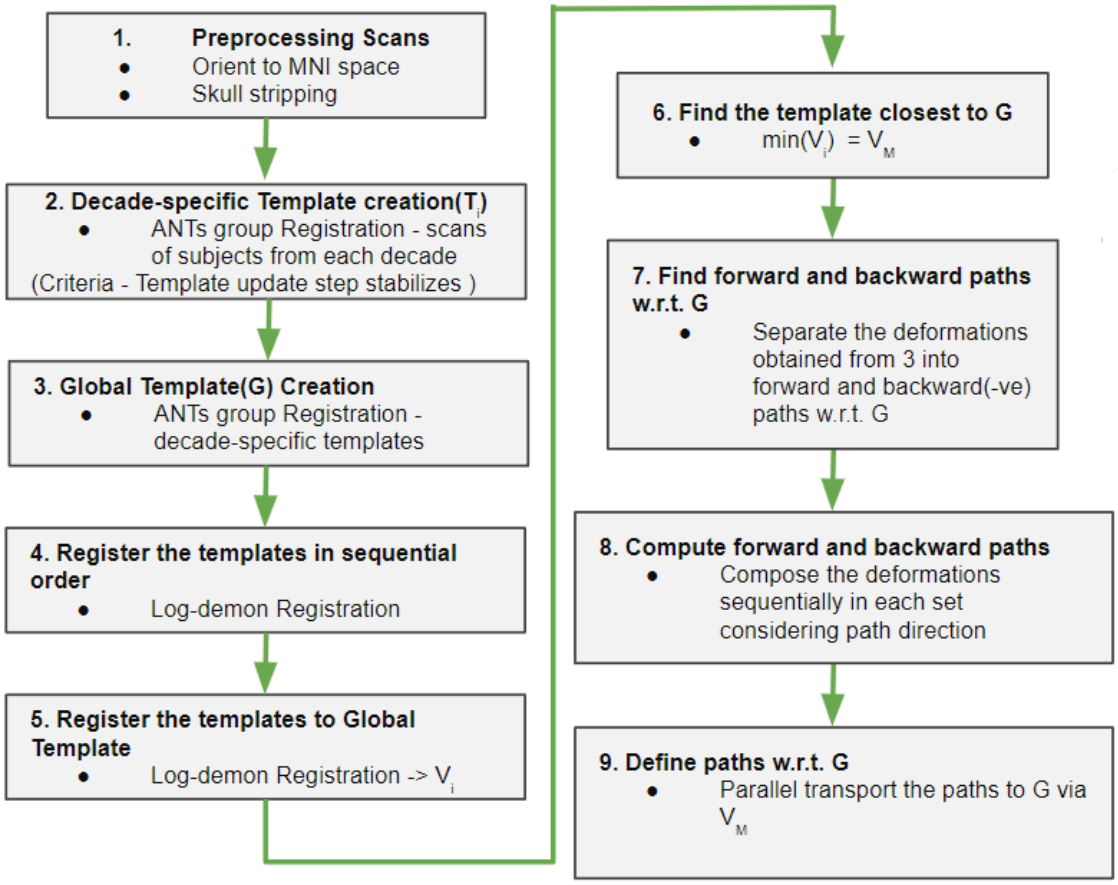

Figure 4.3: Aging model Creation Pipeline

4.3 Results

In this section, we report on validation of the proposed model and experiments with the model. All experiments, barring the one with simulated data, were done on 3D data though only 2D central slices from the results are shown for visual comparison. The proposed aging model is affine invariant, and therefore results were also aligned using affine transformation prior to comparison. The proposed method to create an aging model was implemented using two cross-sectional template datasets: (i) Brain Imaging of Normal Subjects (BRAINS) [177] with 7 templates of subjects aged 25-93 years and (ii) Neurodevelopmental MRI Database (Neurodev) [178] with 14 templates of subjects aged 20-89 years. T1 scans were used in both datasets and more information regarding the subject scans can be found in [177, 178]. Only templates are accessible in these datasets along with information on the age interval and number of scans of subjects were used to create each template. In BRAINS, the sampling of the age range is not uniform, particularly at the upper age level, and the number of scans used for template data creation is less relative to Neurodev. The spacing between template data is shorter (5 years) and uniform in Neurodev. Experiments done to assess and validate the quality of representation of the proposed model.

4.3.1 Aging Model

Recall that the proposed aging model has two elements, namely, the structural template G and the aging deformation. The aging deformation has three components: the forward aging deformation ϕ_f parameterized by $\mathbf{v_f}$, ϕ_b parameterized by $\mathbf{v_b}$ and the γ function. The proposed model developed with Neurodev and BRAINS datasets are shown in Fig. 4.4. A direct interpretation of $\gamma(t)$ plot does not give much information about the aging trend as it represents the degree of deformation with respect to G, rather than any of the end point templates. It however does indicate the age point that corresponds to the reference template T_M. In the case of Neurodev this is 67 years and for BRAINS it is 77 years.

4.3.2 Representation Quality Analysis

Age-specific templates were generated with the proposed aging model using Eqn. 5.2, and were used for visual comparison to assess the quality of representation. Comparisons are done with natural aging trends, existing spatio-temporal atlas and the supplied templates used for model creation.

4.3.2.1 Compatibility with Natural Aging

Templates at increasing age points were generated with the proposed aging model to study the structural change with aging. The BRAINS dataset [177] was chosen to do this experiment as it covers a longer span at the elderly age end where more changes are expected. Human brain aging literature [162, 165, 166] indicates that a mature brain undergoes minimal cognitive and structural changes up to the age of ≈ 50 and more for the elderly, i.e. $\approx 60+$. This trend was verified by computing the intensity difference between the current template and the first (at age 30) template.

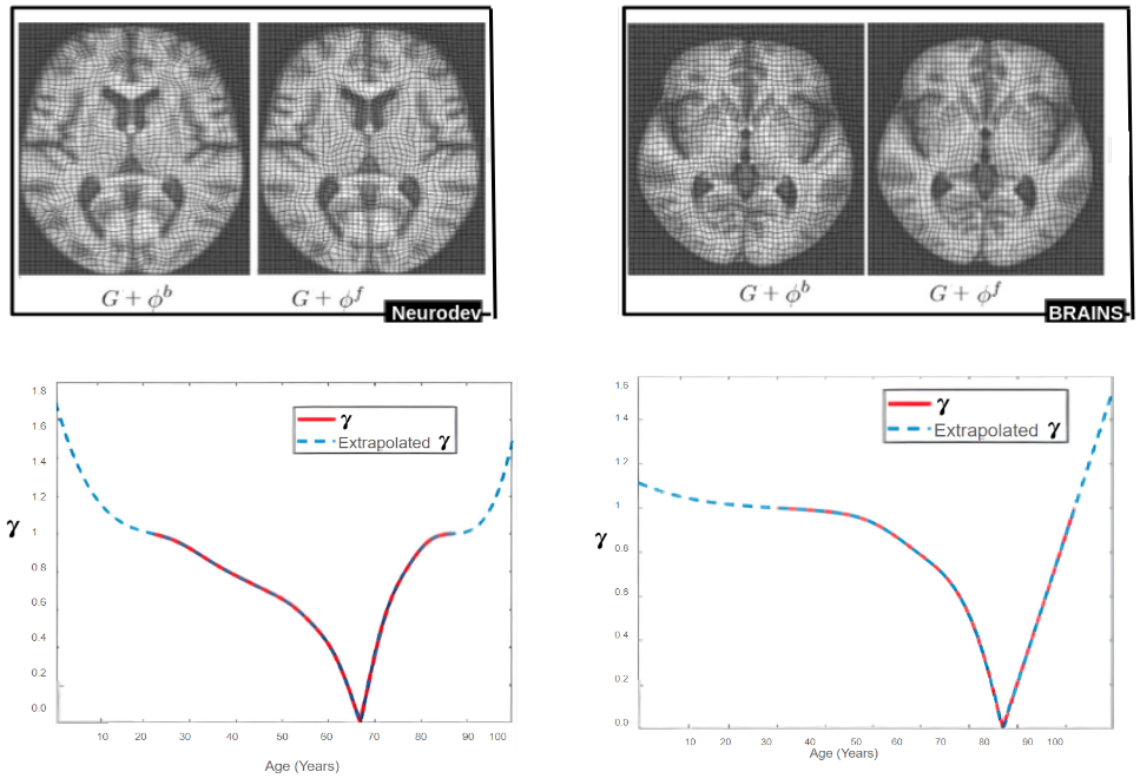

Figure 4.4: The aging model computed with Neurodev and BRAINS datasets

This difference essentially is due to age-induced structural change.

Fig. 4.5 shows the generated sequential templates (first row) and difference between the sequential templates and the first template (second row). The difference images facilitate understanding the structural changes with aging. The difference appears to be very low for the first few decades relative to the last few decades where changes like ventricular expansion occurs. This trend is consistent with the existing information about natural healthy aging.

4.3.2.2 Growth Trend across Aging Models

Huizinga et al. in [152] proposed a cross-sectional spatio-temporal reference model for representing aging. This model does not ensure a diffeomorphic aging deformation and the template space representation of a subject image needs a computationally intensive group-wise registration with a training set used to generate the model. In contrast, our model requires only one pairwise registration from a subject to the corresponding age-specific template, derived from the model. The aging trends observable in the templates derived from our model was compared with those derived using [152]; the latter templates are available in `http://www.agingbrain.nl/` for the age range of 45-92 years. Templates at the same age points were generated with the proposed method using the Neurodev dataset.

Fig. 4.6, shows sample 2D slices of templates from [152] in odd numbered rows, along with the ones

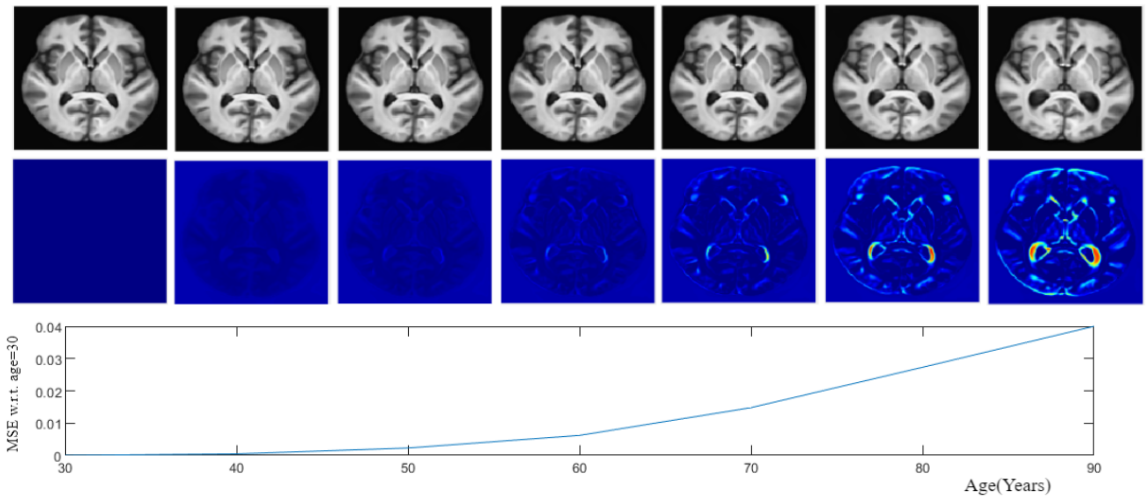

Figure 4.5: The proposed aging model at different time points(first row) along with the difference image with respect to the initial time point(second row)

derived with the proposed model (from the Neurodev dataset) in even numbered rows, for comparison. The comparison at image-level comparison is not meaningful as the templates are generated from different data-sets. However, one can observe growth trends. The structural similarity across rows in a column appear to have similar trends across age indicating growth trend to be consistent.

4.3.2.3 Age-specific Template Assessment

The generated templates with our model were visually compared with the templates given in the Neurodev dataset to understand how well the model have represented these templates. The templates for the first and last time points in our aging model have undergone maximum deformation compared to those at other age points. Hence, such a visual comparison is of interest. The given templates along with our generated templates are shown in Fig. 4.7 for comparison. The first and last time points for Neurodev are shown as the first image in each pair, while the corresponding templates generated by the proposed model are shown as the second image in each pair. As per the proposed aging model, the template for the first and last time points are maximally deformed with respect to the template closest to G, i.e., T_M. Yet, the derived templates are visually quite similar to the templates from the two datasets. Thus, the proposed model appears to preserve the structural details of the given template at each time point. We assessed the interpolation/extrapolation capability of the proposed model and observed that the derived templates are qualitatively and quantitatively similar to given templates. Thus, the model is quite robust to missing data.

4.3.3 Aging Model Validation

Model validation was done by analysing the ability of the model to capture natural deformations and the similarity of model-generated age-specific templates to a set of subject images of same

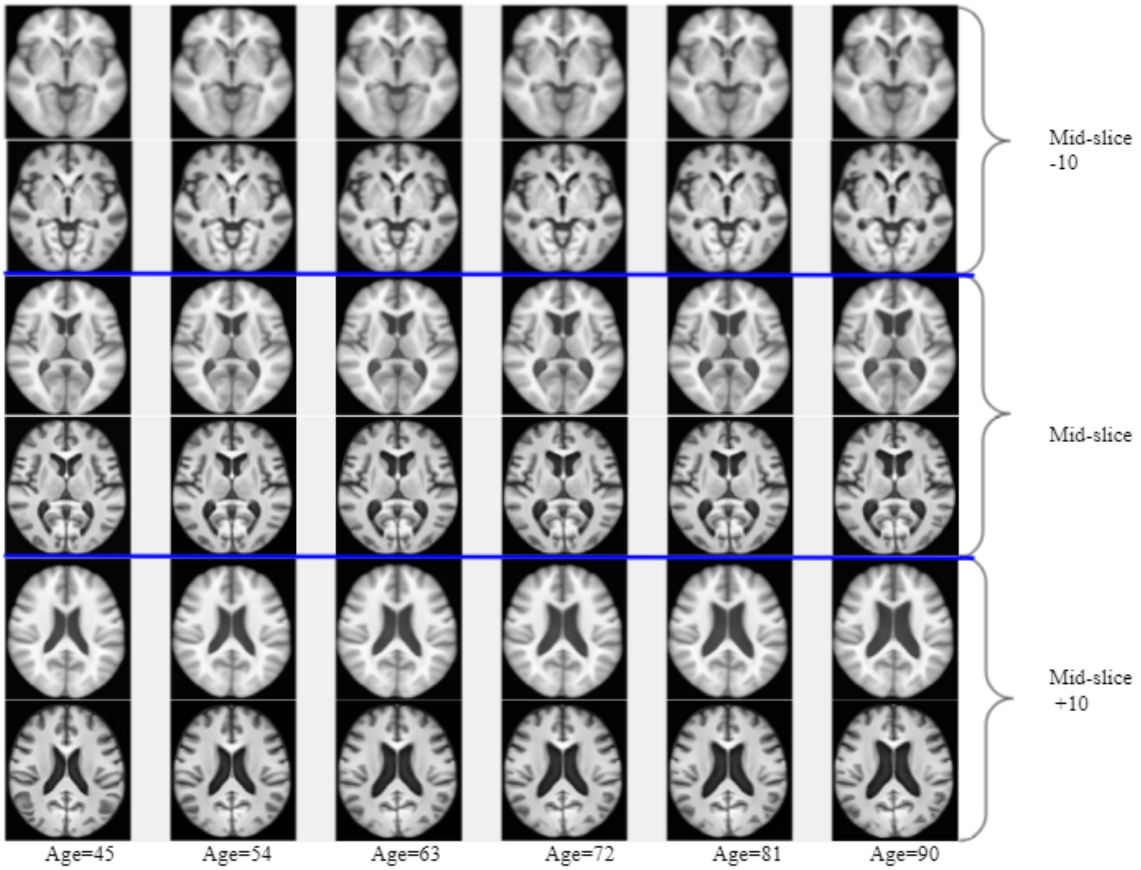

Figure 4.6: Correctness of Aging trends captured in the model: Publicly available spatio-temporal images [152](row 1,3,5) compared with images generated at same time points with proposed aging model using Neurodev data at different time points(row 2,4,6) Each highlighted row pairs compare same slices as specified in the figure.

age. Since our model was derived for a cross-sectional setting, we also studied its performance in a longitudinal data setting as it is of interest.

4.3.3.1 Topology Preservation

Since diffeomorphic deformations best fit *natural* deformations, we considered aging related deformation also as a diffeomorphism. Accordingly, our model is defined on a manifold $\mathcal{G}$ of diffeomorphisms. It is of interest to verify if an extrapolation of the model generates deformations in $\mathcal{G}$ itself. This was done by extrapolating the aging trend and deriving templates in both younger and older ages. Neurodev data which covers that age range of 22-87 (reference template age point, M=77 years) is used for this experiment. The templates from extrapolation in both directions were generated for this experiment with Eqn. 5.2. Two templates, namely at age 20 and age 100, generated with the proposed model are shown in Fig. 4.8 along with the Global template. These are results of extrapolation from the data given in the Neurodev dataset [178]. The topology appears to be preserved even when the aging model is extrapolated in both directions implying that the extrapolated deformations also belong to $\mathcal{G}$. It can also been that while global similarity (in structure) exists across age, local deformations persist. For instance, the ventricle is much smaller at age 20 and enlarges with age, consistent with the expected aging trend. The Jacobians of the forward and backward deformations were verified to be positive valued.

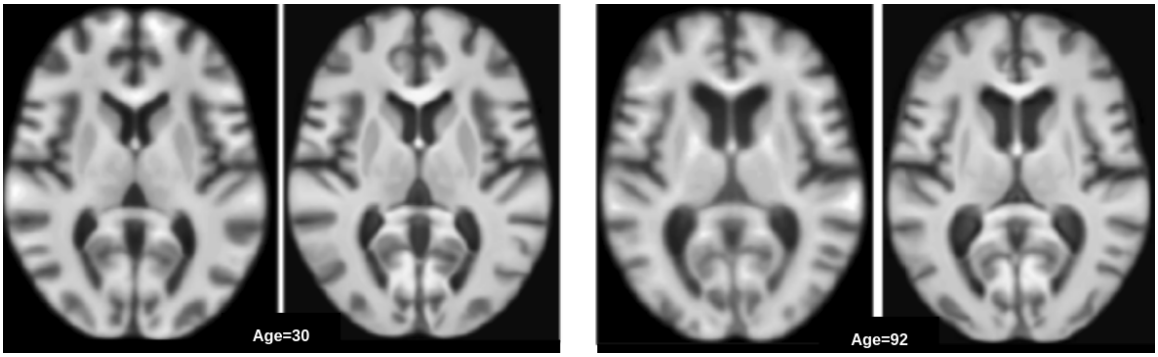

Figure 4.7: Comparison of templates(first image in each pair) given in the Neurodev dataset with those generated by the proposed aging model(second image in each pair). Only the templates for the first and last time-points are shown.

4.3.3.2 Validation with Segmentation

A localised assessment, i.e., of few structures, is of interest in many situations. This requires labeling by aligning the subject image to a labeled template and doing a label transfer. An alignment process that requires smaller deformations indicates that the template is structurally very close to the subject image. This will lead to better segmentation. With our age model, this involves only a single registration step as shown in Figure 4.1 and hence potentially least deformation. This is in contrast to the steps required when using the model in [183] which requires two registration steps: one to

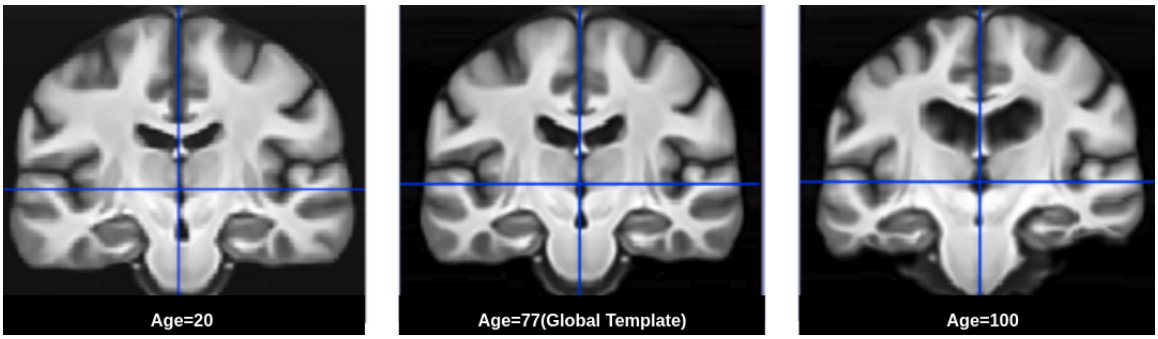

Figure 4.8: The central coronal slices of extrapolated age-templates are shown along with the global template image

transfer the labels from the global template to the template data that is closest to the given subject age, and a second to transfer the template labels to the subject image. Each of these registration steps can contribute to error in labeling in addition to the structural dissimilarity of template and subject image. An experiment was done to quantitatively compare the accuracy of labeling using the proposed method and with [183]. From MICCAI 2012 dataset [167] 35 subject images in 18-90 age range along with the ground truth labels were used to perform the comparison. The templates corresponding to the subject ages outside the range [22-87] years, were constructed by extrapolating the proposed aging model. The accuracy of label transfer from a template is highly influenced by the registration method and the global template labels being used. For a fair comparison, both models were developed with Neurodev [178] templates and the labeled G was taken to be identical. Both methods used DRAMMS-based registrations [168] with identical parameters for label transfer steps. The Dice score was used for assessing the segmentation accuracy.

Figure 8 shows the dice scores and volume comparison for 14 sub-cortical structures for our model and [183]. Results of direct label transfer from [136] and G are also included as baseline as [136] is the atlas used to label G and that labelled G is used by proposed method and [183] as starting point. It should be noted that in [183] a manually labeled G is used unlike our case. It can be observed that in terms of dice and volume the proposed model performs better than both baseline methods and [183] for large structures. Whereas for small structures the label transfer from G performs better than the rest three. The proposed model's better performance in label transfer is due to its ability to generate accurate age-matched (to the subject) template unlike [183] which only allows an approximate age match along with an extra registration step. The p-values computed between dice values with our method and with [183] was less than 0.05 for all structures except left Amygdala. From the visualized segmentations, the results of our aging model are closer to the ground truth and smoother (less spikes and missing pixels) compared with [183].

The segmentation performance of the proposed model and [183] were found to be different for the 2 datasets. A 10% improvement in average dice score is achieved with the proposed model with the Neurodev dataset while this figure is much higher for [183]. This indicates the superior robustness of the proposed aging model to change in sampling of the age range.

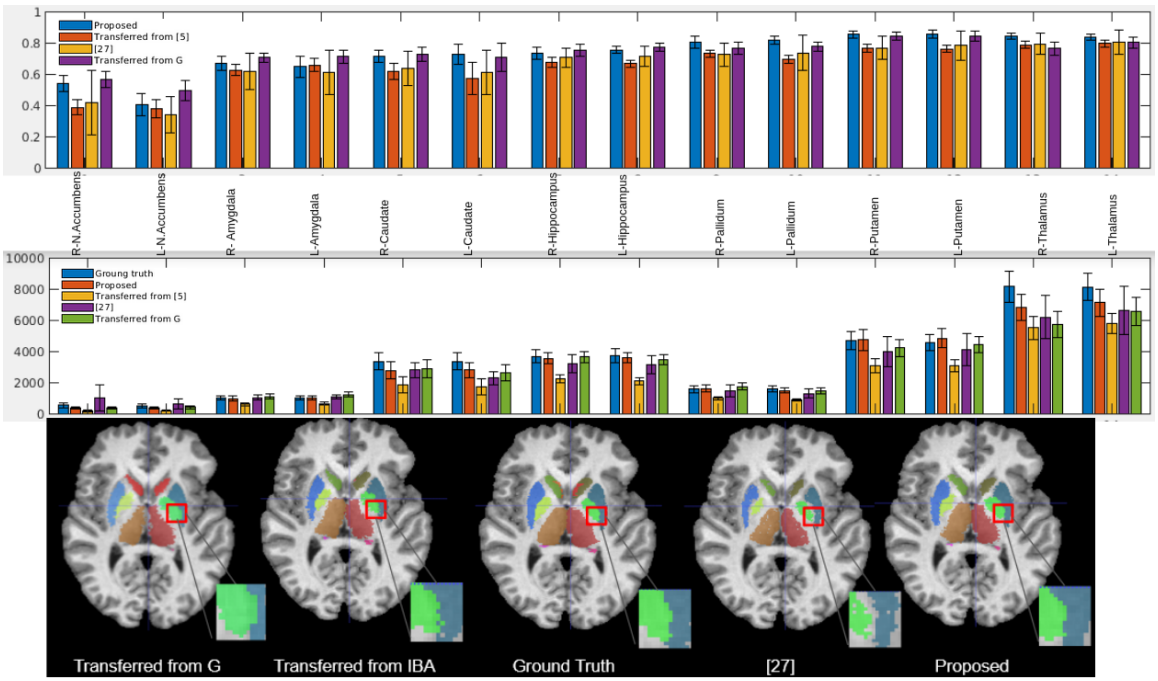

Figure 4.9: Segmentation performance comparison of proposed method with [183], Labels transferred from G and Labels transferred from [136]. The average dice (first row) and volume (second row) are plotted for 14 structures. lllustration of the transferred segmentations in last row

4.3.3.3 Validation with Simulated Longitudinal Data

The proposed method was aimed at handling cross-sectional data. In order to understand how the model would handle longitudinal data, an experiment was done using simulations as longitudinal data is unavailable. The Shepp-Logan phantom was used for this purpose and the deformed phantoms were generated as follows. A few locations on the image were chosen and each selected point and its neighborhood were displaced in X and Y directions; the displacement value was sampled from a Gaussian distribution. The degree of deformation is controlled by the parameters of the Gaussian. A set (S) of fifty randomly deformed phantoms were taken (to simulate a cohort) and five copies were made. Deformations with increasing degree was applied on these five copies to simulate aging of different subjects. The five sets thus form our longitudinal data. For each of the five sets a template was computed separately using the method suggested in [170]. The templates were then used as inputs for the proposed model to generate templates at different age points. These were then compared against the deformed versions of the Shepp-Logan phantom (proxy ground truth). Sample images generated by applying the simulated deformations on the Shepp-Logan phantom are shown in the first row of Fig. 5.3. This forms the ground truth. The template images derived with the proposed model are shown in the second row. The images in the 2 rows appear to be very similar to each other at the same time points. The template images generated with the proposed model and corresponding γ curve is also shown in the same figure. The degree of deformation in the simulated deformation is uniformly increasing with time and hence it can be expected that the γ curve will be

symmetric with respect to mid-time point. We see that, in Fig. 5.3, is indeed true. The proposed model captures the applied deformation without much errors from the simulated longitudinal data. TER

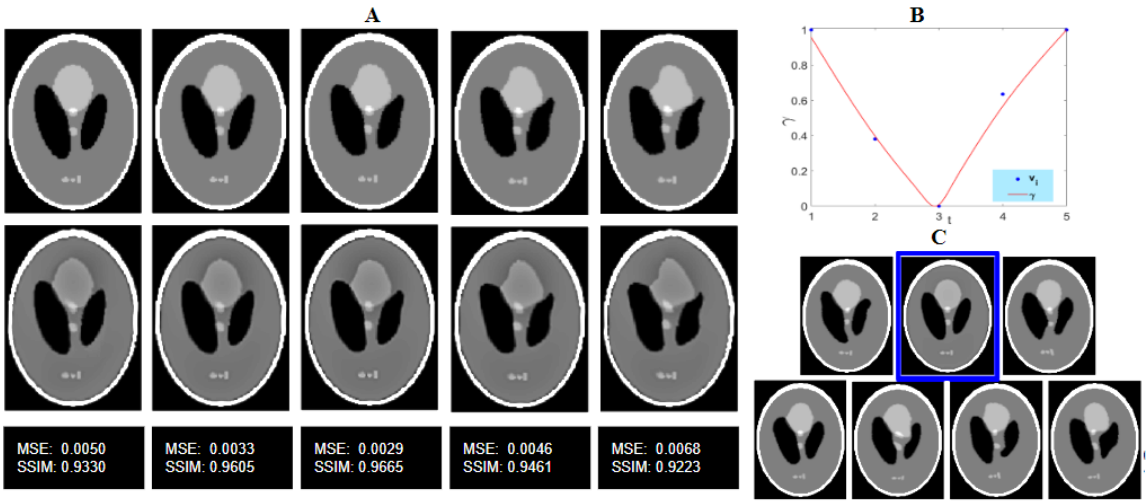

Figure 4.10: Aging model for a simulated longitudinal dataset. A - First row: Deformed images with known transformation and second row: images generated with the proposed model, for the same time points (as in the first row) and last row: the MSE and SSIM of first and second rows; B - The γ curve of our aging model and C - Some sample images used in S

4.4 Discussion

Cross-sectional images at different age points are easier to acquire than that of the same subject. This motivated us to develop a method to generate an aging model using cross-sectional data. The aging model is based on continuous deformation applied to a template. Experimental results show that our aging model can be used to generate templates at different time points in a manner that is consistent with the natural aging trend observed by other studies; it preserves structural details of the supplied templates and generates topology-preserving aging deformations.

The proposed aging model has a few limitations. Firstly, it is applicable only for matured brain growth where no new brain structures are introduced. The quality of the proposed model is completely dependent on the data. Consequently, the number of scans in each age interval needs to be large to generate the template data that are representative of the cohort/population under study. Though the definition of 'large' remains open, current studies have typically used 20 or more scans at every interval. Secondly, while the model reduces the effect of cross-sectional data induced variations in the aging deformation, there is no formal proof as yet that it completely removes the cross-sectional variation. Finally, the proposed aging model defines a single average growth path and does not attempt to model the cross-sectional aging variations.

Since the proposed model works only to obtain a mean aging path, future work can be a refinement

in terms of defining the aging model as a distribution of paths about the average path. The basic requirement to develop such a model however, is the availability of scans at different age points, not the templates alone. Our current work is directed at developing a public database for this purpose with subject scans at different age points.

The spatio-temporal smoothness and consistency are assured in the proposed model to make it closer to natural aging. The model has the potential to be used for clinical purposes. Currently population specific aging trends are of interest and this can be generated with the proposed model with less efforts. The code to generate proposed the aging model has made publicly available in `http://dx.doi.org/10.17632/nw983x225c.1`.

Chapter *5*

A Metric to Quantify Difference in Aging across Populations

Biological processes like growth, aging, and disease progression are generally studied with follow-up scans taken at different time points, i.e., with image time series (TS) based analysis. Comparison between TS representing a biological process of two individuals/populations is of interest. A metric to quantify the difference between TS is desirable for such a comparison. The two TS represent the evolution of two different subject/population average anatomies through two paths. A method to untangle and quantify the path and inter-subject anatomy(shape) difference between the TS is presented in this work. The proposed metric is a generalized version of Fréchet distance designed to compare curves. The proposed method is evaluated with simulated and adult and fetal neuro templates. Results show that the metric is able to separate and quantify the path and shape differences between TS.

5.1 Introduction

Studying natural processes such as growth, disease progression, and other physiological processes often requires imaging at different time points, thus generating an image time series (TS). The images in such TS typically represent a deforming organ of an individual or population average anatomies derived to represent the general trend of a process. Modeling the TS as a continuously deforming image/*shape* though a temporal *path* [139, 149] helps to directly analyze the deformation happening in the anatomy with time [137]. However, it is a fact that anatomy and the biological process vary across individuals. When two TS are of individuals from the same population, it is presumed that there is anatomical (or *shape*) similarity, and for a population-level analysis with a group of TS, the focus is on understanding the *path* difference directly or by mapping to a common space [82]. For a pair of TS, both *shape* and *path* difference will significantly contribute towards the difference between them, and it has to be captured by a metric that defines the distance between them. It is more interesting to study these separately when comparing two population average TS. Let us consider an analogous problem to understand the requirement of such an analysis better. Consider the growth of two chilies represented by two TS. Each chili will have a unique *shape* that changes as it grows. Chilies of the same variety will be similar in shape, whereas those of different varieties will not, as in the case of long versus round chili varieties. Consequently, comparing

the growth of two long chili varieties requires only understanding the course of temporal variation, whereas comparing the growth of a round variety and a long variety chili also requires accounting for the basic shape difference between the two varieties. We define the *shape* variation between TS to represent the time-independent variation between the TS pair and the *path* variation to represent the time-dependent variation between TS. This work proposes a method that separately quantifies the *shape* and *path* variation to define the distance between two TS.

Image similarity metrics such as SSIM and MSE are popular for image-level comparisons. They are inappropriate for image TS because they fail to quantify spatial and temporal differences separately. The terminology 'path difference' is generally used to compare two 1D curves, where the initial points in both curves are assumed to be the same. Hausdorff distance [73] is a common metric to measure the distance between two curves, but it does not consider the course of the curves. Dynamic time Warping [75] aids in comparing two trajectories of different speeds, but it is also a discrete measure. Fréchet distance [80] is the standard for comparing two continuous curves or paths. The idea of Fréchet distance is defined in [80] as the minimum leash length when a person walks with a dog on a leash forward, from start to end. In image TS representing biological processes, the spatial context is as important as the temporal variation, but Fréchet distance (FD) [72] is not designed to handle these directly. In general, none of the existing methods for curve comparison are directly applicable to compare and quantify 3D image TS differences.

3D-image-based qualitative and quantitative comparison of biological process in the existing literature is limited to characteristics like cerebral volume and dimensions of the brain, which are derived from each TS [76, 184, 194, 195]; this translates to image level comparison for 3D image TS. Such analysis, however, will not help to separately compare the *shape* variation and *path* variations. Measures like changes in volume and structure/organ dimensions have been reported but cannot capture the non-rigid anatomical changes. For instance, growth trajectories have been compared in [82] to study the difference between the human brain in healthy/normal individuals and those with Alzheimer's disease by first mapping the trajectories of two groups of individual follow-up scans to a common space in [82] and then performing a volume change analysis. Such methods are useful for case-specific group analysis, but a metric that defines the distance between two TS will facilitate a more general analysis framework.

5.1.1 Our Contribution

The main contribution of this work is a metric for comparing a pair of TS, which considers both *shape* and *path* variations. To our knowledge, this has not been addressed in the context of group analysis. We propose a metric to quantify *path* variation inspired by the idea of FD for curves because FD considers the course of the path, unlike other measures, and defines a single metric to quantify the *path* variation. We also propose a metric to quantify *shape* variation based on the deformation-based distance between the *shape*s of the individual TS. Proposed *shape* and *path*

distance metrics are defined for every point in 3D space. The sum of the average *shape* and *path* distances quantifies the difference between the two TS.

5.2 Method

TS data corresponds to either an individual anatomy variation or average population anatomy variation with time. Henceforth, the term 'subject' is used generically to refer to both an individual or a population average. It should be pointed out that affine invariant, intensity normalized image TS are considered in this work as these factors are separately quantifiable.

5.2.1 Assumptions

Let TS_1 and TS_2 be two TS acquired from two different subjects for approximately the same time range at different/same time instances. I.e., the two TS are aligned with respect to each other in terms of time. The foremost challenge in TS comparison is the discrete nature of the TS. We propose to overcome it by deriving continuous models corresponding to each TS as a first step.

5.2.2 Deriving continuous representation of TS

A natural process in the human body can be considered as a deformation happening on the underlying anatomy [137]. When images are acquired from the same subject, the TS is modeled as an anatomy deforming through a path. Kernel-based regression [77] is another modeling option which however does not separately model the path and the underlying anatomy. Since the purpose is to separately quantify the difference in terms of *shape* and *path* variation between two TS, we choose a path-based modeling approach such as [179] where the TS is modeled as the continuous deformation of a global anatomy. The global anatomy (G) lies around the middle of the time interval and hence a forward($\exp(\mathbf{v_f} \cdot \gamma(t))$) and backward ($\exp(\mathbf{v_b} \cdot \gamma(t))$) time-varying deformation of G models the continuous image path, where γ represents the temporal changes of the deformation. The 2-piece path modelling helps to match the time interval of the two TS via extrapolation of the model towards the required time points as shown in Figure 5.1. To model the continuous image path with [179] the G has to be generated first. The type of the TS being used for comparison has to be considered to derive the G.

For Cross-sectional data based population comparison, [179] can be followed to derive the continuous image path. This model is applicable for population average TS derived from cross-sectional data. The global anatomy (G) in [179] represents the anatomy that normalizes all inter-subject variation and the temporal variation. If the TS is longitudinal data then G generation is not needed as the same subject is being scanned. Hence, select a central image in each series and the forward and backward time deformation of the central image models the TS. Except the G generation, the other steps will be same for longitudinal data.

The derived representation of TS_1 and TS_2 with [179] are $I_1(t)$ and $I_2(t)$ as given in Equation 6.1-5.2. G_1 and G_2 represents the global anatomy in the continuous models of TS_1 and TS_2. It should be noted that, $*$ corresponds to f and b subscripts throughout this chapter, where f corresponds to forward and b to backward. The $\mathbf{v}_{*_\mathbf{1}} \cdot \gamma_1(t))$ and $\mathbf{v}_{*_\mathbf{2}} \cdot \gamma_2(t))$ corresponds to forward/backward path representations in the models correspond to TS_1 and TS_2. The global anatomies $G_1(G_2)$ occurs at $m_1(m_2)$.

$$I_1(t) = \begin{cases} G_1 \circ \exp(\mathbf{v_{f_1}} \cdot \gamma_1(t)) \text{ for } t \geq m_1, \\ G_1 \circ \exp(\mathbf{v_{b_1}} \cdot \gamma_1(t)) \text{ for } t \leq m_1. \end{cases} \tag{5.1}$$

$$I_2(t) = \begin{cases} G_2 \circ \exp(\mathbf{v_{f_2}} \cdot \gamma_2(t)) \text{ for } t \geq m_2, \\ G_2 \circ \exp(\mathbf{v_{b_2}} \cdot \gamma_2(t)) \text{ for } t \leq m_2. \end{cases} \tag{5.2}$$

5.2.3 Temporal alignment of the continuous representations

The models are derived separately for each TS as given in Equation 6.1-5.2. The G_1 and G_2 occurs at m_1 and m_2 respectively. To temporally align the two models the global anatomies has to be moved to the same time point. Then the models can be reformulated with new global anatomies G_1' and G_2' at $(m_1 + m_2)/2$. Suppose $m1 < (m_1 + m_2)/2$ and $m_2 > (m_1 + m_2)/2$. Then G_1' and G_2' are given by Equation 5.5 and 5.4 respectively.

$$G_1' = G_1 \circ \exp(\mathbf{v}_{*\mathbf{1}} \cdot \gamma_1 \left(\frac{m_2 - m_1}{2} \right)) \tag{5.3}$$

$$G_2' = G_2 \circ \exp(\mathbf{v}_{*\mathbf{2}} \cdot \gamma_2 \left(\frac{m_1 - m_2}{2} \right)) \tag{5.4}$$

The updated deformations are given by Equation 5.5 - 5.8. In order to relocate the G_1 and G_2 to $(m_1+m_2)/2$, the deformations has to be updated. Composition steps are required to map part of the forward or backward deformation towards the other side to keep global anatomy at $(m_1 + m_2)/2$. The updated deformations are given by Equation 5.5 - 5.8.

$$\mathbf{V_{b1}} = \mathbf{v_{b1}} - \mathbf{v_{b1}} \gamma_1 \left(\frac{m_2 - m_1}{2} \right) \tag{5.5}$$

$$\mathbf{V_{f1}} = \log \left(\exp(\mathbf{v_{f1}}) \circ \exp(-\mathbf{v_{b1}} \gamma_1 \left(\frac{m_2 - m_1}{2} \right)) \right) \tag{5.6}$$

$$\mathbf{V_{b2}} = \log \left(\exp(\mathbf{v_{b2}}) \circ \exp(\mathbf{v_{b2}} \gamma_2 \left(\frac{m_1 - m_2}{2} \right)) \right) \tag{5.7}$$

$$\mathbf{V_{f2}} = \mathbf{v_{f2}} - \mathbf{v_{b2}}\gamma_2 \left(\frac{m_1 - m_2}{2} \right) \tag{5.8}$$

Equation 5.6 and 5.7 are computed with BCH formulation. For two deformations modelled with SVFs v_a and v_b, the composition of the two deformations is derived as given in Eqn. 5.9. This approximation is done with the assumption that v_b is very small. Hence proposed method will work only if the TS is from approximately the same time interval.

$$\log(\exp(v_a) \circ \exp(v_b)) = v_a + v_b + \frac{1}{2}([v_a, v_b]) + \frac{1}{12}([v_a, [v_a, v_b]] + [v_b, [v_b, v_a]]) + \cdots \tag{5.9}$$

The γ_1 and γ_2 has to be recomputed by fitting a smooth spline curve on their old values and new values around $t = \frac{m_1+m_2}{2}$. Let the new fitted γs be γ_1' and γ_2'. The continuous models is extrapolated /truncated to the same time interval before comparing the two. Figure 5.1 shows the steps to be followed to derive the continuous temporally aligned, range compensated continuous models from the TS., which are used to compute the distance between the pair of TS.

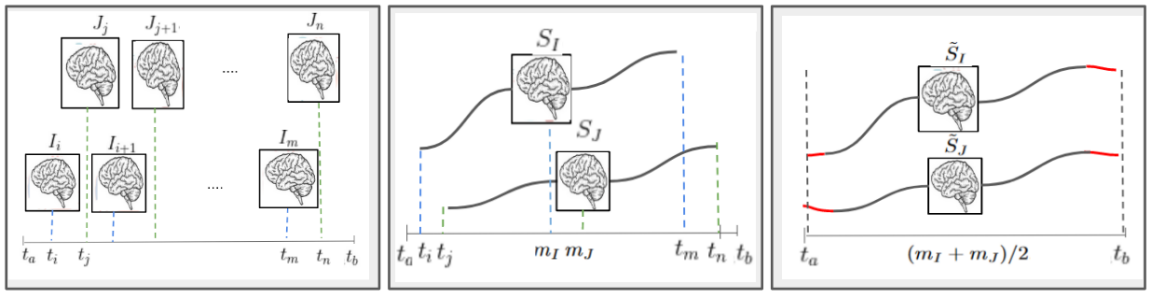

Figure 5.1: A) Temporally aligned TS_1, TS_2, B) Continuous image paths $I_1(t), I_2(t)$ C) Temporally aligned paths with extrapolated deformation(red curve)

5.2.4 Computing the *shape* and *path* distance

5.2.4.1 *Shape* distance:

In the continuous models for the two TS, $\tilde{S}_I$ and $\tilde{S}_J$ represent the *shapes* corresponding to TS_1 and TS_2, respectively, at the same time point. Hence, the deformation between the $\tilde{S}_I$ and $\tilde{S}_J$ captures the *shape* variation ϕ_S between the two TS. Since the deformation is modeled as $\phi_S = \exp(\mathbf{V}_S)$, with $\mathbf{V}_S$ representing a stationary velocity field, the norm of this vector field can be directly used to quantify the deformation as given in [96]. The *shape* distance (d_s) between TS_1 and TS_2 is hence defined as

$$d_s = \|\mathbf{V}_S\| \tag{5.10}$$

5.2.4.2 *Path* distance:

Our aim is to enable the comparison of a pair of TS on a common interval $[t_a, t_b]$, which can be flexibly selected. Extrapolation or truncation may be required, depending on the selected time interval.

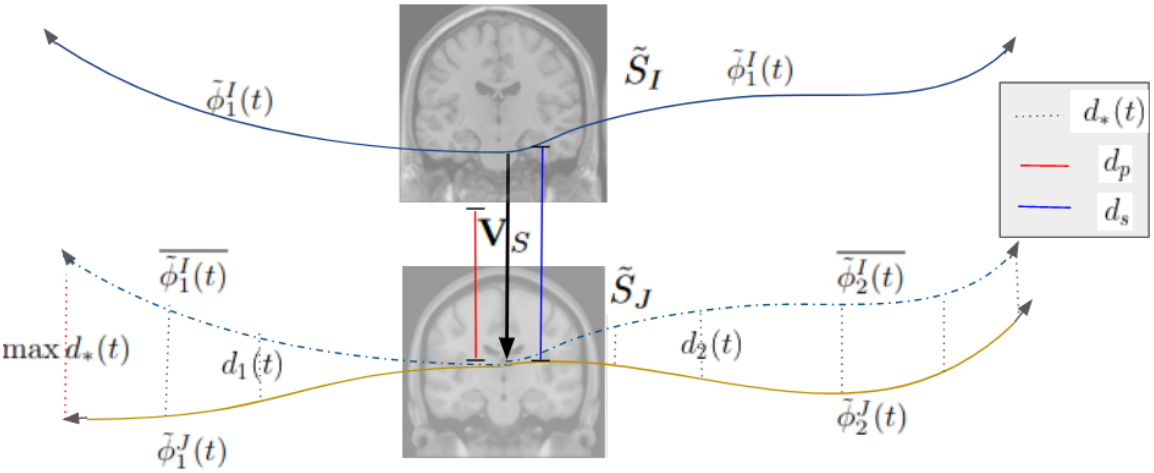

Figure 5.2: *Shape*(d_s) and *path*(d_p) distance computation

The *path* distance is defined as the maximum distance between the two paths over the chosen interval at each spatial location. When the two TS are modeled with one *shape*, then the only distance between the TS will be the *path* distance (d_p). When the shapes differ, then the distance between the paths has to be computed after accounting for the *shape* distance between the two TS. We therefore force $d_s = 0$ by mapping the paths to either $\tilde{S}_I$ or $\tilde{S}_J$ via parallel transport. Specifically, if we consider $\tilde{S}_J$ as the reference to define the *shape* and *path* distance, the paths $\tilde{\phi}_1^I(t)$ and $\tilde{\phi}_2^I(t)$ are transferred to $\tilde{S}_J$ via parallel transport [164] through $\mathbf{V}_S$ to get $\overline{\tilde{\phi}_1^I(t)}$ and $\overline{\tilde{\phi}_2^I(t)}$. The $J(t)$ paths $\tilde{\phi}_1^J(t)$ and $\tilde{\phi}_2^J(t)$ and the transferred paths are defined on $\tilde{S}_J$. A schematic for computing the *path* distance as described is shown in Figure 5.2.

Let the distance between the transferred paths of a TS and the paths of another TS (see Fig.5.2) be denoted as $\{d_1(t), d_2(t)\}$ where $d_1(t)$ corresponds to the distance in $[t_a, m]$ and $d_2(t)$ corresponds to the distance defined in $(m, t_b]$. Since the path is modeled with vector fields $v \cdot \gamma(t)$, the norm of the difference between the vector fields in $I(t)$ and $J(t)$ models can be used to compute the *path* distance $d_*(t)$ as follows.

$$d_*(t) = \left\| v_*^I \cdot \gamma_I(t) - v_*^J \cdot \gamma_J(t) \right\| \tag{5.11}$$

The net difference between the paths has to be finally quantified. We follow the FD formulation for this purpose. Outliers are known to occur in FD. In the current case, since $d_*(t)$ is a continuous smooth function in time the chance of outlier-caused errors is minimal. The maximum distance $\max d_*(t)$ in $t = [t_a, t_b]$ at each spatial position is computed first. The distance, $\max d_*(t)$ is not defined on $\tilde{S}_J$, hence it is transported to $\tilde{S}_J$ via $\overline{\tilde{\phi}_*^I(t)}$ to get $\overline{\max\{d_*(t)\}_{t_a}^{t_b}}$. In Figure 5.2 d_p

corresponds to *path* distance, and it is defined as

$$d_p = \overline{\max\left\{d_*(t)\right\}_{t_a}^{t_b}} \tag{5.12}$$

Finally, the total distance D between the two TS (D) is defined as the sum total of *shape* (d_s and *path* (d_p variation.

$$D = d_s + d_p = \|\mathbf{V}_S\| + \left\|\overline{\max\left\{d_*(t)\right\}_{t_a}^{t_b}}\right\| \tag{5.13}$$

Both *shape* and *path* distances satisfy the distance properties; hence, D also defines a distance that satisfies all distance properties. As $d_*(t)$ is spatially and temporally smooth the $\max$ operation will not add outlier issues in the final distance.

5.3 Results

A variety of experiments were done to validate the proposed method. We believe the proposed method is the first attempt towards separating the *shape* and *path* distance between two TS. Hence, bench-marking was not possible.

5.3.1 Implementation Details

If the TS under consideration is longitudinal data, then *shape* S can correspond to any point in the TS, as the same subject is scanned at different time points. If the TS ithe s population average image (i.,e. a template) at each time point, then S is found by averaging all samples in the TS. Now S represents the anatomy that normalizes all inter-subject and temporal variation. In both cases, an S is not preferred to lie at the end of the time range. This constraint in modeling helps to perform time range matching of the two TS. It also demands a two-piece path modeling which is helpful in handling a complex path as a diffeomorphic deformation.

5.3.2 Simulated data-based experiment

In order to understand how well the proposed method separates and quantifies time-dependent and independent distances, a simulation experiment was done with three sample TS pairs which were constructed by deforming a Shepp-Logan phantom with simulated path and shape deformation as shown in the first column of Figure 5.3. The first set of TS (rows 1-2) was constructed such that they differed only by shape, while the second set of TS (rows 3-4) was constructed to differ only by the path, and finally, the last set of TS (rows 5-6) was constructed to differ in terms of both shape and path. To generate the second set (rows 3-4), two mutually inverse paths were constructed using the path deformation on the phantom image. The third set (rows 5-6) was constructed with different source images; one was the original phantom image, and the other was the shape-deformed phantom image. Inverse paths were applied to these images to construct the TS pair. The last column in Figure 5.3 displays a heat map for each set of the computed shape(d_s) and path(d_p) distance values. For

the first set, the *path* variation is negligible, and *shape* variation is maximum and vice versa for the second set. For the last pair of TS, both *shape* and *path* variations are observed. This observation is in line with the expected results. Hence, this experiment validates the proposed method's ability to separate the time-dependent and independent distances between a pair of TS.

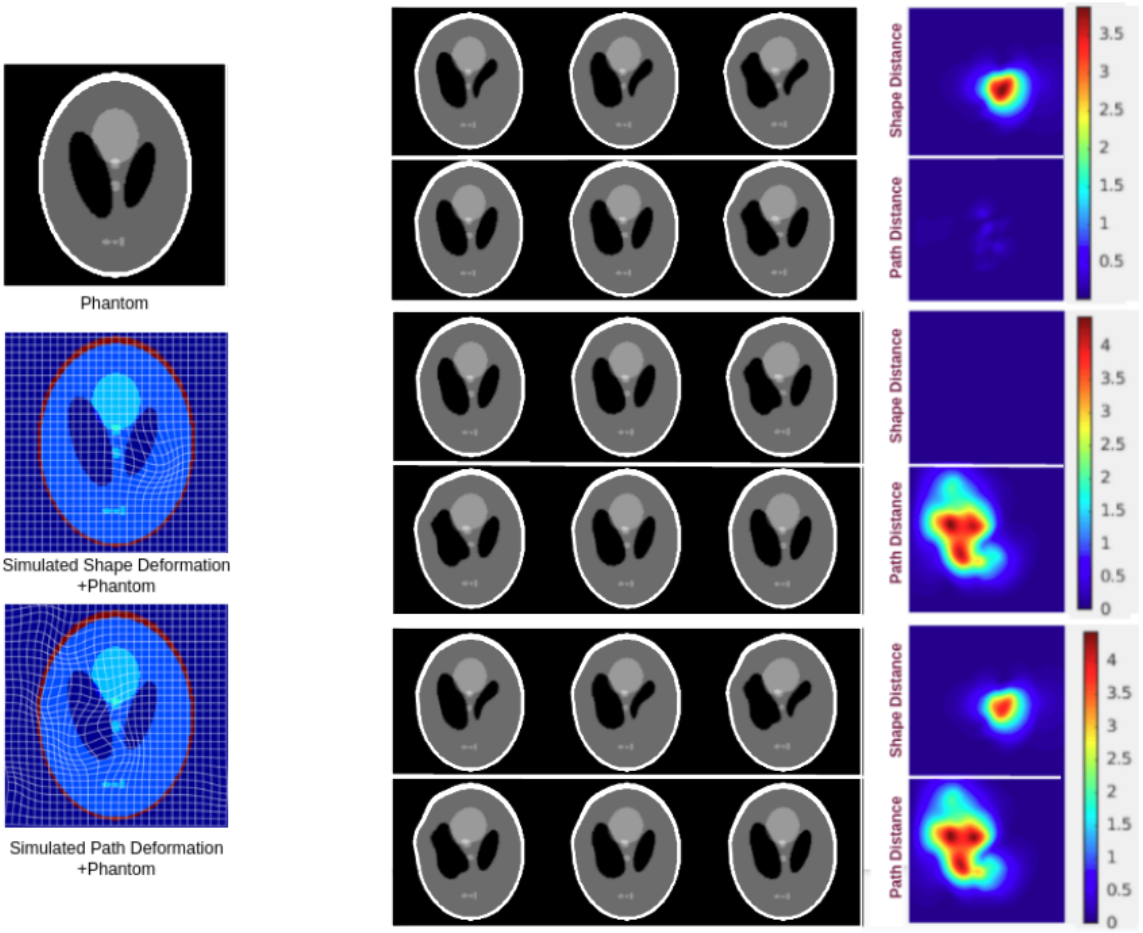

Figure 5.3: Shepp Logan-based validation of the proposed method to quantify the path distance. Column 1: phantom and the deformations fields for shape and path Column 2: three sets of TS used in the validation; column 4: *Shape* and *path* distance maps

5.3.3 Aging data-based experiment

The second experiment is with real data. The intended application domain of the proposed method is biological processes and their comparison, specifically the structural variations over time. This comparison can involve solely healthy individuals drawn from different cohorts or a cohort with both healthy individuals and those with a disease condition. We selected three case studies where the proposed method has potential application: healthy fetal growth, adult aging across populations, and Alzheimer's progression.

Case1: Fetal growth comparison - In this experiment, the focus is on the structural variations associated with fetal growth. Fetal templates of Caucasian (CRL database [81]) and Chinese (FBA database [135]) populations were considered for this purpose. Scans of subjects aged 23-35 weeks were used for both populations. As both the TS were well sampled, the intra-population TS were generated in the same manner as in the previous experiment. A few sample points of the two TS are shown in (Figure 5.4 A - row 1). $P1_a$ and $P1_b$ constructed from Causian($P1$), and $P2_a$ vs $P2_b$ constructed from Chinese($P2$). Two intra-population cases ($P1_a$ vs $P1_b$, and $P2_a$ vs $P2_b$) and one inter-population ($P1$ vs $P2$) case were compared.
If we examine the shape distance maps (Figure 5.4 B), we observe that the inter and intra shape distances are less significant compared to corresponding path distances. Specifically, while there are high values/ bright spots in the path distance maps for the inter-population case, there are no significant bright spots for the intra-population case. This implies that the major cause of difference across the TS is the temporal changes. In (Figure 5.4 C), average $d_*(t)$ values were computed and plotted over time to compare these variations in fetal development between inter- and intra-population TS pairs. In both scenarios, we analyze the growth patterns over time, with path distance solely representing the temporal differences associated with the two-time series. From (Figure 5.4 C) we observe that in both cases, the path distance is a monotonically growing function. The variation in growth patterns within the Chinese and Caucasian populations (the red and blue curves) are seen to be similar. However, the path distance between Chinese and Caucasian fetuses can be seen (in the pink curve) to be larger as the fetus grows.
Observations from all the plots confirm that inter-population differences are more pronounced, primarily due to growth disparities, and these differences consistently increase over time.

Case 2: Adult aging comparison - This experiment focuses on aging trends across adult populations. The aging process and brain anatomy are expected to vary across two different populations [76]. Hence, it is generally expected that inter-population distances will be greater than intra-population distances. However, it should be noted that in a cross-sectional experiment with a small sample size, it is not realistic to expect an intra-population distance of zero. Datasets drawn from the Caucasian (Neurodev [78]) and Japanese (AOBA [94] populations were used for the inter-population study in this experiment. The age range of subjects was 22-87 years for the former and 25-75 years for the latter. An intra-population TS pair was also constructed from the Neurodev data by sampling the data at odd ($P1_a$) and even ($P1_b$) time indices. This was possible because Neurodev templates are densely sample at 5 year-intervals, whereas AOBA templates are only available for every decade. Hence, intra-population analysis was not done with AOBA. The time interval considered for analysis was 30-70 years, as the time ranges differ for the two TS. Sample time points of each TS considered in this analysis are shown in (Figure 5.5 A). The 3D visualization of *shape* and *path* distances are shown in (Figure 5.5 A) in three canonical planes(middle slice of the volume) for a better understanding of the spatial distribution of the distance. It can be observed that both the shape and path distances are smaller (i.e., in the blue range) within a population relative to across populations; this inter-population difference appears to be primarily due to the *path* difference rather

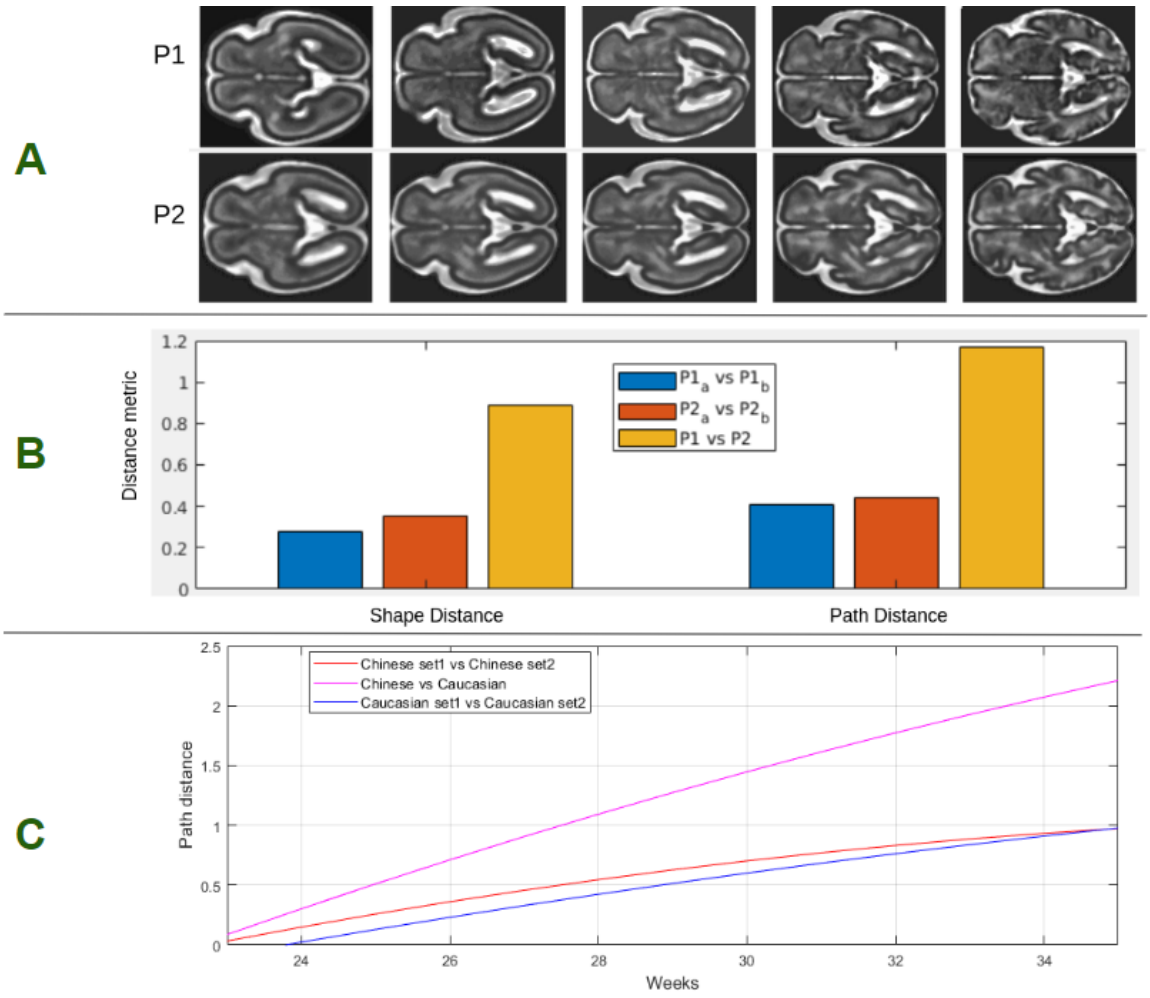

Figure 5.4: Fetal growth study results. A) Samples of population average templates for the Caucasian and Chinese populations are shown in rows 1-2 and the average distance plots for the intra- (P1a, P1b) and inter-populations (P1 vs. P2) are in row 3; B) Validation results. The temporal plots for white matter (WM)/Brain volume ratio are shown for each quadrant. The double-sided arrow represents the distance across the curves; C) Temporal variation in path distance for inter- and intra-population.

than the *shape* difference. In addition to this comparison, we have computed the geodesic regressed paths [179] and plotted the Mean Squared Error (MSE) between the regressed images at each time point for both inter-population and intra-population regression paths in (Figure 5.5 B). It is evident that the inter-population difference ($P1$ vs. $P2$)) is higher relative to intrapopulation ($P1_a$ vs. $P1_b$); this observation is consistent with the patterns seen in the heatmaps derived with the proposed method. However, the MSE plots in (Figure 5.5 B) do not provide detailed insights. In contrast, the distance maps shown in (Figure 5.5 A) are richer as one can discern both the fundamental shape variances between the two populations and the aging-related disparities. Moreover, by pinpointing specific spatial locations, we can identify which regions of the brain are particularly differently aging across populations.

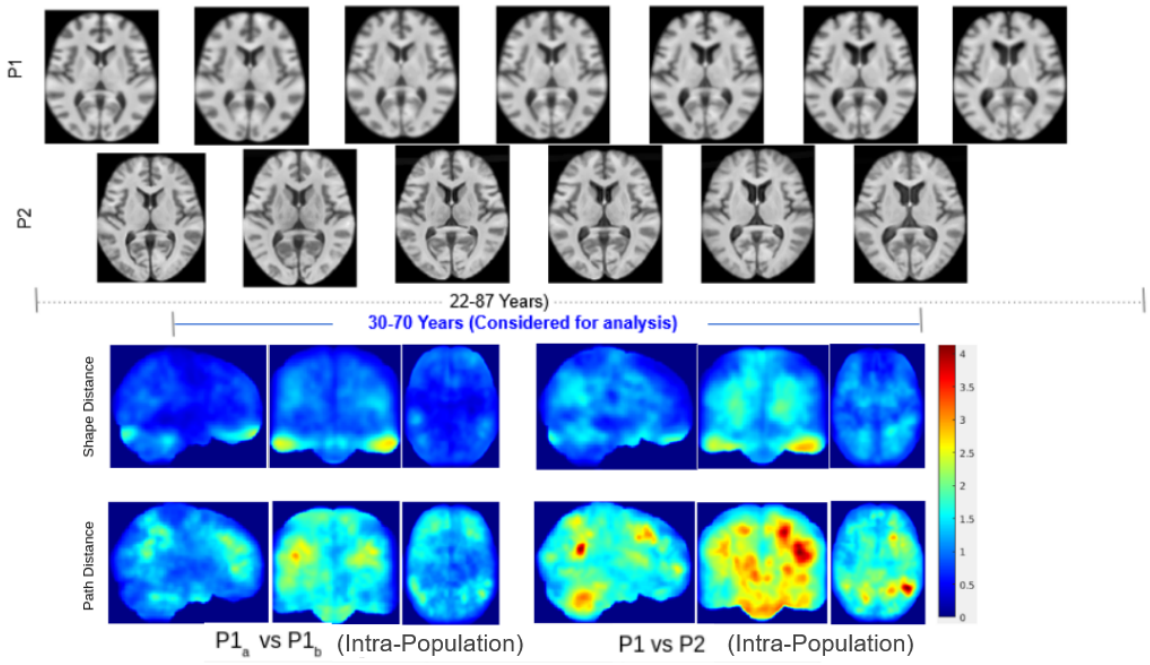

Figure 5.5: Validation results on TS of templates of adults from two different populations. Sample time points of TS considered for the experiment are shown in 1-2 rows. Row 3-4 shows the 3D visualization of the distance between two TS for intra-population ($P1_a$ vs. $P1_b$) and inter-population ($P1$ vs. $P2$).

Case 3: Alzheimer's Disease Progression vs. Normal Aging - Our proposed strategy proves useful when progression of Alzheimer's disease (AD) in an affected individual is to be assessed with reference to a normal individual over a specific period. Two causes of structural difference emerge: first, the inter-subject variation discussed earlier, and second, the disparity in aging-related structural changes due to AD vis a vis normal aging. We consider two normal subjects (subjects 1 and 2) and one AD case (subject 3) over a six year-span from [85] at fairly short intervals of 78-83 years and 78-82 years from the same population. Sample slice images are shown in (Figure 5.6 A) for the 3 subjects. The dataset from where these scans were drawn provides ground truth for AD progression and normal cases based on information of amyloid-beta deposition and tau pathology alongside image-based neurodegeneration. The rate of enlargement of the fluid filled region and atrophy of hippocampus tend to be accelerated in AD compared to the normal aging process. This rapid progression is a key characteristic of the neurodegenerative nature of the disease. Hence, segmentation and volume quantification of fluid-filled regions (CSF) and the hippocampus can help differentiate AD progression from normal brain aging. We utilized FSL software, for the segmentation of both CSF and hippocampus in both hemispheres. The volumes are plotted against age in (Figure 5.6 B).

It is challenging to distinguish the AD case (blue line) from the normal cases (red and pink lines) based on these plots as the hippocampal volume plot for the Normal 2 case is closer to the AD case while the CSF volume is much higher than both AD and Normal 1 case. The higher volume of CSF

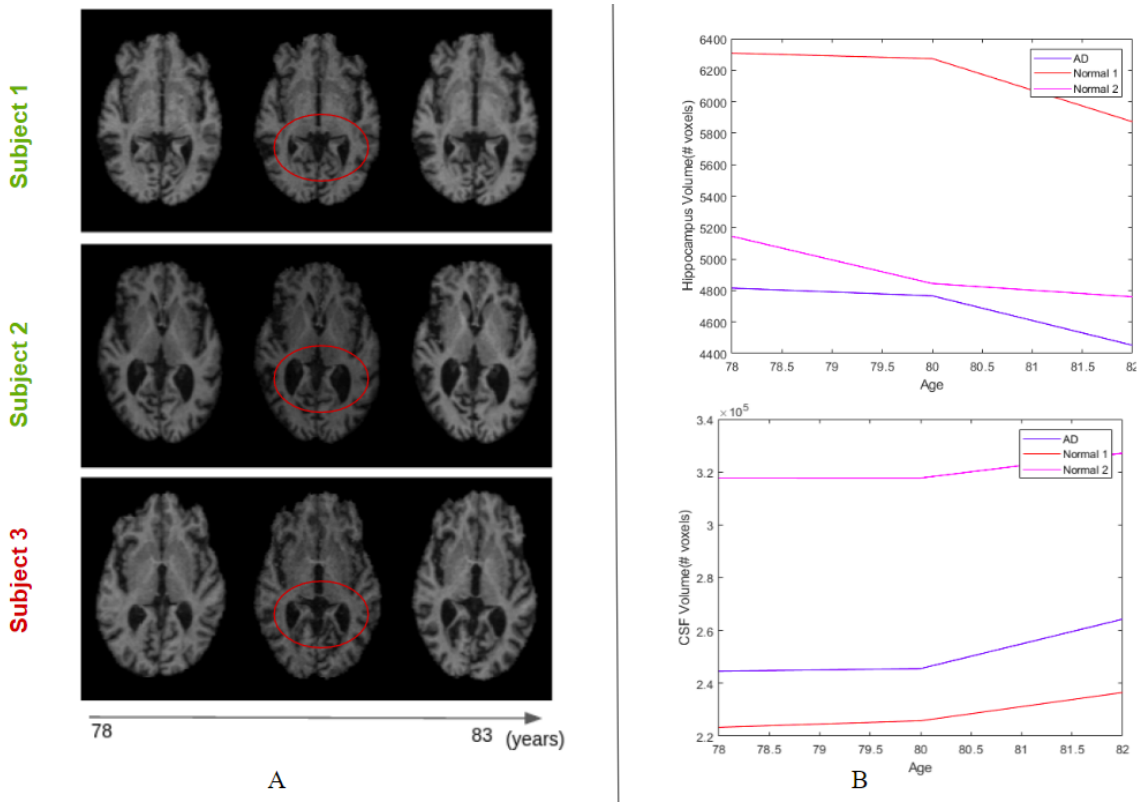

Figure 5.6: Case study of aging in healthy and AD subjects. A) The middle axial slices from a 3D scan are shown for the three subjects who underwent follow-ups during the same timeframe. Subjects 1 and 2 are healthy, while subject 3 has AD. Subject 2 has larger ventricles (dark region within the red ellipse) than the other two subjects. B) Hippocampus (top) and CSF (bottom) volume Plots for all three subjects

for Normal 2 case, relative to the other cases, is consistent with its enlarged appearance (enclosed by red ellipse) in (Figure 5.6 A). Segmentation accuracy affects the volume-based interpretation. Hence, the problem lies not with the inadequacy of volume measures to identify disease condition, but rather with their lack of precise capture which is another challenging problem in neuroimage analysis.

Now, let us see how the proposed method helps to identify AD progression. (Figure 5.7 A) reproduces the MRI slices shown in (Figure 5.6 A) for convenience in explaining this experiment. (Figure 5.6 C) shows the path distance plots for normal vs normal as well as normal vs AD cases from 78 to 83 years. The path distance curve for normal vs AD cases grows rapidly after 80 years due to aging and the effects of AD-related atrophy. The path distance curve for normal vs normal is lower after 80 years and shows a marginal and smooth upward trend, as the common cause of temporal variation now is healthy aging.

Next, we turn to the spatial distance maps to illustrate the insights they provide. The time-independent, inter-subject structural variability is not directly linked to disease or normal conditions. Nevertheless, the inter-subject shape distance variations highlight the proposed method's usefulness in spa-

tially locating inter-subject anatomy differences. Specifically, one can observe from the MRIs of subject 1 and subject 2, the dark structures indicated by the red arrows (Figure 5.7 A - row 1,2), exhibit a consistent structural difference at all time points, i.e. it is a time-independent difference. Our proposed SD captures this as a bright spot in the corresponding location on the heatmap shown in (Figure 5.7 B - left, top row). Similarly, if we consider the folded regions pointed by pink arrows in the MRIs of subject 1 and subject 3 (Figure 5.7 - A row 1,3), there is a structural dissimilarity that is consistent over time. This is also captured as a bright spot in the corresponding location on the heatmap (Figure 5.7 B - right, top row). These are two sample positions, and this observation holds for other regions as well, i.e., any existence of structural difference /similarity in a region, which is consistent over time, will be reflected in the shape distance maps as bright/dark spots in the same location. In general, inter-subject anatomical variation is inherently random due to unique developmental factors. As SD heatmaps reveal the spatial variation in the SD values, more intensive variations are observed in cortical regions (outer boundary).

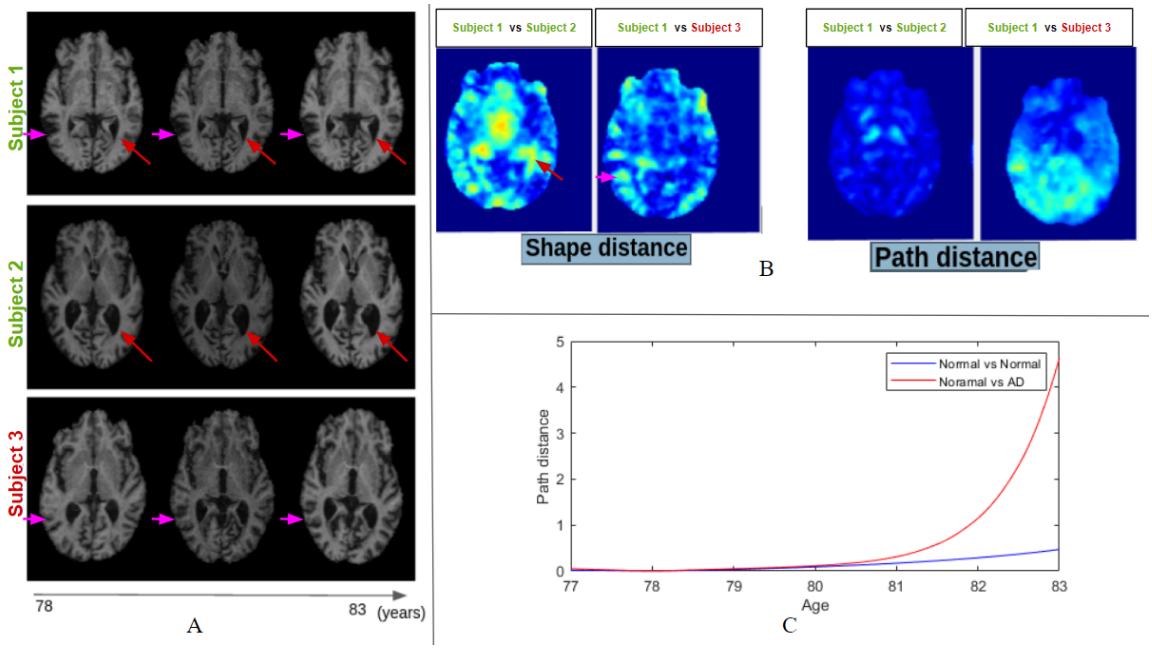

Figure 5.7: Distance map-based analysis of healthy and AD subjects. A) Middle axial slices from a 3D scan for three subjects repeated from (Figure 5.6 A) ; B) Shape and path distance plots. Here arrows pinpoint to regions with consistent variation across time within the time series and corresponding shape distance maps; C) Path distance plot illustrating the variation in path between two normal aging subjects and between a normal aging subject and an individual with AD.

5.4 Discussion and Conclusion

A metric that enables disentangling of the *shape* and *path* variation and helps quantify the difference between a pair of TS is proposed in this work. The proposed metric is an affine invariant and time interval mismatch-compensated metric. The idea of *shape* variation in the proposed metric is

more relevant when the TS under consideration are from cohorts from different populations. As the course of the path is considered in the quantification of the *path* variation, the intra-population TS path variation can be analyzed. For example, one can study the *path* difference in the growth pattern among the elderly (50-80 years) versus the young (20-50) within a population. This was done in our second experiment, and the distance for Caucasians was found to be 1.8, while it is 1.4 for Japanese. This suggests that the temporal variations are faster in Caucasians than in Japanese after adulthood. Whereas the difference across populations is much lower for the fetal brain. Such analysis opens up the opportunity to better understand the reason behind such trends from young to elderly and across populations. The main goal of longitudinal data-based group analysis is to understand the general trend. Our work enables approaching the problem via a joint statistical analysis of 4D data (TS of 3D images). A metric to quantify the distance between a pair of TS can also help derive an average TS model from a set of TS as done for 1D-3D objects. There are some limitations with regard to the proposed metric. It cannot handle large temporal mismatches. Further, the metric accuracy is totally dependent on the accuracy of the computed deformations. This is relevant to inter-subject TS analysis registration in this scenario is generally error-prone that too for a complex structure such as the brain.

Chapter *6*

Indian Brain Aging Data Acquisition and Inter-Population Aging Comparison

Understanding distinct neurological aging patterns across various populations is vital in the context of a globally aging populace. This study aims to explore structural variations in the aging brain across diverse ethnic backgrounds. We introduce an elaborate framework for analyzing such structural variations across aging in different populations, evaluating it with a sample dataset from Indian, Chinese, Japanese, and Caucasian groups. The analysis involves a two-pronged approach applied to MRI data.

Initially, a group analysis was performed involving tissue segmentation through FSL-FAST, examining gray matter (GM), white matter (WM), and cerebrospinal fluid (CSF). Subsequently, a continuous model-based analysis was employed, defining aging as a diffeomorphic transformation, which facilitated a detailed intra- and inter-population analysis, and examined both global anatomy and age-dependent distances of each population in comparison to the Indian population. This analysis framework enables us to derive information about various aspects of aging related structural changes both qualitatively and quantitatively. For example, the analysis revealed distinct aging trajectories in the different populations with relative changes in onset of GM reductions and ventricular expansion. Additionally, we observed a significant hemispherical asymmetry in the expansion rate in the left brain's CSF-filled region across all populations. Detailed insights into the spatial distribution of brain deformations over time were obtained, with particular focus on anatomical changes relative to a reference time point.

6.1 Introduction

Brain aging encompasses a wide array of changes in brain morphology and cognitive abilities. Understanding the standard patterns of aging is essential for identifying normal and abnormal trends. Although these changes vary among individuals, studying them within a cohort can reveal general aging trends influenced by factors such as gender, educational background, and multilingualism [171–173]. The focus of this study is specifically on comparing the structural changes in healthy brain aging across different populations while excluding cognitive changes.

Promoting healthy aging involves recognizing standardized expectations and detecting deviations

from them. For instance, research has shown that aerobic exercise [174] positively impacts brain aging, while engaging in activities like multilingualism and music [175] may also contribute to healthy aging. To create effective strategies for healthy aging, it is vital to grasp the trends and deviations in aging, particularly among diverse populations. Understanding why certain populations exhibit better aging outcomes will enable the implementation of methods that promote better overall aging outcomes for everyone.

Significant progress has been made in establishing global standards for brain aging by analyzing brain scans from diverse regions [176]. Researchers have extensively explored population-specific structural changes during aging, using various methods such as age-specific templates [177, 178] and spatiotemporal models [179, 181]. Constructing anatomical models for different age groups is common. However, it's important to mention that these template-based techniques, while improving our understanding of long-term anatomical changes, may not fully grasp the complex temporal dynamics of aging. On the other hand, spatiotemporal models capture the anatomy changes with time, from either cross-sectional or longitudinal data. Captured information include changes in gross structure, iron deposition and demyelination with aging [183]. Understanding of such changes in normal aging enable the development of consistent analysis pipelines for assessing individual brain aging to identify any abnormal aging patterns. The scope of these studies has been limited to a single population.

Global data-driven studies center their attention on universal patterns, as demonstrated by the comprehensive research conducted by [176].This study rigorously examines the aging process, making use of advanced statistical analysis modeling to explore changes in tissue volume and cortical thickness with age, drawing from the most extensive and inclusive dataset available. Understanding the complexities of the brain aging requires consideration of various factors such as gender, ethnicity, and education, as well as challenges in data acquisition. Focusing on subjects with shared ethnic or geographical backgrounds can provide insights in tackling these complexities. By studying populations with common genetic, cultural, and environmental influences, a more targeted analysis can be conducted compared to global data-based studies [176], and the aim of this work is to compare these common trends. Nonetheless, it's essential to recognize that even within these populations, variations in aging trends and patterns may exist. In this study, we investigate brain aging in four distinct populations: Indian, Chinese, Korean, and Caucasian. These populations were chosen based on their diverse ethnic backgrounds and geographical locations, as these factors are expected to contribute to variations in the aging process. By examining the brain aging of these specific populations, we aim to gain valuable insights into the unique trends and characteristics of aging within and across the groups.

Numerous studies have sought to explore and distinguish aging patterns among diverse populations. Typically, researchers analyze aging patterns by visually comparing time series data or using derived measures, such as changes in cerebral volume and brain dimensions [184, 194, 195]. A widely employed technique for comparing population trends in brain structure is Voxel-based morphometry (VBM) [191, 192, 196]. VBM entails mapping brain images from different individuals to a common template space and subsequently comparing the derived cortical features across these mapped

brains. However, VBM analysis does have limitations when it comes to direct population comparisons for age-related brain structure changes since it primarily focuses on detecting differences in brain structure between predefined groups, such as young versus old or patient versus control. Consequently, its main emphasis is on identifying group disparities, rather than providing a detailed understanding of age-related changes that may occur in a continuous and subtle manner across diverse populations. As such, while VBM can be valuable for exploring structural differences within specific groups, it may not be fully tailored for comprehensive investigations of brain aging across different populations.

In order to comprehensively understand and compare brain aging, a framework that combines both qualitative and quantitative analysis methods is proposed in this work. This framework can be used to study aging within and across populations. Brain aging is not solely governed by time, as various factors such as genetics, environment, and lifestyle play significant roles in influencing the aging process. In light of this complexity, our analysis aims to distinguish aging-dependent variations from the impacts of other aging-independent factors. We do this to achieve a more meaningful comparison of brain aging across different populations. In summary, our contributions include qualitative and quantitative analysis of brain aging within and across populations, distinguishing aging-dependent changes as individuals age, and age-independent differences in brain aging patterns among different groups.

6.2 Brain Aging Data Development

Our study considered four distinct populations (Indian, Caucasian, Chinese, and Japanese) to gain insights into the trends in changes in brain anatomy with age. T1 MRI scans (data) of the brain were sourced from healthy adults aged 20 to 80 years, in each population as summarized in Table 1. The data for the Indian population were partly collected explicitly for this study and partly retrieved from previous studies. The data from previous studies [155]were selected to approximate the acquired data closely. The data for other populations were sourced from publicly available repositories. Ideally, we need to have equal number of subjects, both male and female, at each time point (decade in our case) in the study to avoid any bias. The number of subjects considered for each time point was constrained by the fact that the public repositories had fewer elderly than young/middle-aged subjects. Hence, we chose 26 subjects (split equally between males and females) for each time point. To maintain consistency, a similar distribution of age and gender was maintained across all populations in each decade as seen in Table 1. A detailed description of the data collected for each population is presented next.

Population	Magnetic field strength of scanners	#Subjects distribution in every decade (20-80 years)	Gender Distribution M:F	Matrix	Size (mm)
Indian	3T Philips	1:1:0.9:1:1:1	1:0.99	256x256x165	0.7×0.7×0.5
Caussian	3T Siemens l0.	1:1:1:1:1	1:1	256x240x192	1x1x1
Chinese	3T Siemens	1:1:1:1:1:0.88	0.99:1	256 x256x176	1x1x1
Japanese	0.5 T GE	1:1:1:1:1:1	1:1	256×256×124	1×1×1.5

Table 6.1: Comparison of Population Characteristics and MRI Scanner Specifications for Different Ethnic Groups

6.3 Indian population database creation

3T scans of healthy subjects were collected from multiple sites (see the table in Figure 6.1A for details) within India [155] and individual sites had ethical approval for collecting and sharing the data for research purposes. In the 20-80 age range, 26 scans were collected for each decade, with the exception of a single decade which had 24 scans. This dataset will be referred to as the IBASD. The gender and age distribution of the collected data is shown in Figure 6.1 B. Only physically and psychologically normal subjects with no history of head injury or other neurological disorders were included in the study. The subject selection procedure is shown in Figure 6.2. Pregnant women,

A

Institute	MRI scanner	Image size	Matrix
IIIT	Philips, 3T	320x320x384	0.718 x 0.718 x 0.5
SCTMT	GE, 3T	256x256x172	1 x 1 x 1
NIMHANS	Philips, 3T	256x256x165	1 x 1 x 1
AIG	Philips, 3T	420X515X190	0.533 x 0.532 x 0.85

B

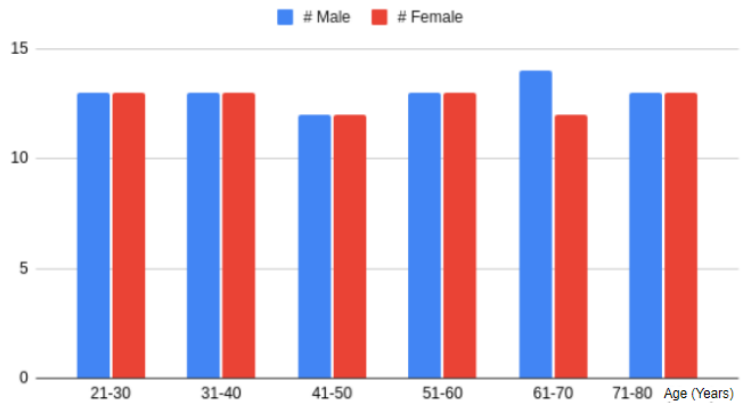

Figure 6.1: A) Acquisition details for the collected scans. B) Gender distribution of subjects in the Indian cohort.

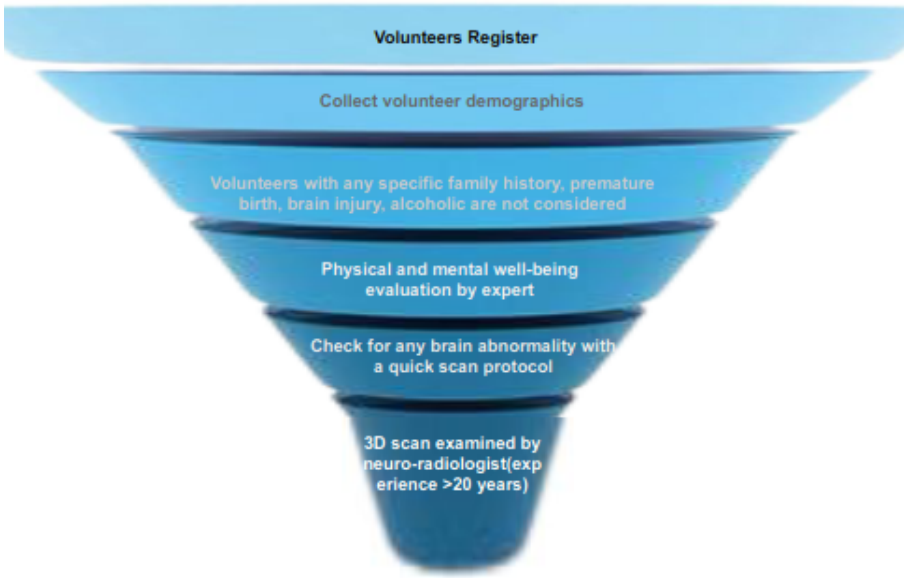

Figure 6.2: Scan selection procedure for the study

subjects born pre-maturely, and those with any long-term disease condition were excluded from the study. All the acquired scans were of right-handed subjects. Experienced medical experts checked all the scans in corresponding institutions for any structural abnormality in the scans.

6.4 Data collection for framework validation

6.4.1 Caucasian population

The Cambridge Centre for Ageing and Neuroscience (Cam-CAN) database [95] has neuroscans of subjects recruited from the Cambridge City area in the United Kingdom. A decadal of 26, 3T MRI scans were selected for each decade from the Cam-CAN database for our study. The demographic information available in the database for each individual was used to select subjects labeled as belonging to the 'white' ethnic group. Subjects meeting these selection criteria were chosen manually.

6.4.2 Chinese population

The Chinese population data was sourced from the Southwest University Adult Lifespan Dataset (SALD) [98] built with scans of University students, staff, and subjects from control group of clinical studies. Out of 494 scans available, 153 scans within the age range of 20-80 years were carefully selected to maintain gender distribution and an equal number of subjects in each decade. A total of 23 images were selected in the 70-80 age range, with rough gender balance, while 26 images were selected in other age ranges.

6.4.3 Japanese population

The Japanese population data was sourced from the AOBA database [94] which includes scans of volunteers recruited by the AOBA Brain Imaging Research Center in Japan. Out of a total of 1153 scans available in the database, 156 scans were chosen for our study which resulted in 26 scans for each decade. Although the scans were sourced from a 0.5T scanner, they were of good quality and comparable to other databases, possibly due to longer scanning times.

6.5 Framework for Comparative Brain Aging Analysis Across Populations

A time series of templates representing each decade forms the basis of our aging study. Given that the scans we selected were collected from multiple sites with different scanners and protocols, the scans have to be standardised and normalised.

6.5.1 Data Normalization and Standardization

We employed two analysis strategies to compare the aging of different populations: group analysis and model-based analysis. The data preparation process to support these two analysis strategies was different. The specific processes are explained here.

6.5.1.1 Preprocessing for Group analysis

Individual images within all population-specific datasets (CAMCAN, SALD, AOBA, and IBASD) were preprocessed using the complete FSL pipeline, including the "fsl_anat" command. This comprehensive pipeline involves various steps such as brain extraction, bias field correction, tissue segmentation, and nonlinear registration. This preprocessing pipeline ensures consistent and reliable quality in tissue segmentation, which is critical for group-level analysis and comparisons.

6.5.1.2 Data Preparation for Aging Model Based analysis

The main goal of model-based analysis is to develop a consistent and generalizable model that can be applied across datasets, rather than performing analysis on derived measurements from individual images.

Creating Decade-Specific Templates - For each population, individual images of subjects, in the age range of 20 to 80 years, were skull-stripped and grouped into six distinct decades, for each population. Using the group registration tool from the ANTS package, templates were generated for each decade. The primary stopping criterion was based on a fixed number of iterations, with additional consideration given to the mean displacement observed within the initial iterations. The image dimension, intensity range, and alignment were maintained relative to the individual population space, as illustrated in Figure 6.3-A. However, it is important to note that the templates needed to be aligned to a common reference space before proceeding to the subsequent steps, which will

be discussed in detail later on.

Creating Reference Template - A reference template was crafted to align all templates to a common space, closely resembling the natural appearance of an original scan. This template was constructed from a carefully chosen subset of 70 images from the Indian population-specific IBASD dataset, all acquired using the same scanner and parameters. The brain region was cropped, and standard zero-padding was applied to each image. Finally, the group registration tool from the ANTS package was used to align and combine the preprocessed images, creating the reference template.

Template Prepossessing - The reference template image played a crucial role in normalizing each individual template across all four datasets. After applying cropping and standard zero-padding, affine alignment and histogram matching were conducted relative to the template using MATLAB, ensuring both affine and data acquisition invariance. To further ensure image quality and identify potential distortions, manual checks were performed during the preprocessing steps. Once verified, a time series of templates was generated for each population, consisting of six time points spanning ages from 20 to 80 years. This comprehensive approach allowed for robust and accurate analysis across different age groups in the study.

Creating Decade-Specific Templates - Finally, for standardization, the IBASD dataset was chosen as the reference population and a global template, combining all decade-specific templates, was created. Each individual template from the remaining three populations was affinely aligned and histogram equalized with respect to this global template. Visual checks were performed in 3D to ensure the quality of each template before proceeding with further analysis. The preprocessing steps made the templates consistent and standardized across populations, shown in Figure 6.3 B. This ensures a reliable and accurate analysis of the aging process.

6.5.2 An Overview of the Analytical Framework

Our aim is to investigate the structural variations in the aging brain in different populations. Both qualitative and quantitative measures are included in the analysis framework in order to understand population-specific aging processes. Figure 6.4 provides a visual representation of the proposed analysis framework. Global measures can be used to infer changes in brain size and tissue volume in different populations whereas non-rigid deformations can help understand the local changes. These local changes encompass both aging-related or time-dependent variations and population-specific, time-independent variations observed across populations.

6.5.3 Group analysis using discrete time points

In group analysis, the primary focus is indeed on examining the individual subject images to understand the group trend in aging for each population. Group analysis was chosen to be done via tissue volume changes across individuals. Tissue segmentation of the individual scans was first performed using FSL-FAST. This is a tool in the FSL software package specifically designed for accurate tissue segmentation. Specifically, the grey matter, white matter, and CSF were segmented and the average volume of each segmented tissue was calculated for each decade by considering ap-

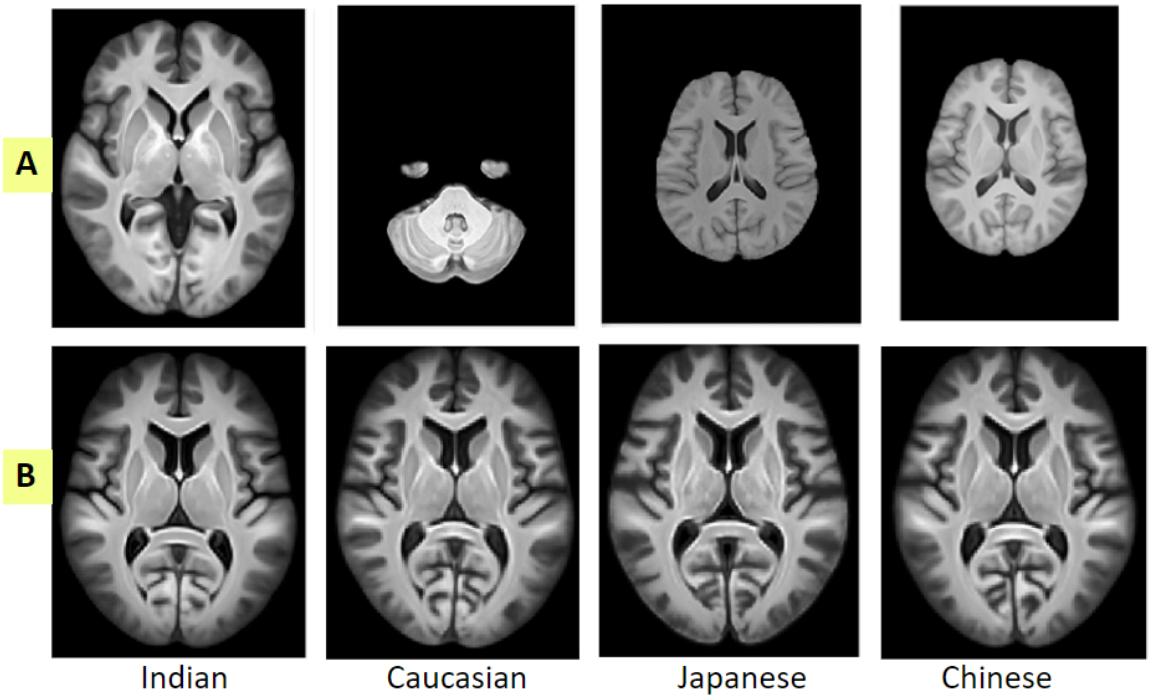

Figure 6.3: Sample templates corresponds to 40-50 years age range before(A) and after (B) template pre-processing

proximately 26 image tissue volumes at every time point. In order to visualise and capture the trend of volumetric changes, a cubic function was fitted to the mean volume points for each tissue type in each population. This trend allows us to quantitatively assess how tissue volumes change with aging and gain insights into the overall patterns and trajectories of tissue degeneration or growth.

6.5.4 Continuous model based analysis

Template-based analysis is a powerful method used to study aging-related changes by bringing individual images to a common space for cross-sectional data analysis. This approach involves aligning and registering the template images to a shared coordinate system. We choose a cross-sectional data-based diffeormorphic aging model ([179]) as it models the aging process as a smooth, monotonic, and diffeomorphic change observed across the discrete templates. The aging process is represented as a continuous deformation of a template in a global space. We next explain how this model is derived.

Aging model:

First, a template, represented as S, is obtained by aligning and then averaging all the templates in the discrete time series of a population. The aging process is then modeled as a deformation (ϕ) of the average anatomy (S) over time. As S represents a temporal average and is positioned towards the center in time, the aging deformation is defined with respect to this reference point. This design necessitates the computation of both forward and backward deformations relative to the reference time point. Given that S is positioned towards the middle, $t = m$, two paths (ϕ_1,ϕ_2) are defined to

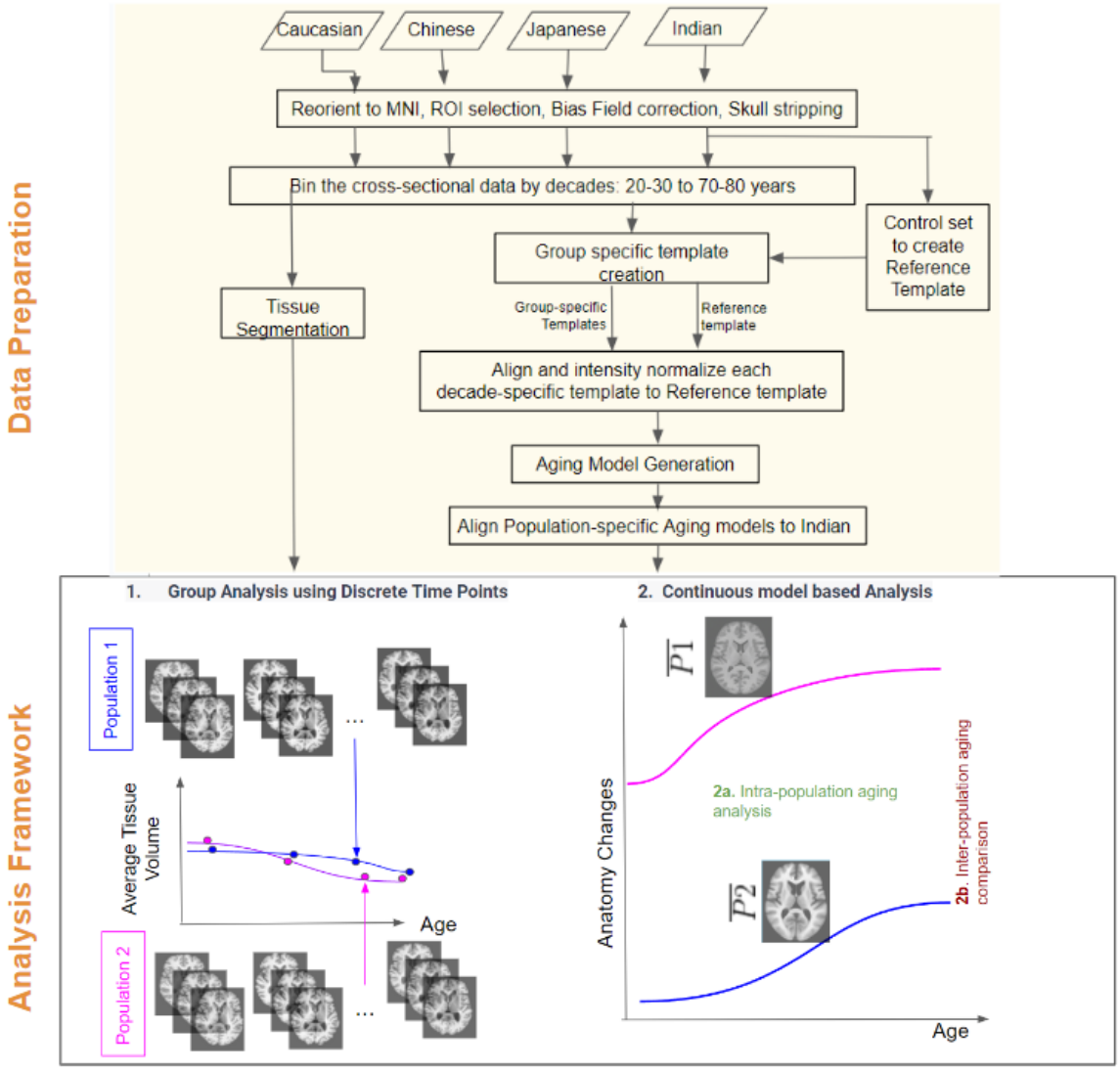

Figure 6.4: Graphical representation of analysis framework

cover the entire time range, namely $[t_0, m]$ and $[m, t_n]$. The forward and backward deformations are determined by composing the pairwise deformations sequentially. These deformations are computed between consecutive templates in the given time series and subsequently mapped into the S space.

The aging model for the population is then found as

$$I(t) = \begin{cases} \phi_1(t) \circ S \text{ for } t \geq m, \\ \phi_2(t) \circ S \text{ for } t \leq m. \end{cases} \tag{6.1}$$

6.5.4.1 Intra-population aging analysis

The aging model given by Equation6.1 is used for this analysis. Visualizing the structural alterations in the brain aids in defining the expected trends of brain aging. Hence, an aging model is derived for each of the four populations (Indian, Chinese, Japanese and Caucasian). The normative deformations computed for each population are individually analyzed to gain insights into the local structural changes in the brain during aging. These deformations can be attributed to tissue contraction or expansion in fluid-filled regions as only topology preserving deformations are expected in a matured aging brain. By analyzing the Jacobians of the normative deformations, it should be possible to draw meaningful conclusions.

6.5.4.2 Inter-population aging analysis

The aging models utilized in this study are derived from different datasets, which introduces the possibility of temporal misalignment between the models. Additionally, the models may also exhibit affine misalignment and have varying intensity ranges. As mentioned earlier, these are addressed via normalisation and standardization processes which precede comparative analysis. A two-level comparison framework is proposed aimed at providing a comprehensive understanding of the variations in aging among different populations. In the first level, a qualitative analysis is performed to explore trend variations by comparing the normative aging in individual populations. The differences in deformation trends for the entire brain and some specific sub-regions are visualised for this purpose.

Furthermore, deformation-based approaches are employed to explore the variations in brain structure and shape changes linked to the aging process across populations. To accomplish this, a metric described in our previous work [180] is employed. In general, any difference in aging trends across different populations can be due to the difference between the average anatomies as well as the difference in deformation happening on the average anatomies. The former is termed global anatomy distance while the latter is termed as age dependant distance. Let us consider two populations a, b with average/global anatomies S_a, andS_b, and deformations ϕ^a and ϕ^b, respectively. A deformation-based distance between the average anatomies (S_a and S_b) quantifies the difference in the global anatomies while the maximum distance between the deformations (ϕ^a and ϕ^b) in time quantifies the age dependant difference. Specifically, the deformation between the S_a and S_b captures the global anatomy variation ψ between the two time series; here, the deformation is modeled as $\psi = \exp(\mathbf{V}_S)$, where $\mathbf{V}_S$ represents a stationary velocity field. Therefore, the norm of the vector field $\mathbf{V}_S$ can be directly used to quantify the deformation [96]. The global anatomy distance (d_s) between S_a and S_b is hence defined as

$$d_s = \|\mathbf{V}_S\| \tag{6.2}$$

The paths ϕ^a and ϕ^b are modeled with vector fields $v_a \cdot \gamma(t)$ and $v_b \cdot \gamma(t)$ respectively. The norm of the difference between the vector fields is used to compute the distance between the paths at each

time point, $d_*(t)$.

$$d_*(t) = \|v_a \cdot \gamma_a(t) - v_b \cdot \gamma_b(t)\| \tag{6.3}$$

The age dependant distance is then defined to be the maximum $d_*(t)$.

$$d_p = \max\{d_*(t)\} \tag{6.4}$$

It is important to note that both d_S and d_P are distances defined at every voxel of S_a or S_b. By combining both qualitative and quantitative analyses, this framework offers a way to understand the variations in aging across populations.

6.6 Results

We illustrate the proposed framework using sample data collected for validation of the framework, highlighting the possibilities of conducting an elaborate analysis to derive various aspects of brain aging comparisons across populations.

6.6.1 Group Analysis using Discrete Time Points

An analysis was conducted to investigate the normative tissue volume changes relative to the total brain volume for different populations. The three major tissues, namely, white matter(WM), gray matter(GM), and cerebrospinal fluid (CSF), were analysed at individual scan level. Segmented volumes were normalised with respect to the total brain volume in order to assess their proportion in the total brain volume. This was averaged over all scans at each time point. These are depicted for different populations in Figure 6.5 with mean and standard deviation volume values at each time point and the trends across curves are valid even after considering the variation.
In the following, all results refer to normalised values. When considering the gray matter (GM) volume, it consistently decreases with age in Indian and Caucasian populations from earlier age points. In Japanese and Chinese groups the trend is different. Specifically, the Japanese population exhibits minimal GM degradation until the age of 60, after which there is a notable acceleration in degradation. In contrast, for the Chinese population, the onset of GM degradation occurs much earlier, starting at around 35 years of age, before which the degradation remains minimal. The WM volume tends to remain fairly stable across all populations except Indian which shows a slight deviation. The plots also indicate ventricular expansion with aging for all populations as CSF volume has an increasing trend over age. However, it's worth noting that the acceleration of this expansion in the Japanese population occurs later, typically after the age of 65, which contrasts with other populations where the onset of ventricular expansion tends to occur earlier.

6.6.2 Continuous model based Analysis

Age-specific models were developed for each population using time series of brain templates. To create these aging models, templates were defined for each decade within the population. The

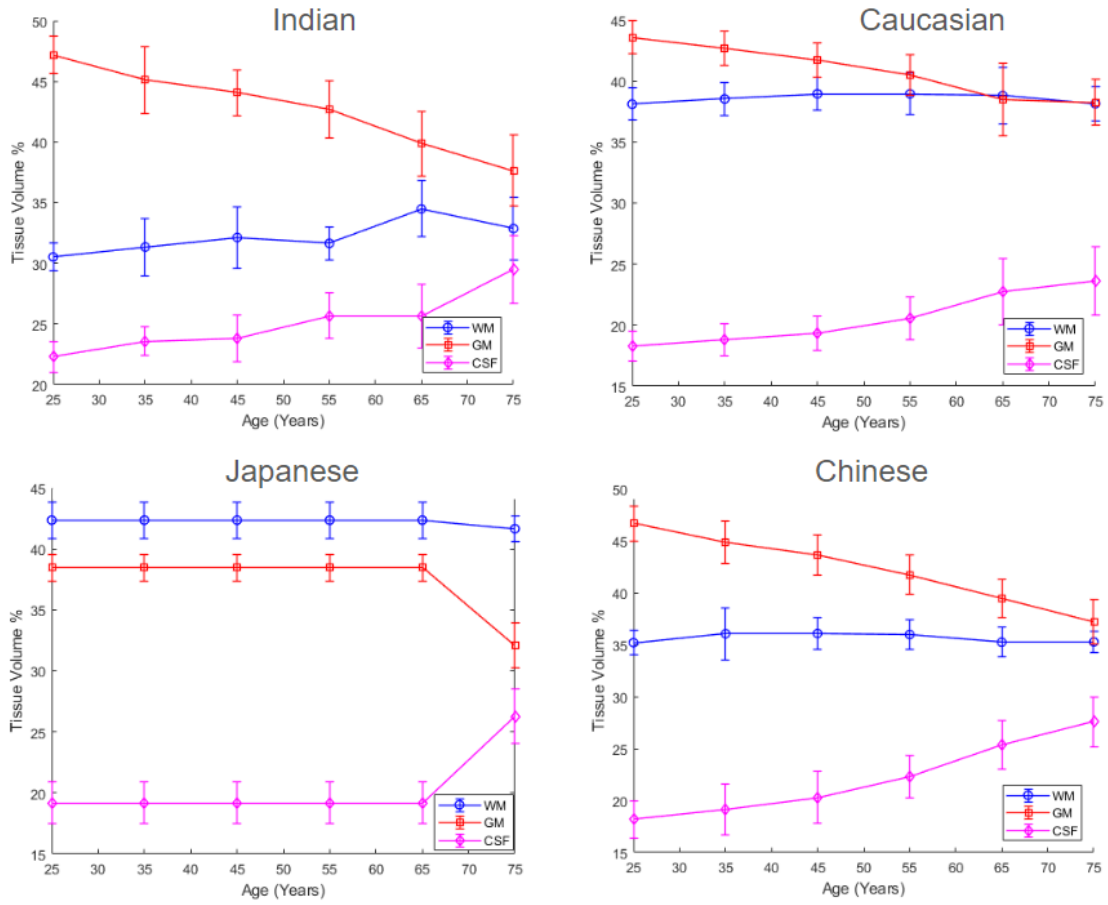

Figure 6.5: Distribution of White matter(WM), gray matter(GM), and cerebrospinal fluid (CSF) regions relative to the total brain volume across aging for different populations.

Indian global template served as a reference to align other population templates using an affine transformation. The central slices of the age-specific templates derived from these aging models are shown in Figure 6.6. As direct visual comparisons between the models is challenging, we performed further analyses to obtain interpretable results.

6.6.2.1 Qualitative Analysis of Inter-Population Aging

We wish to visualise the anatomical changes due to aging across various populations relative to a reference time point. On average, the brain is considered to be fully matured [182] at the age of 20 years and hence this serves as a good reference point.

The deformation between the brain anatomy and the reference brain from the same population was computed at every time point. Jacobians of the computed deformations were utilized to assess the local volume changes in different brain regions as they provide insights into the expansion or contraction occurring in specific brain regions. The resulting Jacobian maps, which illustrate the spatial distribution of these deformations, are visualised as heatmaps in Figure 6.7. The general

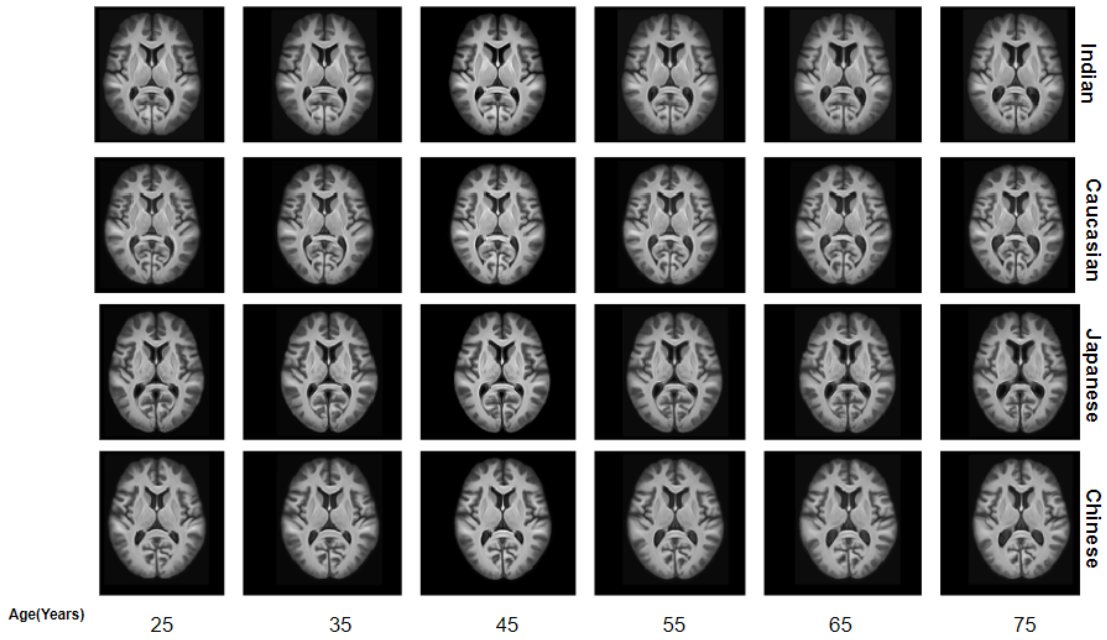

Figure 6.6: Age-specific templates derived from population-specific aging models for ages=25, 35, ...75 years

trend observed is that there is no change at ages closer to 20 years (as indicated by blue pixels) and significant changes at ventricular locations above the age of 55. These maps enable an understanding of how the structural alterations in the brain evolve over time in different populations. The tissue volume analysis plots (Figure 6.5) and the Jacobian maps (Figure 6.7) are correlated. In order to see this more clearly, the rate of expansion or shrinkage in the brain was computed for specific regions using segmentation maps and their contraction/expansion relative to the reference point (20 years of age) were computed. Specifically, an atlas-based registration was used to identify four regions, encompassing ventricles, sub-cortical structures, white matter and cortical grey matter. Next, the Jacobians for these regions were computed and their average value at each time point was plotted as shown in Figure 6.8 A. The ventricles predominantly exhibit increasingly positive Jacobian values over time, indicating an expanding trend, while the other regions show increasingly negative Jacobian values over time indicating shrinkage/contraction trend. There is evidence for early onset of contraction in cortical compared to sub-cortical GM. The sub-cortical gray matter contraction and ventricular expansion occurs at a significantly faster rate with an earlier onset in the Indian population when compared to other populations. Interestingly, white matter degradation is more pronounced in the Japanese population, with other populations exhibiting similar trends. The trends in cortical gray matter degradation become notably more distinct among populations after the age of approximately 55 years. Additionally, the analysis also highlights the delayed onset of ventricular expansion and sub-cortical contraction in the Japanese population.

An additional analysis was conducted to examine potential hemispherical asymmetry in brain aging. Figure 6.8-B) shows the average Jacobian values at the hemispherical level for the CSF-

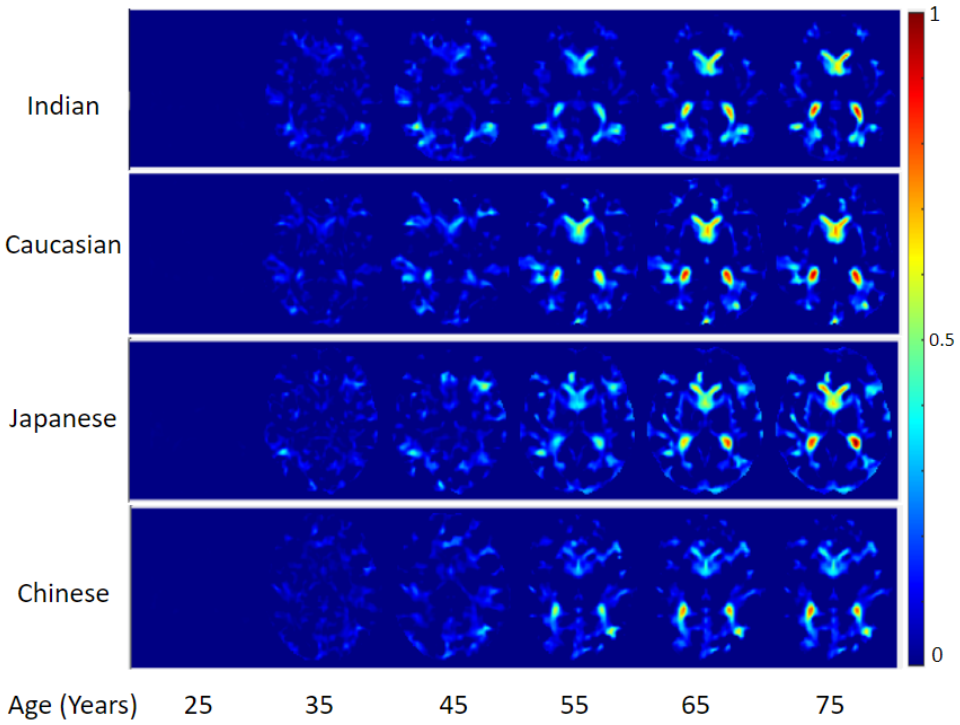

Figure 6.7: The deformation with respect to the initial time point (25years) and subsequent time points in each decade for every population

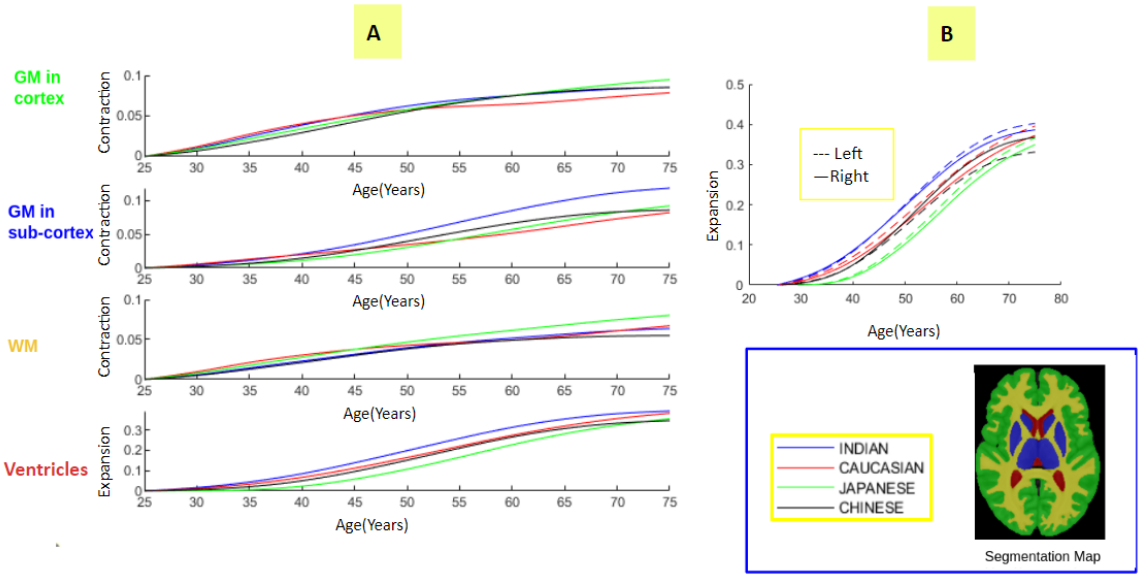

Figure 6.8: The plot of expansion and contraction in four brain regions over time, alongside the segmentation atlas. The regions include ventricles, sub-cortical structures, white matter, and cortical grey matter (shown inside the Blue box).

filled region in each population. The trends in the plots indicate that the expansion of this region

in the left brain is at a much faster rate than in the right hemisphere and is consistently so in all populations.

6.6.2.2 Quantitative analysis of inter-population aging

It should be noted that all the previous analyses used brain tissue segmentations, which can introduce errors, particularly given the complexity of cortical tissue boundaries. In this analysis, structural changes are directly examined without utilizing any segmentation steps. Here, we study the variations in average anatomies and deformations, via global anatomy and age-dependent distances, defined in Section 6.5.4.2. Once again, the Indian brain is taken as a reference point. The global distance between the average anatomies were calculated using equation 6.2, Since this distance is defined for every voxel we visualise the distance map as a heat map in Figure 6.9 A. A red/yellow voxel indicates significant difference in the average anatomy for population X relative to that for Indian population. Axial slices of the global distance map are shown in the figure. Global distance maps for the Chinese and Japanese are more similar, i.e., left Parietal-temporal-occipital regions has more variation. Whereas, the Caucasian distance map suggests more global anatomy mismatch towards the frontal region.

The pairwise age-dependent distance between Indian and another population was computed using Equation 6.4. These distances are visualised as heatmaps again in Figure 6.9 B. From the predominance of blue pixels in the distance maps it is evident that, the aging trend between the Indian and other populations is similar except in some specific regions. The temporo-parietal regions however show higher age-dependant distances.

Since it is known that anatomical differences exist within a population, a baseline for population comparisons is useful. Hence, an analysis of intra-population deformations was conducted for the Indian population, with respect to its global anatomy. Each individual subject scan (spanning all age groups) was first registered to the global template image using a non-linear approach. Subsequently, the deformation-based distances i.e., the norm of the stationary velocity field parameterisation of the non-rigid deformation [189] were calculated for each subject image from Global template. The average of all these distances is depicted in Figure 6.9 C to illustrate the intra-population variation with respect to the Global template. It should be noted that the distance scale here is 0-4 whereas it is 0-8 for the maps in Figure 6.9A and B. Taking this scale difference into account, it is evident that inter-population differences are significantly more than the intra-population variations.

Previously we observed that the posterior left and right hemispheres exhibited maximum age-dependant distances. To investigate this further, the absolute percentage differences in tissue volumes of a population with respect to Indian population were computed at every time point for the left and right posterior part of the brain. These are plotted in Figure 6.10 for GM and WM. In Figure 6.10, the left posterior brain region specific plots have maximum slopes, which agrees with Figure 6.9C, where relatively maximum age-dependent changes are observed in the posterior region. Additionally, the left region showed comparatively more changes than the right. Comparing the GM and WM plots in Figure 6.10 reveals that the Japanese population exhibits maximum tissue varia-

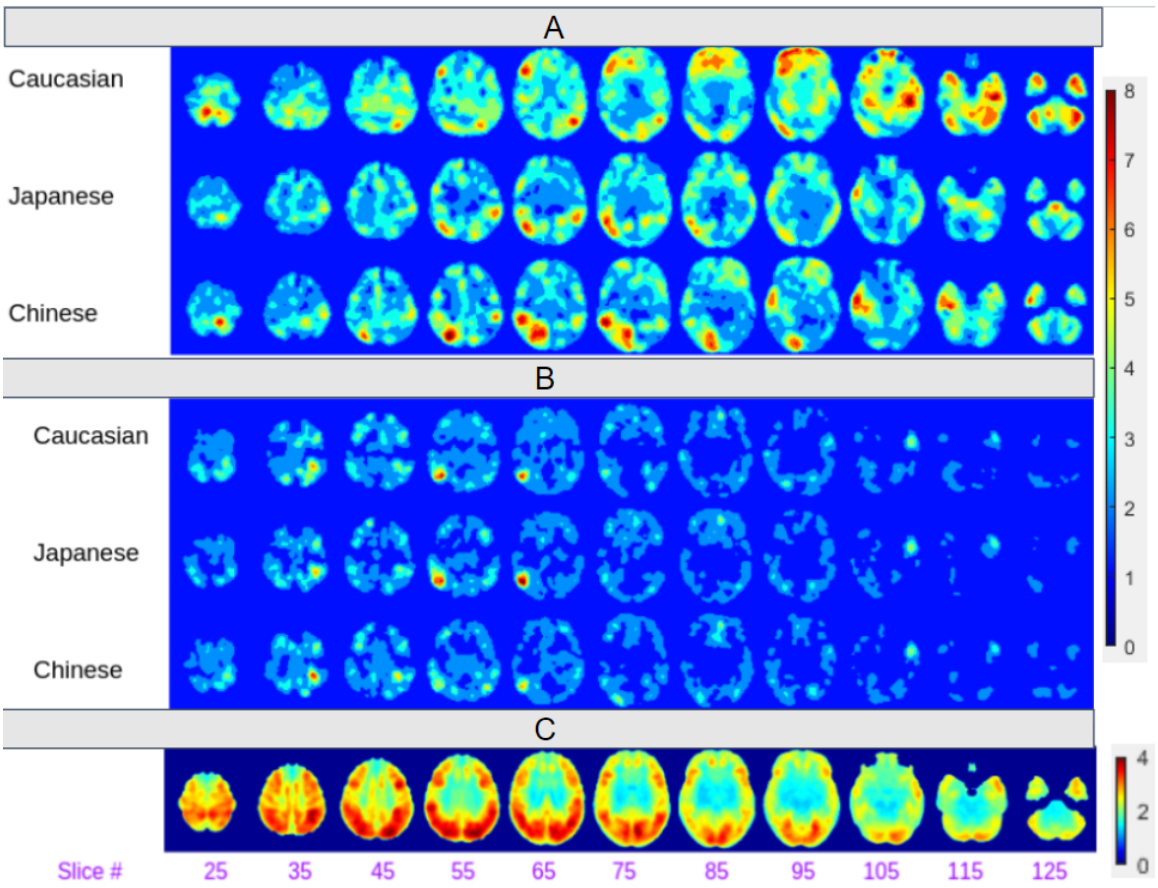

Figure 6.9: Brain aging differences across populations compared to the Indian population: (A) Global anatomy difference in 2D slices and (B) Age-dependent distance analysis. (C) Within-population deformations with respect to global anatomy for the Indian population. Left side correspond to Left side of Brain.

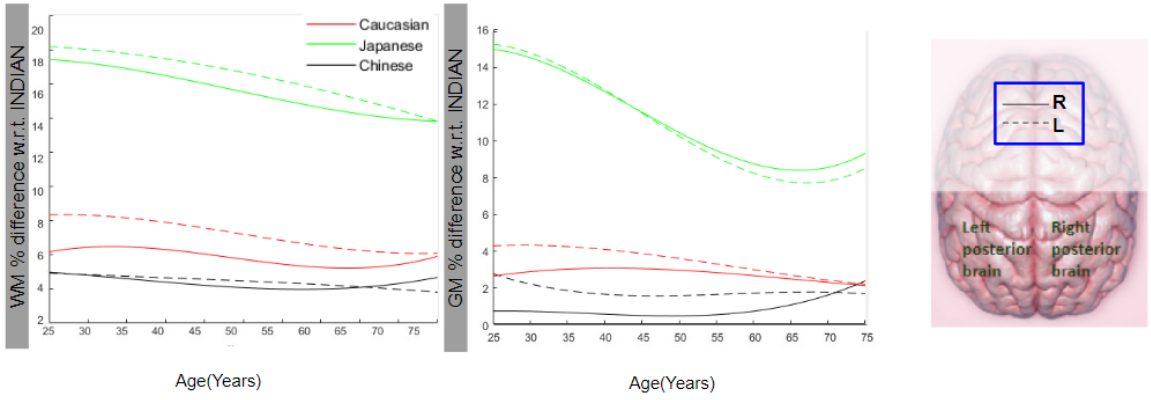

Figure 6.10: GM and WM contribution difference for different population with respect to Indian population for left and right posterior hemispheres

tion over time compared to the Indian population, primarily due to differences in GM. We found that this observation is statistically significant, indicating that there exists a statistically significant

difference between the Indian and Japanese populations. In contrast, the other two groups show some statistically insignificant differences at certain time points.

6.7 Discussion

In this research, we adopted a systematic approach to analyze the neurological aging process across four distinct populations: Indian, Caucasian, Japanese, and Chinese, leveraging a dual-analytical strategy using in T1w structural MRI data. This is a preliminary attempt involving a detailed analysis across multiple populations. Rather than drawing definitive conclusions, we aim to discuss insights from the work for the given sample data, acknowledging the constraints of a smaller dataset size in this study.

The initial approach was based on a conventional group analysis utilizing tissue segmentation with FSL-FAST, showing volume changes across age in gray matter (GM), white matter (WM), and cerebrospinal fluid (CSF). Extending beyond this groundwork, we constructed a continuous model-based analysis to delve deeper into the intricate details of the aging process. Central to our approach was the representation of aging as a diffeomorphic transformation, a conceptualization that enabled a comprehensive intra- and inter-population analysis. This methodological choice allowed for a meticulous examination of both the overarching global anatomy and age-dependent variations, with a special focus on findings in reference to the Indian population.

A significant advancement of this study is the development of an analysis framework capable of comparing population-specific trends in aging both qualitatively and quantitatively by isolating the changes directly associated with aging. This innovation allows us to scrutinize voxel-level diffeomorphic transformations at a population level and discern differences across populations. Consequently, this study essentially underscores the importance of personalized approaches, opening avenues for potential clinical applications that are firmly rooted in a more population-specific and personalized understanding of neurological aging trajectories.

Our findings provide evidence of ventricular expansion and tissue degradation, consistent with previous research [185]. Notably, ventricular expansion accelerates within the age range of 40-45 years, and the results in Figure 6.8 clearly indicate that the Indian population experiences an early onset of ventricular expansion compared to the other populations.Conversely, the Japanese population displays a delayed onset of ventricular expansion compared to other demographic groups. In the early stages, both the Chinese and Caucasian populations exhibit a similar pattern of ventricular expansion. However, in the elderly, the pattern diverges. The rate of expansion gradually stabilizes after approximately 70-75 years of age for the Chinese population, whereas the rate of expansion in the Caucasian population continues to increase, mirroring the trend observed in the other two populations.

Gray matter (GM) degeneration occurs at a faster rate than white matter (WM), which is consistent with the findings in [193]. There were some interesting observations from our study results. The GM follows a linear pattern in both Caucasian and Indian populations in Figure 6.5. In the Chinese population, the degradation rate accelerates during the mid-age group and subsequently stabilizes

in the elderly. Conversely, in the Japanese population, degradation commences at much later ages but then accelerates at a higher rate.

When separately analyzing Cortical GM and sub-cortical GM contractions in Figure 6.8, it becomes evident that cortical GM contraction starts at earlier stages and follows similar trends across all populations, except for Caucasians, where the degradation rate is relatively lower in the elderly. Sub-cortical GM contraction, on the other hand, initiates around the mid-age range in all populations, with a relatively delayed onset observed in the Japanese population. Both cortical and sub-cortical GM tissue degradation increases with aging for all populations, but for the Chinese population, it subsequently stabilizes in the elderly. Japanese population has more white matter degradation compared to the other groups. A DTI-based investigation of WM changes across populations may be needed to confirm this observation.

Hemispherical asymmetry in aging is a well-established phenomenon [186] and was observed in our study as well. In all populations, the left brain consistently exhibited faster ventricular expansion compared to the right brain, with a similar onset. The observed differences in slopes of the left and right ventricular expansion curves indicate that this asymmetry intensifies with aging in each population. Notably, the Chinese population displays more pronounced asymmetrical ventricular expansion with aging compared to other populations. In line with our findings, another study [188] observes that Chinese individuals display more hemispherical asymmetry compared to Caucasians. Asymmetry in ventricular expansion is also observed in conditions such as Parkinson's disease [187]. Understanding population-specific ventricular expansion asymmetry can help define the normal limits tailored to each population and shed light on age-related changes and variations relevant to neurological conditions and the aging process.

Structural differences in the brain are prominent across populations, encompassing both global anatomical variances and age-related structural changes when compared to the Indian population. Global anatomical comparisons reveal that the left parietal-temporal-occipital regions exhibit more variation among Asian populations, while Caucasians show greater anatomical distinctions in the frontal region compared to the Indian population. The global anatomical differences are distributed throughout the brain, whereas age-related differences are relatively localized, with more pronounced deviations occurring in the parieto-temporal regions. These regions are recognized for their susceptibility to significant structural changes, particularly in neurodegenerative conditions such as Alzheimer's disease (AD). Performing automated segmentation-based statistical analysis of tissue changes for small regions can be error-prone, so multiple modalities, like susceptibility variation analysis functional changes etc. can help understand the desirable structural changes associated with aging in this region.

This study is a pioneering effort in comprehending brain aging across diverse populations. It presents a detailed analysis framework that encompasses a comprehensive comparison of tissue degradation, hemispherical asymmetry development, age-related, and independent structural changes in brain anatomy across various populations. The analysis illustrated with sample data, and our intention is to present this as a proof of concept to showcase the possibilities of analysis and potential insights using the proposed analysis framework. The same framework can be used for further explo-

ration of critical factors like language, diet, and mental well-being, disease conditions underscoring the imperative for healthcare strategies tailored to the distinctive aging patterns found within each population. With the framework, the study is motivated to gain a deeper understanding of the underlying patterns and probable reasons for these aging trends. A larger dataset with more imaging modalities will be essential for future research.

Chapter *7*

Conclusion

Our investigation into the structural changes in brain with aging started with the hypothesis that there might be significant differences in brain anatomy and aging among various groups of people. Leveraging insights from the groundwork laid in a prior study by [199], our curiosity shifted toward understanding aging differences. Our journey progressed systematically—from developing essential data for the study to framing the analytical framework and culminating in the detailed analyses that follow. The stages of our work are summarized below.

7.1 A Summary of Thesis Findings

7.1.1 Population-Specific Atlas: Segmentation Map for the Indian Brain Template

Our exploration into brain aging commenced by addressing gaps in our reference population—the Indian population. The initial step in this endeavor is the creation of an atlas. This thesis commenced by building upon the groundwork laid in [199], utilizing the data and template developed in that study. We extended this foundation by collecting expert segmentations on the collected data, leading to the significant contribution of structural probability maps for the Indian population. The template space comparison revealed structural variations across diverse populations, prompting our exploration into aging disparities.

7.1.2 Cross-sectional Data-based Brain Aging Model

Recognizing the challenges of obtaining longitudinal data for aging studies, we introduced an innovative aging model based on continuous deformation applied to a template. This model, generated from cross-sectional data, demonstrated its effectiveness in capturing natural aging trends. Although limited to matured brain growth, the model exhibited spatio-temporal smoothness and consistency. Its potential for clinical applications and the ease with which it accommodates population-specific trends were notable contributions.

With the collected data and the developed aging model for cross-sectional data, we also created the first-ever Indian brain aging model, marking a significant contribution of this thesis. This model

enables the derivation of age-specific brain atlases for the Indian population, providing a standard for comparing the aging process within the population.

The next task is to compare the aging process across populations. However, it goes beyond a simple comparison of images or quantitative measures at different time points. The comparison aims to understand the structural variation of a temporally varying process across populations. Therefore, we formulated a method, which is discussed next.

7.1.3 Method for Aging Model Comparison

In our pursuit of understanding brain aging, we proposed a metric designed to disentangle shape and path variations in aging models. This affine invariant and time interval mismatch-compensated metric provided a robust means of quantifying the difference between aging models, especially when considering cohorts from different populations. The metric's effectiveness was validated using both synthetic and real data, assessing its capability in comparing populations and considering developments in both normal and diseased populations. This metric serves as a crucial component in our aging comparison analysis, which is the main focus of this thesis.

7.1.4 Indian brain aging Database Creation

In our exploration of structural variations in aging, we gathered crucial T1 MRI scans from healthy adults aged 20 to 80 years in the Indian dataset, sourced from multiple sites within India. With over 150 scans collected, we formed decade-specific cohorts of 26 subjects (equally divided by gender) for each time point across all populations. This comprehensive approach involved selecting only physically and psychologically normal subjects, with strict criteria to maintain data integrity. Data collection spanned four different sites, and deliberate efforts were made to standardize the data to mitigate disparities during model development.

The gathered data is cross-sectional, capturing different time points for distinct subjects. While developing a method for group analysis, our focus was specifically on working with cross-sectional data, posing challenges for aging analysis. Efforts were directed towards creating a model tailored for cross-sectional data to facilitate a comprehensive analysis and comparison of structural variations in aging.

7.1.5 Brain aging comparison across populations

This thesis involves conducting a comprehensive comparative study of brain aging. We collected data for the study and developed tools for the analysis. We would like to conclude the insights we gained from the sample dataset we collected for the study. These findings provide valuable insights into aging variations across the population. However, it's important to note that these are not conclusive results, as they are based on a limited sample size used in the study. Nevertheless, this thesis provides a comprehensive pipeline for studying cross-population variation with a larger dataset, enabling the derivation of conclusions about the cross-population variation in brain aging.

We carefully studied the aging process in Chinese, Caucasian, and Japanese populations, using the Indian population as our baseline. When comparing four different populations in terms of brain aging, we observed variations in ventricular expansion, tissue degradation, and aging patterns across hemispheres and in the structural variations specifically in parieto-temporal brain regions. Japanese population shows maximum deviation in aging compared to Indian population by considering all the of the aforementioned variations in aging. Specifically, considering tissue degradation and ventricular expansion as indicators of brain aging, Japanese population displayed a delayed onset aging, along with the most pronounced structural variation in aging compared to the Indian population. Nevertheless, Japanese and Indian populations exhibited minimal hemispherical asymmetry with aging compared to Chinese and Caucasian populations. The Asian populations showed similar brain anatomies compared to Caucasian population but with significant differences in the aging of the anatomy. To gain a comprehensive understanding of these age-related structural changes, future investigations should aim to integrate multiple modalities. Additionally, exploring factors such as education, gender, and more could provide deeper insights into the reasons behind these disparities in brain aging across various populations.

7.2 Future works

Future work could involve expanding our dataset to include a more diverse range of populations, allowing for the creation of models tailored to specific demographic groups. Additionally, further exploration is needed to understand how factors such as education and lifestyle influence brain aging trajectories across different cohorts. In addition to investigating structural changes, future research could delve into cognitive decline and functional connectivity variations to provide a more comprehensive understanding of aging. Ultimately, the goal is to continue building upon this foundation to conduct a more expansive analysis that captures the full complexity of aging and its variations among individuals and populations.

List of Related Publications

[P1] AJ Thottupattu, J Sivaswamy, VP Krishnan, **"A Diffeomorphic Aging Model for Adult Human Brain from Cross-Sectional Data"**, in proceedings of *Nature Scientific Reports*, 2022.

[P2] J Sivaswamy, AJ Thottupattu, R Mehta, R Sheelakumari, C Kesavadas, **"Construction of Indian human brain atlas"**, in proceedings of *Neurology India*, 2019.

[P3] AJ Thottupattu, J Sivaswamy, VP Krishnan, **"A method for image registration via broken geodesics"**, in proceedings of *WBIR, Lecture Notes in Computer Science, vol 13386*, 2022.

[P4] V Mythri, AJ Thottupattu, NA RJ, J Sivaswamy, **"A Method to Remove Size Bias in Sub-Cortical Structure Segmentation"**, in proceedings of *ISBI*, 2022.

[P5] AJ Thottupattu, J Sivaswamy, **"A Fast Method For Shape Template Generation"**, in proceedings of *ICIP*, 2020.

[P6] AJ Thottupattu, J Sivaswamy, Venky P, **"Global Space Modelling Of Biological Processes With Cross-sectional Data"**, in proceedings of *ICVGIP*, 2023.

Appendix

Manifold

A manifold is a topological space locally homeomorphic to a Euclidean space. We can assign local coordinates to points in the manifold. One point can have multiple coordinates, but the transition from one to another should be smooth.
There are three constraints in defining coordinate systems in a Manifold

1. There should be at least one coordinate system such that nearby points should have nearby coordinates
2. In each coordinate system, each point should have unique coordinates
3. For a boundary point, there should be a smooth transition map from one coordinate system to another

Differentiable Manifolds and diffeomorphism

The local homeomorphism of m-dimensional manifold M to Euclidean space $\mathbb{R}^m$ helps to map each point i in the manifold along with its neighborhood. This neighborhood is called a coordinated neighborhood. The mapping from U_i to $\mathbb{R}^m$ is referred to as a coordinate function ϕ_i.

M is a differentiable manifold if
(i) M is a topological space
(ii)M has whole family of $\{(U_i, \phi_i)\}$,
(iii) $\cup_i U_i = M$
(iv)If U_i and U_j are overlapping, then there exists a smooth transition map from one to another and the map is infinitely differentiable

The pair of coordinate neighbourhood and coordinate function (U_i, ϕ_i) , is called a Chart and the whole family $\{(U_i, \phi_i)\}$ is called an Atlas. If the coordinate system is m-dimensional, then there exist m coordinate functions, and all are smooth. Union of two atlases $\{(U_i, \phi_i)\} \cup \{(W_i, \psi_i)\}$ gives another atlas. In other words, the two atlases i.e, $\{(U_i, \phi_i)\}$ and $\{(W_i, \psi_i)\}$ define the same differentiable structure on the manifold M.

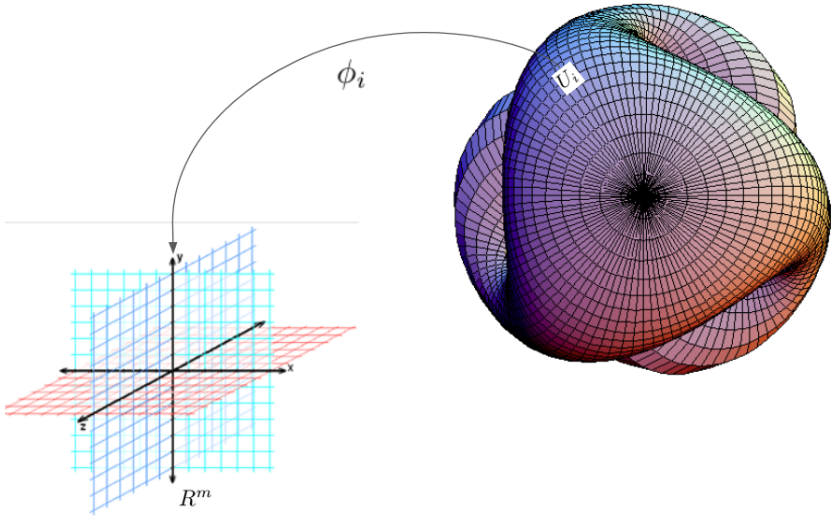

Figure 7.1: Mapping m-dimensional manifold M to Euclidean space $\mathbb{R}^m$

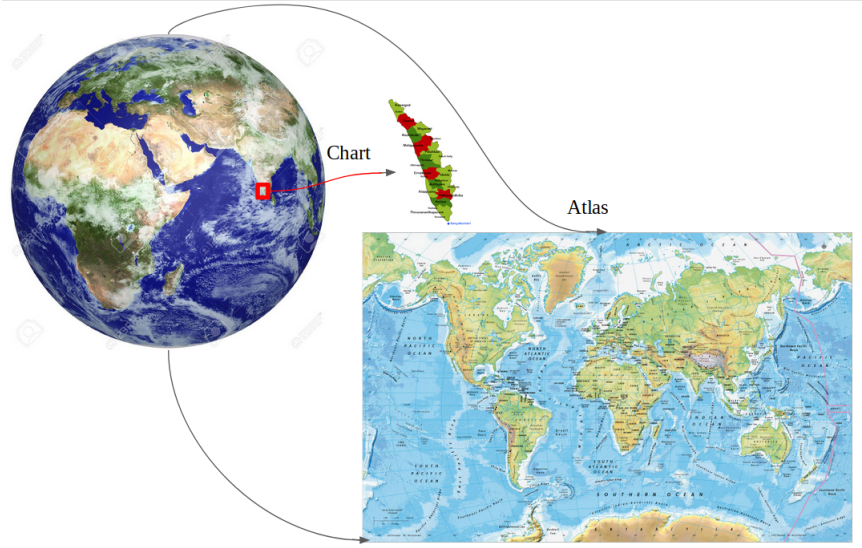

Figure 7.2: Concepts of chart and atlas

Diffeomorphism

Let us consider a map from manifold M to manifold N, $f : M \to N$. It maps a point p in M to a point $f(p)$ in N. Consider charts (U, ϕ) on M and (W, ψ) on N, then $p \in (U, \phi)$ and $f(p) \in (W, \psi)$. Let $\phi(p) = \{x^\mu\}$ and $\psi(f(p)) = \{y^\mu\}$ are the co-ordinates.

From the above diagram, it is easy to see that we can compose mappings $\mathbb{R}^m \to \mathbb{R}^n$ as follows

- $\psi \circ f \circ \phi^{-1} : \mathbb{R}^m \to \mathbb{R}^n$

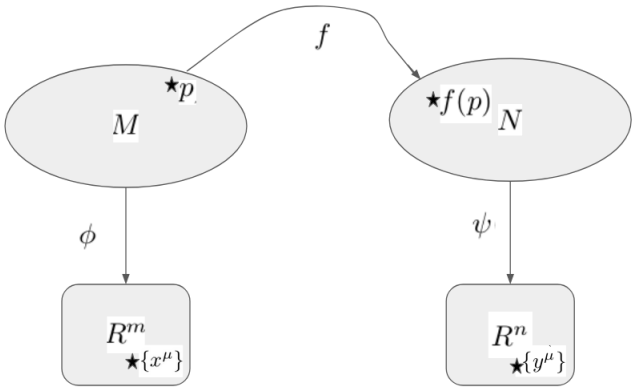

Figure 7.3: Mapping one manifold into another

- If $\psi \circ f \circ \phi^{-1}$ and $\phi \circ f^{-1} \circ \psi^{-1}$ are infinitely differentiable then f is a Diffeomorphism.

Definition: A diffeomorphism is a smooth bijective map between two differentiable manifolds such that both the map and its inverse are infinitely differentiable.
The smooth map f naturally induces a map f_* called the differential map defined as $f_* : T_pM \rightarrow T_{f(p)}N$.

The difference between a homeomorphism and diffeomorphism is that the former requires the deformations to only be continuous whereas, in the latter, the deformations also have to be smooth. Tangent vectors play a crucial role in differential geometry by providing a local linear approximation to the manifold, facilitating the study of smooth deformations and differentiable structures, which is explained next.

Vectors

Given a curve $c(t)$ in a Euclidean space, the tangent at any point p on c is $\frac{\mathrm{dc}(t)}{\mathrm{d}t}$. Consider the curve $c(t)$ in a manifold M. To define the tangent for this curve at a point p, we consider the neighborhood around the point p in the manifold and map it to a Euclidean space using a function $f : M \rightarrow \mathbb{R}$.

We define the tangent vector at point p as a directional derivative of a function $f(c(t))$ at p.

$$\frac{\mathrm{d}f(c(t))}{\mathrm{d}t}|_{t_p} = \frac{\partial f}{\partial x^\mu}\frac{\mathrm{dx}^\mu(\mathrm{c(t)})}{\mathrm{d}t}|t_p \tag{7.1}$$

In practice, vectors are expressed using a Differential operator. A Differential operator X is defined as follows,

$$X = X^\mu \frac{\partial}{\partial x^\mu}\ where\ X^\mu = \frac{\mathrm{dx}^\mu(\mathrm{c(t)})}{\mathrm{d}t}|t = 0 \tag{7.2}$$

So,

$$\frac{\mathrm{d}f(c(t))}{\mathrm{d}t}|_{t=0} \equiv X[f] \tag{7.3}$$

From this, it is clear that X is a tangent vector of M at a point p.

Curve equivalence in a Manifold

Given two curves c_1 and c_2 are said to be equivalent under the following conditions:
(i)$c_1(0) = c_2(0)$
(ii)$\frac{\mathrm{dx}^\mu(\mathrm{c}_1(\mathrm{t}))}{\mathrm{d}t}|_{t=0} = \frac{\mathrm{dx}^\mu(\mathrm{c}_2(\mathrm{t}))}{\mathrm{d}t}|_{t=0}$
The second condition in essence requires the initial tangent vectors of the curves to be the same. If these 2 conditions are satisfied then both c_1 and c_2 have the same differential operator X at p. All such equivalent curves at $p \in M$ with corresponding tangent vectors form a vector space called the Tangent Space of M at p, denoted by T_pM whose basis is $\frac{\partial}{\partial x^\mu}$. All the tangent vectors together form a manifold called Tangent bundle(TM). It is notable that $dim(T_pM) = dim(M)$.

Flows

A vector field X is a mapping $M \to TM$ i.e., a section of TM.

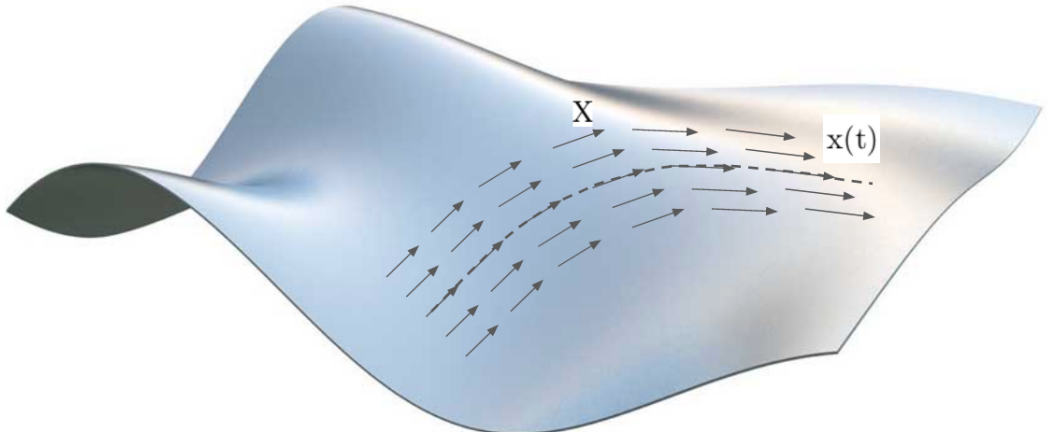

Figure 7.4: An integral curve in the vector field

Using previous definitions, $\frac{\mathrm{d}x^\mu(t)}{\mathrm{d}t} = X^\mu(x(t))$. The solution of this ODE is the desired integral curve. Let $\sigma(t, x(0))$ be the integral curve of X through point x(0) and let $\sigma^\mu(t, x(0))$ denote the co-ordinate. Then,

$$\frac{\mathrm{d}\sigma^\mu(t, x(0))}{\mathrm{d}t} = X^\mu(\sigma(t, x(0))) \tag{7.4}$$

I.e., the time derivative at any point of the curve is the value of the vector field at that point. The flow of a vector field X is defined as the group action of an additive group in $\mathbb{R}$ on M. I.e., the map

$\sigma : \mathbb{R} \times M \to M$ is called flow of the vector field X. Flow satisfies Equation: 6.

$$\sigma(t, \sigma(s, x(0))) = \sigma(s + t, x(0)) \tag{7.5}$$

The vector field X is called infinitesimal generator as at each point the vector field determines the direction of the flow.

Modelling - One-parameter group of transformations

A one-parameter group of diffeomorphisms is a collection of smooth maps from a manifold to itself parameterized by a single real parameter, representing a continuous family of diffeomorphic transformations on the manifold. A one-parameter group of diffeomorphisms is valuable in modeling because it enables a systematic way to describe continuous transformations on a manifold. A one-parameter group of diffeomorphisms is closely related to the concept of Lie groups and Lie algebras in differential geometry which is explained next.

Lie Derivatives

Let $\sigma(t, x)$ and $\tau(t, x)$ be two flows generated by the vector fields X and Y

$$\frac{\mathrm{d}\sigma(t, x)}{\mathrm{d}t} = X^{\mu}(\sigma(t, x)) \tag{7.6}$$

$$\frac{\mathrm{d}\tau(s, x)}{\mathrm{d}s} = Y^{\mu}(\tau(s, x)) \tag{7.7}$$

Now we can check the change of Y w.r.t σ, i.e. finding the derivative of the vector field along the flow of another vector field. This is basically called Lie Derivative. For that, we can compare two points, one on the vector field Y and one on the flow of X. But we cannot do the comparison directly as the points belong to different tangent spaces. I.e. to compare a vector Y at x and vector Y at a nearby point on the curve $\sigma_{\varepsilon}(x)$, we have to use a differential map $(\sigma_{-\varepsilon})_*$ which maps $T_{\sigma_{\varepsilon}(x)}M$ to T_xM. The Lie derivative is easy to be defined as in Equation 9

$$\pounds_X Y = \lim_{\varepsilon \to 0} \frac{1}{\varepsilon}[(\sigma_{-\varepsilon})_* Y|_{\sigma_{\varepsilon}(x)} - Y|_x] \tag{7.8}$$

Lie derivative of Y along X is defined as Lie Bracket
Few points about the Lie bracket

- The difference between the coordinates of these two points is proportional to the Lie bracket
- Geometrically, the Lie bracket shows the non-commutativity of two flows.

- The Lie derivative of a function f along the flow of a vector field X is the directional derivative of f along X.

Lie groups and Lie algebras

Imposing a group structure for a manifold buys us many advantages which will be discussed from this section onwards.
A Lie group is an algebraic group G that also forms a differentiable manifold, where the group operations, multiplication, and inversion, are smooth mappings. Many common geometric transformations of Euclidean space form Lie groups. For example, rotations, translations, and affine transformations all form Lie groups. More generally, Lie groups can be used to describe transformations of smooth manifolds. The dimension of a Lie group G is equal to the dimension of the manifold. Lie algebra is defined as the set of left-invariant vector fields $\mathfrak{g}$ with the Lie bracket.
For any $g \in G$, there exists a unique integral curve of a vector field $X \in \mathfrak{g}$ on entire $\mathbb{R}$.

$$\sigma_g : \mathbb{R} \to G \tag{7.9}$$

i.e., To deform an element in G using some deformation, the corresponding vector field can be used instead of finding the entire deformation. This idea made the deformation calculation step more implementable.

Let a, g be the elements of a Lie group. $R_{ag} = ga$ and $L_{ag} = ag$ are called Right($R_a : G \to G$) and Left($L_a : G \to G$) translations. As multiplication and inverse are smooth for the maps, the translations are diffeomorphisms $G \to G$. There is a special class of vector fields in G invariant under left or right translations. It is this class of vector fields that is of interest as the left-invariant and right-invariant vector fields are diffeomorphisms, and they are complete. As discussed earlier, a map $L_a : G \to G$ induces a differentiable map $L_{a_*} : T_aG \to T_{ag}G$, i.e., the tangent at that point is also translated by the same amount. Now the left invariance for a vector filed X can be defined with the map L_{a_*}. Let X be a vector field; then, it is said to be left invariant if $L_{a_*}X|_g = X|_{ag}$. For convenience, henceforth, we can consider Left translations alone. Left-invariant vector fields form a Lie algebra $\mathfrak{g}$ of G.
Next, we analyze the properties of interest of the flow generated by a left-invariant vector field.
Group homeomorphism is a map that preserves group operations from one group to another. A one-parameter subgroup of the Lie group is defined as a group homeomorphism from a real line to some topological group G. A curve $\sigma(t) : \mathbb{R} \to G$ is called a one-parameter subgroup of G if it satisfies the following conditions:

i. $\sigma_t \circ \sigma_s = \sigma_{t+s}$

ii. σ_0 is the identity map

iii. $\sigma_{-t} = \sigma_t^{-1}$

From Equation (7.9) any vector field $X \in \mathfrak{g}$ can generate a one-parameter subgroup in G. Given a one-parameter subgroup σ, there exists a left-invariant vector field X such that

- $\frac{\mathrm{d}\sigma(t,g)}{\mathrm{d}t} = X$
- $\sigma(0, g) = g$

A one-to-one correspondence exists between one-parameter subgroups of G and Left invariant vector fields on G. An Exponential map is generally used to *map a Lie algebra to its Lie group*. I.e. we can use an exponential map to get the one parameter transformations from a given X.

$$\sigma(t) = exp(tX) \tag{7.10}$$

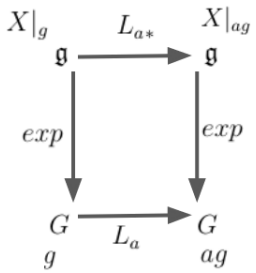

Figure 7.5: Mappings in Lie group

The justification for using this map is that it satisfies all the commutative rules. Note that $exp(0) = e$, i.e., the identity element and exp map help capture only the local group structure from the Lie algebra.

With the above mathematical background, we can now move to the main problem of interest; namely, i) Diffeomorphic registration, ii) Brain Template, iii) Brain Aging Model, and finally, an approach to study iv)Aging Trend Analysis across Populations using the aforementioned tools.

Let us begin by summarizing the key points relevant to a diffeomorphism.

- If $f : M \to N$ is a diffeomorphism, then the derivative $df(p) : T_pM \to T_{f(p)}N$ is a vector space.
- A smooth vector field X on M is a smooth map $X : M \to \mathbb{R}^k$ with all $X(p) \in T_pM$.
- Smooth vector fields on M form a real vector space, and for an open interval I, a smooth map $\gamma : I \to M$ is called the integral curve of vector field if $\dot{\sigma}(t) = X(\sigma(t))$
- A vector field X is said to be complete if, for $p_0 \in M$, there is an integral curve $\sigma(0) = p_0$. Every vector field on M is complete for a compact manifold (closed and bounded).
- Analogy between Lie groups and Diffeomorphisms only works well when the manifold M is compact (i.e., closed and bounded).

Bibliography

[1] Tun Jao, Chun-Yuan Chang, Chia-Wei Li, Der-Yow Chen, Edzer Wu, Chang-Wei Wu, Chi-Hsuan Tsou, Chien-Chang Ho, and Jyh-Horng Chen. Development of ntu standard chinese brain template: morphologic and functional comparison with mni template using magnetic resonance imaging. In Engineering in Medicine and Biology Society, 2009. EMBC 2009. Annual International Conference of the IEEE, pages 4779–4782. IEEE, 2009.

[2] Hitoshi T Uchiyama, Ayumi Seki, Daisuke Tanaka, Tatsuya Koeda, et al. A study of the standard brain in japanese children: Morphological comparison with the mni template. Brain and Development, 35(3):228–235, 2013.

[3] Nneka Isamah, Warachal Faison, Martha E Payne, James MacFall, David C Steffens, John L Beyer, K Ranga Krishnan, and Warren D Taylor. Variability in frontotemporal brain structure: the importance of recruitment of african americans in neuroscience research. PLoS One, 5(10):e13642, 2010.

[4] Florent Lalys, Claire Haegelen, Jean-Christophe Ferre, Omar El-Ganaoui, and Pierre Jannin. Construction and assessment of a 3-t mri brain template. Neuroimage, 49(1):345–354, 2010.

[5] Hyunna Lee, Byung Il Yoo, Ji Won Han, Jung Jae Lee, San Yeo Wool Oh, Eun Young Lee, Jae Hyoung Kim, and Ki Woong Kim. Construction and validation of brain mri templates from a korean normal elderly population.

[6] Wu, J., Sun, T., Yu, B., Li, Z., Wu, Q., Wang, Y., Qian, Z., Zhang, Y., Jiang, L., Wei, H. Age-specific structural fetal brain atlases construction and cortical development quantification for chinese population. NeuroImage , 241, 118412 ,2021

[7] Xie, W., Richards, J.E., Lei, D., Lee, K., Gong, Q.: Comparison of the brain development trajectory between chinese and u.s. children and adolescents. Frontiers in Systems Neuroscience,8, 2015

[8] Naren Rao, Haris Jeelani, Rashmin Achalia, Garima Achalia, Arpitha Jacob, Rose Bharath, Shivarama Varambally, Ganesan Venkatasubramanian, and Phaneendra Yalavarthy. Population differences in brain morphology: Need for population specific brain template. Psychiatry Research: Neuroimaging, 265, 03 2017.

[9] Aljabar, P., Heckemann, R., Hammers, A., Hajnal, J. V. & Rueckert, D. Classifier selection strategies for label fusion using large atlas databases. In Ayache, N., Ourselin, S. & Maeder, A. (eds.) Medical Image Computing and Computer-Assisted Intervention, 523–531, 10.1007/978-3-540-75757-3_64 (Springer Berlin Heidelberg, 2007.

[10] Babalola, K. et al. Automatic segmentation of the caudate nuclei using active appearance models. Biomed Eng Online. 10 ,2007.

[11] Patenaude, B. Bayesian statistical models of shape and appearance for subcortical brain segmentation ,2007.

[12] Murgasova, M. et al. Segmentation of brain mri in young children. In Larsen, R., Nielsen, M. & Sporring, J. (eds.) Medical Image Computing and Computer-Assisted Intervention – MICCAI 2006, 687–694, 10.1007/11866565_84 (Springer Berlin Heidelberg, Berlin, Heidelberg, 2006.

[13] Mehta, R. & Sivaswamy, J. M-net: A convolutional neural network for deep brain structure segmentation. 437–440, 10.1109/ISBI.2017.7950555 ,2017.

[14] Liu, L. et al. ψ-net: Stacking densely convolutional lstms for sub-cortical brain structure segmentation. IEEE Transactions on Medical Imaging 39, 2806–2817, 10.1109/TMI.2020.2975642 ,2020.

[15] McDuff, T. & Sumi, S. M. Subcortical degeneration in alzheimer's disease. Neurology 35, 123–123, 10.1212/WNL.35.1.123 (1985.

[16] Tang, X. et al. Regional subcortical shape analysis in premanifest huntington's disease. Human brain mapping 40(5), 1419–1433, https://doi.org/10.1002/hbm.24456 ,2019.

[17] Looi, J. et al. Morphometric analysis of subcortical structures in progressive supranuclear palsy: in vivo evidence of neostriatal and mesencephalic atrophy. Psychiatry research 194, 163–75, 10.1016/j.pscychresns.2011.07.013 ,2011.

[18] Jamea, A. et al. Volumetric and shape analysis of the subcortical regions in schizophrenia patients: A pilot studyvolumetric and shape analysis of the subcortical regions in schizophrenia patients: A pilot study. Journal of Clinical Imaging Science 9, 1, 10.4103/jcis.JCIS_61_18 ,2019.

[19] Lu, Y. et al. The volumetric and shape changes of the putamen and thalamus in first episode, untreated major depressive disorder. NeuroImage: Clinical 11, 658–666, https://doi.org/10.1016/j.nicl.2016.04.008 ,2016.

[20] Landman, B. & Warfield, S. Miccai 2012 workshop on multi-atlas labeling. Create Space Independent Publishing Platform 2 ,2012.

[21] Linguraru, M. G. et al. Segmentation propagation from deformable atlases for brain mapping and analysis. Brain Research Journal 1 ,2007.

[22] Shattuck, D. et al. Construction of a 3d probabilistic atlas of human cortical structures. neuroimage ,2007.

[23] Rolf, A. H., Joseph, V. H., Paul, A., Daniel, R. & Alexander, H. Automatic anatomical brain mri segmentation combining label propagation and decision fusion. NeuroImage 33, 115–126 ,2006.

[24] Jafari-Khouzani, K., Elisevich, K., Patel, S. & Soltanian-Zadeh, H. Dataset of magnetic resonance images of nonepileptic subjects and temporal lobe epilepsy patients for validation of hippocampal segmentation techniques. Neuroinformatics 9, 335–46, 10.1007/s12021-010-9096-4 ,2011.

[25] Sivaswamy, J., Thottupattu, A. J., Mehta, R., Sheelakumari, R. & Kesavadas, C. Construction of indian human brain atlas. Neurol India 67, 229–34 ,2019.

[26] Tustison, N. J. et al. N4itk: improved n3 bias correction. IEEE transactions on medical imaging 29, 1310–1320 ,2010.

[27] Manjón, J. V., Coupé, P., Martí-Bonmatí, L., Collins, D. L. & Robles, M. Adaptive non-local means denoising of mr images with spatially varying noise levels. Journal of Magnetic Resonance Imaging 31, 192–203 ,2010.

[28] Smith, S. M. Fast robust automated brain extraction. Human Brain Mapping 17 ,2002.

[29] Lancaster, J. et al. Automated talairach atlas labels for functional brain mapping. Human Brain Mapping 10, 120–131, 10.1002/1097-0193(200007)10:3<120::AID-HBM30>3.0.CO;2-8 ,2000.

[30] Yushkevich, P. A. et al. User-guided 3D active contour segmentation of anatomical structures: Significantly improved efficiency and reliability. Neuroimage 31, 1116–1128 ,2006.

[31] Bruce, F. et al. Whole brain segmentation: Automated labeling of neuroanatomical structures in the human brain. Neuron 33(3), 341–355, https://doi.org/10.1016/S0896-6273(02)00569-X ,2002.

[32] Patenaude, B., Smith, S., Kennedy, D. & Jenkinson, M. A bayesian model of shape and appearance for subcortical brain segmentation. NeuroImage 56, 907–22, 10.1016/j.neuroimage.2011.02.046 ,2011.

[33] Cicek, O., Abdulkadir, A., Lienkamp, S., Brox, T. & Ronneberger, O. 3d u-net: Learning dense volumetric segmentation from sparse annotation. ArXiv abs/1606.06650 ,2016.

[34] Lee, K., Zung, J., Li, P., Jain, V. & Seung, H. Superhuman accuracy on the snemi3d connectomics challenge. ArXiv abs/1706.00120 ,2017.

[35] Huang, G., Liu, Z., Van Der Maaten, L. & Weinberger, K. Q. Densely connected convolutional networks. In Proceedings of the IEEE conference on computer vision and pattern recognition, 4700–4708 ,2017.

[36] Milletari, F., Navab, N. & Ahmadi, S.-A. V-net: Fully convolutional neural networks for volumetric medical image segmentation. 565–571, 10.1109/3DV.2016.79 ,2016.

[37] Dice, L. R. Measures of the amount of ecologic association between species. Ecology 26, 297–302 ,1945.

[38] Rockafellar, R. & Wets, R. Variational Analysis, vol. 317 ,2004.

[39] Mirza Faisal Beg Ali R. Khan, Lei Wang. Freesurfer-initiated fully-automated subcortical brain segmentation in mri using large deformation diffeomorphic metric mapping. Neuroimage, 41(3):735–746, 2008 July.

[40] Babak A Ardekani and Alvin H Bachman. Model-based automatic detection of the anterior and posterior commissures on mri scans. Neuroimage, 46(3):677–682, 2009.

[41] John Ashburner and Karl J Friston. Voxel-based morphometry: the methods. Neuroimage, 11(6):805–821, 2000.

[42] B. Avants, T. Sundaram, J.T. Duda, J.C. Gee, and L Ng. Insight into images. ch. nonrigid image registration. pages 307–348, 2004.

[43] Brian B Avants, Paul Yushkevich, John Pluta, David Minkoff, Marc Korczykowski, John Detre, and James C Gee. The optimal template effect in hippocampus studies of diseased populations. Neuroimage, 49(3):2457–2466, 2010.

[44] Jordan Bai, Muhammad Farid Abdul-Rahman, Anne Rifkin-Graboi, Yap-Seng Chong, Kenneth Kwek, Seang-Mei Saw, Keith M Godfrey, Peter D Gluckman, Marielle V Fortier, Michael J Meaney, et al. Population differences in brain morphology and microstructure among chinese, malay, and indian neonates. PLoS One, 7(10):e47816, 2012.

[45] akamura m. Bouix S. Pohl K. a hierarchical algorithm for mr brain image parcellation. TMI, 26:1201–12, 2007.

[46] C.E. Coffey, J.A. Saxton, G. Ratcliff, R.N. Bryan, and J.F. Lucke. Relation of education to brain size in normal aging. Neurology, 53(1):189–189, 1999.

[47] D Louis Collins, Colin J Holmes, Terrence M Peters, and Alan C Evans. Automatic 3-d model-based neuroanatomical segmentation. Human brain mapping, 3(3):190–208, 1995.

[48] David Alexander Dickie, Susan D Shenkin, Devasuda Anblagan, Juyoung Lee, Manuel Blesa Cabez, David Rodriguez, James P Boardman, Adam Waldman, Dominic E Job, and Joanna M Wardlaw. Whole brain magnetic resonance image atlases: a systematic review of existing atlases and caveats for use in population imaging. Frontiers in neuroinformatics, 11, 2017.

[49] Alan C Evans, D Louis Collins, SR Mills, ED Brown, RL Kelly, and Terry M Peters. 3d statistical neuroanatomical models from 305 mri volumes. In Nuclear Science Symposium and Medical Imaging Conference, 1993., 1993 IEEE Conference Record., pages 1813–1817. IEEE, 1993.

[50] Alan C Evans, Andrew L Janke, D Louis Collins, and Sylvain Baillet. Brain templates and atlases. Neuroimage, 62(2):911–922, 2012.

[51] Nneka Isamah, Warachal Faison, Martha E Payne, James MacFall, David C Steffens, John L Beyer, K Ranga Krishnan, and Warren D Taylor. Variability in frontotemporal brain structure: the importance of recruitment of african americans in neuroscience research. PLoS One, 5(10):e13642, 2010.

[52] Tun Jao, Chun-Yuan Chang, Chia-Wei Li, Der-Yow Chen, Edzer Wu, Chang-Wei Wu, Chi-Hsuan Tsou, Chien-Chang Ho, and Jyh-Horng Chen. Development of ntu standard chinese brain template: morphologic and functional comparison with mni template using magnetic resonance imaging. In Engineering in Medicine and Biology Society, 2009. EMBC 2009. Annual International Conference of the IEEE, pages 4779–4782. IEEE, 2009.

[53] Florent Lalys, Claire Haegelen, Jean-Christophe Ferre, Omar El-Ganaoui, and Pierre Jannin. Construction and assessment of a 3-t mri brain template. Neuroimage, 49(1):345–354, 2010.

[54] Jack L. Lancaster, Marty G. Woldorff, Lawrence M. Parsons, Mario Liotti, Catarina S. Freitas, Lacy Rainey, Peter V. Kochunov, Dan Nickerson, Shawn A. Mikiten, and Peter T. Fox. Automated talairach atlas labels for functional brain mapping. Human Brain Mapping, 10(3):120–131, 2000.

[55] Hyunna Lee, Byung Il Yoo, Ji Won Han, Jung Jae Lee, San Yeo Wool Oh, Eun Young Lee, Jae Hyoung Kim, and Ki Woong Kim. Construction and validation of brain mri templates from a korean normal elderly population. Psychiatry investigation, 13(1):135–145, 2016.

[56] Jae Sung Lee, Dong Soo Lee, Jinsu Kim, Yu Kyeong Kim, Eunjoo Kang, Hyejin Kang, Keon Wook Kang, Jong Min Lee, Jae-Jin Kim, Hae-Jeong Park, et al. Development of korean standard brain templates. Journal of Korean medical science, 20(3):483–488, 2005.

[57] Peipeng Liang, Lin Shi, Nan Chen, Yishan Luo, Xing Wang, Kai Liu, Vincent CT Mok, Winnie CW Chu, Defeng Wang, and Kuncheng Li. Construction of brain atlases based on a multi-center mri dataset of 2020 chinese adults. Scientific reports, 5, 2015.

[58] Pravat K Mandal, Rashima Mahajan, and Ivo D Dinov. Structural brain atlases: design, rationale, and applications in normal and pathological cohorts. Journal of Alzheimer's Disease, 31(s3):S169–S188, 2012.

[59] José V Manjón, Pierrick Coupé, Luis Martí-Bonmatí, D Louis Collins, and Montserrat Robles. Adaptive non-local means denoising of mr images with spatially varying noise levels. Journal of Magnetic Resonance Imaging, 31(1):192–203, 2010.

[60] John Mazziotta, Arthur Toga, Alan Evans, Peter Fox, Jack Lancaster, Karl Zilles, Roger Woods, Tomas Paus, Gregory Simpson, Bruce Pike, et al. A probabilistic atlas and reference system for the human brain: International consortium for brain mapping (icbm). Philosophical Transactions of the Royal Society of London B: Biological Sciences, 356(1412):1293–1322, 2001.

[61] John C Mazziotta, Arthur W Toga, Alan Evans, Peter Fox, and Jack Lancaster. A probabilistic atlas of the human brain: Theory and rationale for its development: The international consortium for brain mapping (icbm). Neuroimage, 2(2):89–101, 1995.

[62] Naren P Rao, Haris Jeelani, Rashmin Achalia, Garima Achalia, Arpitha Jacob, Rose Dawn Bharath, Shivarama Varambally, Ganesan Venkatasubramanian, and Phaneendra K Yalavarthy. Population differences in brain morphology: Need for population specific brain template. Psychiatry Research-Neuroimaging, 265:1–8, 2017.

[63] Adisetiyo V Hojatkashani C Salamon G Narr KL Poldrack RA Bilder RM Toga AW Shattuck DW, Mirza M. Construction of a 3d probabilistic atlas of human cortical structures. neuroimage, 2007.

[64] Jean Talairach and Pierre Tournoux. Co-planar stereotaxic atlas of the human brain. 3-dimensional proportional system: an approach to cerebral imaging. 1988.

[65] Yuchun Tang, Cornelius Hojatkashani, Ivo D Dinov, Bo Sun, Lingzhong Fan, Xiangtao Lin, Hengtao Qi, Xue Hua, Shuwei Liu, and Arthur W Toga. The construction of a chinese mri brain atlas: A morphometric comparison study between chinese and caucasian cohorts. Neuroimage, 51(1):33–41, 2010.

[66] Nicholas J Tustison, Brian B Avants, Philip A Cook, Yuanjie Zheng, Alexander Egan, Paul A Yushkevich, and James C Gee. N4itk: improved n3 bias correction. IEEE transactions on medical imaging, 29(6):1310–1320, 2010.

[67] N. et al. Tzourio-Mazoyer. Automated anatomical labeling of activations in spm using a macroscopic anatomical parcellation of the mni mri single-subject brain. NeuroImage, 15:273–289, 2002.

[68] Hitoshi T Uchiyama, Ayumi Seki, Daisuke Tanaka, Tatsuya Koeda, et al. A study of the standard brain in japanese children: Morphological comparison with the mni template. Brain and Development, 35(3):228–235, 2013.

[69] Wang Xing, Chen Nan, Zuo ZhenTao, Xue Rong, Jing Luo, Yan Zhuo, Shen DingGang, and Li KunCheng. Probabilistic mri brain anatomical atlases based on 1,000 chinese subjects. PloS one, 8(1):e50939, 2013.

[70] Yongyue Zhang, Michael Brady, and Stephen Smith. Segmentation of brain mr images through a hidden markov random field model and the expectation-maximization algorithm. IEEE transactions on medical imaging, 20(1):45–57, 2001.

[71] Bharath Holla, Paul Taylor, Daniel Glen, John Lee, Nilakshi Vaidya, Urvakhsh Mehta, Ganesan Venkatasubramanian, Pramod Pal, Jitender Saini, Naren Rao, Chirag Ahuja, Rebecca Kuriyan, Murali Krishna, Debashish Basu, Kartik Kalyanram, Amit Chakrabarti, Dimitri Papadopoulos Orfanos, Gareth Barker, Robert Cox, and Vivek Benegal. A series of five population-specific indian brain templates and atlases spanning ages 6–60 years. Human Brain Mapping, 41, 08 2020.

[72] Helmut Alt and MICHAEL GODAU. Computing the fréchet distance between two polygonal curves. Int. J. Comput. Geometry Appl., 5:75–91, 03 1995.

[73] E. Belogay, Carlos Cabrelli, Ursula Molter, and Ron Shonkwiler. Calculating the hausdorff distance between curves. Inf. Process. Lett., 64:17–22, 10 1997.

[74] Timothy Brown. Individual differences in human brain development. Wiley Interdisciplinary Reviews: Cognitive Science, 8, 11 2016.

[75] Lei Chen, M. Tamer Özsu, and Vincent Oria. Robust and fast similarity search for moving object trajectories. In Proceedings of the 2005 ACM SIGMOD International Conference on Management of Data, SIGMOD '05, page 491–502, New York, NY, USA, 2005. Association for Computing Machinery.

[76] Yu Yong Choi, Jang Jae Lee, Kyu Yeong Choi, Uk-Su Choi, Eun Hyun Seo, IL Han Choo, Hoowon Kim, Min-Kyung Song, Seong-Min Choi, Soo Hyun Cho, Youngshik Choe, Byeong C. Kim, and Kun Ho Lee. Multi-racial normative data for lobar and subcortical brain volumes in old age: Korean and caucasian norms may be incompatible with each other†. Frontiers in Aging Neuroscience, 13, 2021.

[77] B. C. Davis, P. T. Fletcher, E. Bullitt, and S. Joshi. Population shape regression from random design data. In 2007 IEEE 11th International Conference on Computer Vision, pages 1–7, 2007.

[78] Paul T. Fillmore, Michelle Phillips-Meek, and J. Richards. Age-specific mri brain and head templates for healthy adults from 20 through 89 years of age. Frontiers in Aging Neuroscience, 7, 2015.

[79] James Fishbaugh, Stanley Durrleman, and Guido Gerig. Estimation of smooth growth trajectories with controlled acceleration from time series shape data. In Gabor Fichtinger, Anne Martel, and Terry Peters, editors, Medical Image Computing and Computer-Assisted Intervention – MICCAI 2011, pages 401–408, Berlin, Heidelberg, 2011. Springer Berlin Heidelberg.

[80] M. Maurice Fréchet. Sur quelques points du calcul fonctionnel, December 1906.

[81] Ali Gholipour, Caitlin K. Rollins, Clemente Velasco-Annis, Abdelhakim Ouaalam, Alireza Akhondi-Asl, Onur Afacan, Cynthia M. Ortinau, Sean Clancy, Catherine Limperopoulos, Edward Yang, Judy A. Estroff, and Simon K. Warfield. A normative spatiotemporal mri atlas of the fetal brain for automatic segmentation and analysis of early brain growth. Scientific Reports, 7(1):476–476, 2017.

[82] Mehdi Hadj-Hamou, Marco Lorenzi, Nicholas Ayache, and Xavier Pennec. Longitudinal analysis of image time series with diffeomorphic deformations: A computational framework based on stationary velocity fields. Frontiers in Neuroscience, 10, 2016.

[83] Marek Kijonka, Damian Borys, Krzysztof Psiuk-Maksymowicz, Kamil Gorczewski, Piotr Wojcieszek, Bartosz Kossowski, Artur Marchewka, Andrzej Swierniak, Maria Sokol, and Barbara Bobek-Billewicz. Whole brain and cranial size adjustments in volumetric brain analyses of sex- and age-related trends. Frontiers in Neuroscience, 14, 2020.

[84] Marco Lorenzi and X. Pennec. Efficient parallel transport of deformations in time series of images: From schilds to pole ladder. Journal of Mathematical Imaging and Vision, 50:5–17, 2013.

[85] Daniel S. Marcus, Tracy H. Wang, Jamie Parker, John G. Csernansky, John C. Morris, and Randy L. Buckner. Open Access Series of Imaging Studies (OASIS): Cross-sectional MRI Data in Young, Middle Aged, Nondemented, and Demented Older Adults. Journal of Cognitive Neuroscience, 19(9):1498–1507, 09 2007.

[86] Michael I. Miller. Computational anatomy: shape, growth, and atrophy comparison via diffeomorphisms. NeuroImage, 23:S19 – S33, 2004. Mathematics in Brain Imaging.

[87] Marc Niethammer, Yang Huang, and François-Xavier Vialard. Geodesic regression for image time-series. In Gabor Fichtinger, Anne Martel, and Terry Peters, editors, Medical Image Computing and Computer-Assisted Intervention – MICCAI 2011, pages 655–662, Berlin, Heidelberg, 2011. Springer Berlin Heidelberg.

[88] Kazunori Sato, Yasuyuki Taki, Hiroshi Fukuda, and Ryuta Kawashima. Neuroanatomical database of normal japanese brains. Neural networks : the official journal of the International Neural Network Society, 16:1301–10, 12 2003.

[89] Alphin Thottupattu, Jayanthi Sivaswamy, and Venkateswaran Krishnan. A diffeomorphic aging model for adult human brain from cross-sectional data. Scientific Reports, 12:12638, 07 2022.

[90] V. Arsigny et al. A Log-Euclidean Framework for Statistics on Diffeomorphisms. MICCAI, 9:924–31, 2006.

[91] Jiangjie Wu, Taotao Sun, Boliang Yu, Zhenghao Li, Qing Wu, Yutong Wang, Zhaoxia Qian, Yuyao Zhang, Ling Jiang, and Hongjiang Wei. Age-specific structural fetal brain atlases construction and cortical development quantification for chinese population. NeuroImage, 241:118412, 2021.

[92] Wanze Xie, John E. Richards, Du Lei, Kang Lee, and Qiyong Gong. Comparison of the brain development trajectory between chinese and u.s. children and adolescents. Frontiers in Systems Neuroscience, 8, 2015.

[93] Richard A.I. Bethlehem, Jakob Seidlitz, Simon White, Jacob Vogel, Kevin Anderson, Chris Adamson, Sophie Adler-Wagstyl, George Alexopoulos, Evdokia Anagnostou, Ariosky Areces Gonzalez, Duncan Astle, Bonnie Auyeung, Muhammad Ayub, Gareth Ball, Simon Baron-Cohen, Richard Beare, Saashi Bedford, Vivek Benegal, Frauke Beyer, and Aaron Alexander-Bloch. Brain charts for the human lifespan, 06 2021.

[94] Kazunori Sato, Yasuyuki Taki, Hiroshi Fukuda, and Ryuta Kawashima. Neuroanatomical database of normal japanese brains. Neural Networks, 16(9):1301–1310, 2003. Neuroinformatics.

[95] Jason R. Taylor, Nitin Williams, Rhodri Cusack, Tibor Auer, Meredith A. Shafto, Marie Dixon, Lorraine K. Tyler, Cam-CAN, and Richard N. Henson. The cambridge centre for ageing and neuroscience (cam-can) data repository: Structural and functional mri, meg, and cognitive data from a cross-sectional adult lifespan sample. NeuroImage, 144:262–269, 2017. Data Sharing Part II.

[96] V. Arsigny et al. A Log-Euclidean Framework for Statistics on Diffeomorphisms. MICCAI, 9:924–31, 2006.

[97] Devin Wahl, Alyssa Cavalier, and Thomas Larocca. Novel strategies for healthy brain aging. Exercise and sport sciences reviews, 49, 04 2021.

[98] Dongtao Wei, Kaixiang Zhuang, Qunlin Chen, Wenjing Yang, Liu Wei, Kangcheng Wang, Jiangzhou Sun, and Jiang Qiu. Structural and functional mri from a cross-sectional southwest university adult lifespan dataset (sald), 01 2018.

[99] Mirza Faisal Beg, Michael Miller, Alain Trouvé, and Laurent Younes. Computing large deformation metric mappings via geodesic flows of diffeomorphisms. International Journal of Computer Vision, 61:139–157, 02 2005.

[100] K. Brodmann. The principles of comparative localisation in the cerebralcortex based on cytoarchitectonics. London: Smith-Gordon, 1994.

[101] CHAIM BROIT. Optimal registration of deformed images. 1981.

[102] et.al. Ceritoglu. Large deformation diffeomorphic metric mapping registration of reconstructed 3d histological section images and in vivo mr images. Frontiers in human neuroscience, 4, 43, 2005.

[103] Tage Emil Christensen, Niels Boye Olsen, and Jeppe Dyre. Shoving model for viscous flow. World Scientific, page 375, 1996.

[104] Claire Cury, Joan Alexis Glaunès, and Olivier Colliot. Diffeomorphic Iterative Centroid Methods for Template Estimation on Large Datasets. In Frank Nielsen, editor, Geometric Theory of Information, volume Chapter 10, pages 273–299. Springer, 2014.

[105] Rahul S. Desikan, Howard J. Cabral, Fabio Settecase, Christopher P. Hess, William P. Dillon, Christine M. Glastonbury, Michael W. Weiner, Nicholas J. Schmansky, David H. Salat, and Bruce Fischl. Automated mri measures predict progression to alzheimer's disease. Neurobiology of Aging, 31(8):1364 – 1374, 2010. Alzheimer's Disease Neuroimaging Initiative (ADNI) Studies.

[106] Eickhoff et.al. A new SPM toolbox for combining probabilistic cytoarchitectonic maps andfunctional imaging data. NeuroImage, 25:1325–1335, 2005.

[107] Mazziotta et.al. A probabilistic atlas and reference system for the human brain: InternationalConsortium for Brain Mapping (ICBM). Philos. Trans. R. Soc. London B Biol. Sci., 356:1293–1322, 2001.

[108] Shattuck et.al. Construction of a 3D probabilistic atlasof human cortical structures. NeuroImage, 39:1064–1080, 2008.

[109] Tzourio-Mazoyer et.al. Automated anatomical labeling of activations in SPMusing a macroscopic anatomical parcellation of the MNI MRI single-subject brain. NeuroImage, 15:273–289, 2002.

[110] Vercauteren et.al. Symmetric log-domain diffeomorphic registration: A demons-based approach. MICCAI, pages 754–761, 2008.

[111] Collins D.L. Milner B Evans, A.C. An MRI-based stereotaxic atlas from 250young normal subjects. Proc 22nd Annual Symposium, Society for Neuroscience, 18:408, 1992.

[112] James Fishbaugh, Stanley Durrleman, and Guido Gerig. Estimation of smooth growth trajectories with controlled acceleration from time series shape data. pages 401–408, 2011.

[113] M. Hernandez, M. N. Bossa, and S. Olmos. Registration of anatomical images using geodesic paths of diffeomorphisms parameterized with stationary vector fields. IEEE 11th International Conference on Computer Vision, pages 1–8, Oct 2007.

[114] Hoge R. Collins D.L. Woods R. Toga A.W. Evans A.C Holmes, C.J. Enhancement of MR images using registration for signal averaging. Proc 22nd Annual Symposium, Society for Neuroscience, 22(2):324–333, 1998.

[115] Edgar M. Housepian. Atlas d'anatomie stereotaxique du telencephale. JAMA Neurology, 18(3):335–336, 03 1968.

[116] Jr Jack, Clifford R., Heather J. Wiste, Prashanthi Vemuri, Stephen D. Weigand, Matthew L. Senjem, Guang Zeng, Matt A. Bernstein, Jeffrey L. Gunter, Vernon S. Pankratz, Paul S. Aisen, Michael W. Weiner, Ronald C. Petersen, Leslie M. Shaw, John Q. Trojanowski, David S. Knopman, and the Alzheimer's Disease Neuroimaging Initiative. Brain beta-amyloid measures and magnetic resonance imaging atrophy both predict time-to-progression from mild cognitive impairment to Alzheimer's disease. Brain, 133(11):3336–3348, 2010.

[117] Terry L. Jernigan, Sarah L. Archibald, Christine Fennema-Notestine, Anthony C. Gamst, Julie C. Stout, Julie Bonner, and John R. Hesselink. Effects of age on tissues and regions of the cerebrum and cerebellum. Neurobiology of Aging, 22(4):581 – 594, 2001.

[118] Brad C. Davis·P. Thomas Fletcher·Elizabeth Bullitt·Sarang Joshi. Population shape regression from random design data. Int J Comput Vis, 90:255–266., 2010.

[119] A. R. Khan and M. F. Beg. Representation of time-varying shapes in the large deformation diffeomorphic framework. ISBI, pages 1521–1524, 2008.

[120] Michael I. Miller, Alain Trouvé, and Laurent Younes. On the metrics and euler-lagrange equations of computational anatomy. Annual Review of Biomedical Engineering, 4(1):375–405, 2002.

[121] James O'Connor. Thomas willis and the background to cerebri anatome. Journal of the Royal Society of Medicine, 96:139–43, 04 2003.

[122] Naftali Raz, Ulman Lindenberger, Karen M. Rodrigue, Kristen M. Kennedy, Denise Head, Adrienne Williamson, Cheryl Dahle, Denis Gerstorf, and James D. Acker. Regional Brain Changes in Aging Healthy Adults: General Trends, Individual Differences and Modifiers. Cerebral Cortex, 15(11):1676–1689, 02 2005.

[123] David H. Salat, Randy L. Buckner, Abraham Z. Snyder, Douglas N. Greve, Rahul S.R. Desikan, Evelina Busa, John C. Morris, Anders M. Dale, and Bruce Fischl. Thinning of the Cerebral Cortex in Aging. Cerebral Cortex, 14(7):721–730, 2004.

[124] 264–266. Smith G. E. 61(Pt 2). The principles of comparative localisation in the cerebralcortex based on cytoarchitectonics. J Anat., 61(Pt 2):264–266, 1927.

[125] Thompson PM Welcome SE Henkenius AL Toga AW.l Sowell ER, Peterson BS. Mapping cortical change across the human life span. Nat Neurosci., 6(3):309–15, 2003.

[126] Guido Gerig Alain Trouvé Nicholas Ayache Stanley Durrleman, Xavier Pennec. Spatiotemporalatlas estimation for developmental delay detection in longitudinal datasets. RR-6952, INRIA., 2009.

[127] Jean-Philippe Thirion. mage matching as a diffusion process: an analogy with maxwell's demons.medical image analysis,. Elsevier, 2(3):243–260., 1998.

[128] P. Thomas Fletcher. Geodesic regression and the theory of least squares on riemannian manifolds. International Journal of Computer Vision, 105(2):171–185, Nov 2013.

[129] Paul M. Thompson, Kiralee M. Hayashi, Elizabeth R. Sowell, Nitin Gogtay, Jay N. Giedd, Judith L. Rapoport, Greig I. de Zubicaray, Andrew L. Janke, Stephen E. Rose, James Semple, David M. Doddrell, Yalin Wang, Theo G.M. van Erp, Tyrone D. Cannon, and Arthur W. Toga. Mapping cortical change in alzheimer's disease, brain development, and schizophrenia. NeuroImage, 23:S2 – S18, 2004. Mathematics in Brain Imaging.

[130] Alain Trouve. Diffeomorphisms groups and pattern matching in image analysis. International Journal of Computer Vision, 28:213–221, 1998.

[131] Tom Vercauteren, Xavier Pennec, Aymeric Perchant, and Nicholas Ayache. Diffeomorphic demons: Efficient non-parametric image registration. NeuroImage, 45(1, Supplement 1):S61 – S72, 2009. Mathematics in Brain Imaging.

[132] Ziegler, G. Models of the aging brain structure and individual decline. Frontiers in Neuroinformatics, 2012.

[133] JC, M. et al. A probabilistic atlas and reference system for the human brain: International consortium for brain mapping (icbm). Philosophical transactions of the Royal Society of London. Series B, Biological sciences 356, 1293–322, 2001.

[134] Evans, A. C. et al. 3d statistical neuroanatomical models from 305 mri volumes. 1993 IEEE Conference Record Nuclear Science Symposium and Medical Imaging Conference 1813–1817 vol.3, (1993.

[135] Xing, W. et al. Probabilistic mri brain anatomical atlases based on 1,000 chinese subjects. PLOS ONE 8, 2013.

[136] Sivaswamy, J., Thottupattu, A. J., Mehta, R., Sheelakumari, R. & Kesavadas, C. Construction of indian human brain atlas. Neurol India 67, 229–34 ,2019.

[137] Miller, M. I. Computational anatomy: shape, growth, and atrophy comparison via diffeomorphisms. NeuroImage 23, S19 – S33,2004.

[138] Fletcher, T. Geodesic regression on riemannian manifolds. International Workshop on Mathematical Foundations of Computational Anatomy ,2011.

[139] Niethammer, M., Huang, Y. & Vialard, F.-X. Geodesic regression for image time-series. InFichtinger, G.,Martel, A. & Peters, T. (eds.) Medical Image Computing and Computer-Assisted Intervention – MICCAI 2011, 655–662 (Springer Berlin Heidelberg, Berlin, Heidelberg, 2011.

[140] Singh, N., Hinkle, J., Joshi, S. & Fletcher, P. T. A vector momenta formulation of diffeomorphisms for improved geodesic regression and atlas construction. 2013 IEEE 10th International Symposium on Biomedical Imaging 1219–1222 ,2013.

[141] Fishbaugh, J., Prastawa, M., Gerig, G. & Durrleman, S. Geodesic regression of image and shape data for improved modeling of 4d trajectories. In 2014 IEEE 11th International Symposium on Biomedical Imaging (ISBI), 385–388 ,2014.

[142] Fletcher, P. Geodesic regression and the theory of least squares on riemannian manifolds. International Journal of Computer Vision, 2013.

[143] Chevallier, J., Oudard, S. & Allassonnière, S. Learning spatiotemporal piecewise-geodesic trajectories from longitudinal manifold-valued data. Neural Information Processing Systems 2017 ,2017.

[144] Singh, N. & Niethammer, M. Splines for diffeomorphic image regression. InGolland, P.,Hata, N., Barillot, C.,Hornegger, J. & Howe, R. (eds.) Medical Image Computing and Computer-Assisted Intervention – MICCAI 2014, 121–129 (Springer International Publishing,Cham, 2014.

[145] Hinkle, J., Muralidharan, P., Fletcher, P. T. & Joshi, S. Polynomial regression on riemannian manifolds. InFitzgibbon, A.,Lazebnik, S., Perona, P.,Sato, Y. & Schmid, C. (eds.) Computer Vision – ECCV 2012, 1–14 (Springer Berlin Heidelberg,Berlin, Heidelberg, 2012.

[146] Banerjee, M. et al. A nonlinear regression technique for manifold valued data with applications to medical image analysis. In 2016 IEEE Conference on Computer Vision and Pattern Recognition (CVPR), 4424–4432 ,2016.

[147] Differentiating maturational and aging-related changes of the cerebral cortex by use of thickness and signal intensity. NeuroImage 52, 172–185, https://doi.org/10.1016/j.neuroimage.2010.03.056 ,2010.

[148] Hadj-Hamou, M., Lorenzi, M., Ayache, N. & Pennec, X. Longitudinal analysis of image time series with diffeomorphic deformations: A computational framework based on stationary velocity fields. Frontiers in Neuroscience 10, 236,2016.

[149] Fishbaugh, J., Durrleman, S. & Gerig, G. Estimation of smooth growth trajectories with controlled acceleration from time series shape data. InFichtinger, G.,Martel, A. & Peters, T. (eds.) Medical Image Computing and Computer-Assisted Intervention – MICCAI 2011, 401–408 (Springer Berlin Heidelberg, Berlin, Heidelberg, 2011.

[150] Fishbaugh, J. & Gerig, G. Acceleration controlled diffeomorphisms for nonparametric image regression. In 2019 IEEE 16th International Symposium on Biomedical Imaging (ISBI 2019), 1488–1491 ,2019.

[151] Bône, A., Colliot, O. & Durrleman, S. Learning the spatiotemporal variability in longitudinal shape data sets. International Journal of Computer Vision 128, 2020.

[152] Huizinga, W. et al. A spatio-temporal reference model of the aging brain. NeuroImage 169 ,2017.

[153] Fillmore, P. T., Phillips-Meek, M. & Richards, J. Age-specific mri brain and head templates for healthy adults from 20 through 89 years of age. Frontiers in Aging Neuroscience 7 ,2015.

[154] Liang, P. et al. Construction of brain atlases based on a multi-center mri dataset of 2020 chinese adults open. Scientific Reports 5, 18216,2015.

[155] Holla, B. et al. A series of five population-specific indian brain templates and atlases spanning ages 6–60 years. Human Brain Mapping 41, 2020.

[156] Dickie, D. A. et al. Brain imaging of normal subjects (brains) age-specific mri atlases from young adults to the very elderly. University of Edinburgh, Edinburgh Imaging, CCBS, BRAINSImagebank. v1, ,2016.

[157] Davis, B. C., Fletcher, P. T., Bullitt, E. & Joshi, S. Population shape regression from random design data. In 2007 IEEE 11th International Conference on Computer Vision, 1–7, 10.1109/ICCV.2007.4408977 ,2007.

[158] Zhang, Y. et al. Longitudinal atlas for normative human brain development and aging over the lifespan using quantitative susceptibility mapping. NeuroImage 171, 176 – 189, 2018.

[159] Avants, B. B. et al. The optimal template effect in hippocampus studies of diseased populations. Neuroimage 49, 2457–2466 ,2010.

[160] LeMay, M. Radiologic changes of the aging brain and skull. AJR. American journal of roentgenology 143,2, (383–389), (1984.

[161] Resnick, S., Pham, D., Kraut, M., Zonderman, A. & Davatzikos, C. Longitudinal magnetic resonance imaging studies of older adults: A shrinking brain. The Journal of Neuroscience 23, 3295 – 3301 ,2003.

[162] Hedman, A., Haren, N., Schnack, H., Kahn, R. & Pol, H. Human brain changes across the life span: A review of 56 longitudinal magnetic resonance imaging studies. Human brain mapping 33, 1987–2002 ,2012.

[163] Vercauteren, T., Pennec, X., Perchant, A. & Ayache, N. Symmetric log-domain diffeomorphic registration: A demons-based approach. InMetaxas, D.,Axel, L., Fichtinger, G. &Székely, G. (eds.) Medical Image Computing and Computer-Assisted Intervention – MICCAI 2008, 754–761 (Springer Berlin Heidelberg,Berlin, Heidelberg, 2008.

[164] Lorenzi, M. & Pennec, X. Efficient parallel transport of deformations in time series of images: From schilds to pole ladder. Journal of Mathematical Imaging and Vision 50, 5–17 ,2013.

[165] Nyberg, L., Lövdén, M., Riklund, K., Lindenberger, U. & Bäckman, L. Memory aging and brain maintenance. Trends in cognitive sciences 16, 292–305, ,2012.

[166] Fjell, A., Mcevoy, L., Holland, D., Dale, A. & Walhovd, K. What is normal in normal aging? effects of aging, amyloid and alzheimer's disease on the cerebral cortex and the hippocampus. Progress in Neurobiology 117, 2014.

[167] B. Landman, S. W. Miccai 2012 workshop on multi-atlas labeling, in: Miccai grand challenge and workshop on multi-atlas labeling, createspace independent publishing platform. CreateSpace Independent Publishing Platform ,2012.

[168] Ou, Y., Sotiras, A., Paragios, N. & Davatzikos, C. Dramms: Deformable registration via attribute matching and mutual-saliency weighting. Medical image analysis 15, 622–39,2011.

[169] Avants, B. et al. A reproducible evaluation of ants similarity metric performance in brain image registration. NeuroImage 54, 2033–2044 ,2011.

[170] Avants, B. et al. A reproducible evaluation of ants similarity metric performance in brain image registration. NeuroImage 54, 2033–2044 ,2011.

[171] Nichols, E. S., Wild, C. J., Owen, A. M., & Soddu, A. Cognition across the lifespan: Investigating age, sex, and other sociodemographic influences. Behavioral Sciences 11, 2021.

[172] Brayne, C. et al. Education, the brain and dementia: neuroprotection or compensation?: EClipSE Collaborative Members. Brain133, 2210–2216, 2010.

[173] Grant, A., Dennis, N. A., & Li, P. Cognitive control, cognitive reserve, and memory in the aging bilingual brain. Frontiers in Psychology 5, 2014.

[174] Wahl, D., Cavalier, A., & Larocca, T. Novel strategies for healthy brain aging. Exercise and Sport Sciences Reviews 49, 2021.

[175] Nijmeijer, S., van Tol, M.-J., Aleman, A., & Keijzer, M. Musical and Multilingual Experience Are Related to Healthy Aging: Better Some Than None But Even Better Together. The Journals of Gerontology: Series B ,78, 609–619, 2022

[176] Bethlehem, R. A. et al. Brain charts for the human lifespan. Nature,2021.

[177] Dickie, D. A. et al. Brain imaging of normal subjects (brains) age-specific MRI atlases from young adults to the very elderly. University of Edinburgh, Edinburgh Imaging, CCBS, BRAINSImagebank. v1, 2016.

[178] Fillmore, P. T., Phillips-Meek, M., & Richards, J. Age-specific MRI brain and head templates for healthy adults from 20 through 89 years of age. Frontiers in Aging Neuroscience, 7 (2015).

[179] Thottupattu, A. J., Sivaswamy, J., & Krishnan, V. P. A diffeomorphic aging model for adult human brain from cross-sectional data. Sci Rep 12, 12638, 2022.

[180] Thottupattu, Alphin J and Sivaswamy, Jayanthi A metric to compare the anatomy variation between image time series. arXiv 2023. `https://arxiv.org/abs/2302.11929`.

[181] Huizinga, W. et al. A spatio-temporal reference model of the aging brain. NeuroImage 169, 11–22, 2018.

[182] Johnson, Sara B. and Blum, Robert W. and Giedd, Jay N. Adolescent Maturity and the Brain: The Promise and Pitfalls of Neuroscience Research in Adolescent Health Policy. J Adolesc Health **45(3)**, 216-221 (2009).

[183] Zhang, Y. et al. Longitudinal atlas for normative human brain development and aging over the lifespan using quantitative susceptibility mapping. NeuroImage171, 176–189, 2018.

[184] Xie, W., Richards, J. E., Lei, D., Lee, K., & Gong, Q. Comparison of the brain development trajectory between Chinese and U.S. children and adolescents. Frontiers in Systems Neuroscience **8**, (2015).

[185] Resnick, Susan M. and Pham, Dzung L. and Kraut, Michael A. and Zonderman, Alan B. and Davatzikos, Christos Longitudinal magnetic resonance imaging studies of older adults: a shrinking brain. Journal of Neuroscience 23(8), 3295–3301, 2003.

[186] Shapiro, Robert and Galloway, Steven J. and Shapiro, Mitchell D. Minimal asymmetry of the brain: a normal variant. AJR. American journal of roentgenology ,147(4), 753–756, Oct 1986.

[187] Lewis, Mechelle M. and Smith, Andrea B. and Styner, Martin and Gu, Hongbin and Poole, Rae and Zhu, Hongtu and Li, Yimei and Barbero, Xavier and Gouttard, Sylvain and McKeown,

Martin J. and Mailman, Richard B. and Huang, Xu Asymmetrical lateral ventricular enlargement in Parkinson's disease. European Journal of Neurology ,16(4), 475–481, Apr 2009.

[188] Lou, Yixiao and Zhao, Liang and Yu, Songwei and Sun, Bin and Hou, Zhenming and Zhang, Zhiqiang and Tang, Yuchuan and Liu, Shuwei Brain asymmetry differences between Chinese and Caucasian populations: a surface-based morphometric comparison study. Brain Imaging and Behavior,14(6), 2323–2332, 2020.

[189] Yang, X. and others Diffeomorphic Metric Landmark Mapping Using Stationary Velocity Field Parameterization. Int J Comput Vis 115, 69–86, 2015.

[190] Kang, K. and Wang, S.M. and Na, H.R. and Park, S.Y. and Kim, N.Y. and Lee, C.U. and Kim, D.-H. and Son, S.J. and Lim, H.K. Differences in cortical structure between cognitively normal East Asian and Caucasian older adults: a surface-based morphometry study. Scientific Reports **10(1)**, 20905, 2020. https://doi.org/10.1038/s41598-020-77848-8.

[191] Tang, Y. and Zhao, L. and Lou, Y. and Shi, Y. and Fang, R. and Lin, X. and Liu, S. and Toga, A. Brain structure differences between Chinese and Caucasian cohorts: A comprehensive morphometry study. Human Brain Mapping **39(5)**, 2147–2155, 2018. https://doi.org/10.1002/hbm.23994.

[192] Huang, C.-M. and Doole, R. and Wu, C.W. and Huang, H.-W. and Chao, Y.-P. Culture-Related and Individual Differences in Regional Brain Volumes: A Cross-Cultural Voxel-Based Morphometry Study. Frontiers in Human Neuroscience **13**, 2019. https://doi.org/10.3389/fnhum.2019.00313.

[193] Bethlehem, Richard A. I. and Seidlitz, Jakob and White, Simon R. and others Brain charts for the human lifespan. Nature **604**, 525–533, 2022. https://doi.org/10.1038/s41586-022-04554-y.

[194] Brown, T. Individual differences in human brain development. Wiley Interdisciplinary Reviews: Cognitive Science **8**, (2016).

[195] Kijonka, M. et al. Whole brain and cranial size adjustments in volumetric brain analyses of sex- and age-related trends. (2020).

[196] Kang, D. H., Joung, W., Kim, S., Lee, J., & Kim, C. H. Brain entropy can be affected by modulations of complexity in human brain: resting state fMRI study. PLoS ONE **8**, (2013).

[197] Cheng, X., Li, Y., Duan, H., Wang, Y., & Mei, L. Reconstructing the complete cranial neural crest developmental program in vivo. Developmental Biology **397**, 99–106, (2015).

[198] Zhang, Y., Ding, W., Ding, Y., & Shi, S. Aging brain estimation via Gaussian process regression. International Conference on Medical Image Computing and Computer-Assisted Intervention, 353–361, 2019.

[199] Mehta, Raghav Population Specific Template Construction and Brain Structure Segmentation Using Deep Learning Methods. Thesis, International Institute of Information Technology, Hyderabad (2017).

[200] Gerig, Guido and Fishbaugh, James and Sadeghi, Nasim Longitudinal modeling of appearance and shape and its potential for clinical use. Medical Image Analysis, 33:114-121 (2016). doi: 10.1016/j.media.2016.06.014. PMID: 27344938; PMCID: PMC5381523.